

AD-A276 689

2



PL-TR-93-2005

ANALYSIS OF REGIONAL DISTANCE BODY WAVES FOR SEISMIC DISCRIMINATION

Terry C. Wallace
Guangwei Fan
Liping Gao

University of Arizona
Department of Geosciences
Tucson, AZ 85721

DTIC
SELECTE
FEB 25 1994
S B D

23 December 1992

Final Report
Period covered: August 1990—July 1992

11027
94-06128

Approved for public release; distribution unlimited

DTIC



PHILLIPS LABORATORY
Directorate of Geophysics
AIR FORCE MATERIEL COMMAND
HANSCOM AIR FORCE BASE, MA 01731-3010

94 2 24 090

The views and conclusions contained in this document are those of the authors and should not be interpreted as representing the official policies, either express or implied, of the Air Force or the U.S. Government.

This technical report has been reviewed and is approved for publication.


JAMES F. LEWKOWICZ
Contract Manager
Solid Earth Geophysics Branch
Earth Sciences Division


JAMES F. LEWKOWICZ
Branch Chief
Solid Earth Geophysics Branch
Earth Sciences Division


DONALD H. ECKHARDT, Director
Earth Sciences Division

This report has been reviewed by the ESD Public Affairs Office (PA) and is releasable to the National Technical Information Service (NTIS).

Qualified requestors may obtain additional copies from the Defense Technical Information Center. All others should apply to the National Technical Information Service.

If your address has changed, or if you wish to be removed from the mailing list, or if the addressee is no longer employed by your organization, please notify PL/IMA, 29 Randolph Road, Hanscom AFB, MA 01731-3010. This will assist us in maintaining a current mailing list.

Do not return copies of this report unless contractual obligations or notices on a specific document requires that it be returned.

TABLE OF CONTENTS

1.	Introduction	1
2.	Determination of source parameters for small earthquakes from a single station	3
3.	Regional distance recordings of large mining explosions: Distance-dependent discrimination	41
4.	Preliminary analysis of the crustal structure in Iran, Iraq, and Pakistan	53
5.	The seismotectonics of the Lop Nor, Xinjiang Province, People's Republic of China	64

Accession For	
NTIS GRA&I	<input checked="" type="checkbox"/>
DTIC TAB	<input type="checkbox"/>
Unannounced	<input type="checkbox"/>
Justification	
By	
Distribution/	
Availability Codes	
Dist	Avail and/or Special
A-1	

CHAPTER 1

REPORT INTRODUCTION

The role of seismology in monitoring nonproliferation is one of detection and discrimination of low-yield devices detonated in uncalibrated environments. The backbone of monitoring effort will be at regional distances, so it is essential to develop a detailed understanding of short-period, regional distance seismic phases from nuclear explosions, chemical explosions, and earthquakes. Most discrimination schemes are based on the excitation of various phases. Unfortunately, these regional distance phases are a complex combination of both propagation and source effects, and any algorithm for automated discrimination will require both empirical and analytical development. Here we report on our research efforts to study different types of seismic events at regional distances.

In Chapter 2 we discuss recovering the source parameters of small *earthquakes* recorded on a very sparse, very broadband network. We have chosen to work on earthquakes at this developmental stage because of the much larger data base available. We have developed a *single station moment tensor* algorithm (SSMT), which appears to work very well. This algorithm is very similar to the $M_L:M_0$ discriminant reported by Woods et al. (1992).

In Chapter 3 we discuss an empirical data base for large chemical explosions. This is of particular concern to global proliferation monitoring since there are many thousands of industrial explosions per year with magnitudes of the order of $m_b = 2.5$. This is the generally accepted magnitude which would correspond to a fully decoupled 1-kt nuclear explosion. Although there is considerable debate on whether 1 kt is an appropriate yield to expect in a nonproliferation environment, it is the size required to develop "boosted weapons." The spectral-temporal

characteristics of regional seismograms can be used to discriminate between different types of seismic sources. Most large mining explosions have a unique signature in the frequency domain due to the "ripple-fire" detonation explosions separated by small distances and times. We have attempted to better quantify the signature of ripple-fire explosions as a function of travel path, propagation distance, and shot configuration by studying chemical explosions in several environments.

Regional distance seismograms are often difficult to deterministically model. The characters of the phases Pg and Lg show a very strong dependence on travel path. Although scattering is apparently very important in controlling these phases, the gross features of the crustal waveguide, such as crustal thickness, Pn velocity, and the "continuity" of the waveguide, have a strong signature on the efficiency of Pg and Lg propagation. In Chapter 4 we have regionalized the crustal structure in the area around the western Himalayan syntaxis (Iran, Afghanistan, Pakistan, and northwestern India) and regions of concern for nonproliferation monitoring.

The Lop Nor underground nuclear test site is located in the northeastern corner of the Tarim Basin, Xinjiang Province, China. On 21 May 1992 the largest underground explosion since 1976 took place here ($m_b = 6.6$). This explosion, as with most detonated at Lop Nor, had a significant component of nonisotropic seismic radiation. The SH and Love wave energy appears to be consistent with a double-couple source. To better understand the tectonic release, we have begun to study the seismotectonics of the region.

CHAPTER 2

THE DETERMINATION OF SOURCE PARAMETERS FOR SMALL EARTHQUAKES FROM A SINGLE SEISMIC STATION

Introduction

Determination of the source parameters of shallow, moderate-sized earthquakes ($M_L < 5.5$) is an important seismological problem for several reasons. Earthquakes of this type have widespread geographic occurrence, and in some cases, these earthquakes provide the only clue to the active tectonics of a region. A considerable amount of effort has been expended to determine the source parameters of this size earthquake, although such determinations are beset with difficulties. Most of these events are too small to be well recorded teleseismically, so regional waveforms must be used to determine the source parameters. *Wallace and Helmberger* (1982) and *Patton* (1988) have developed inversion procedures for regional body and surface waves respectively. These methodologies allow the routine determination of source parameters for events as small as magnitude 5 when recorded by 3 or more stations. The installation of high quality, very broadband seismic stations suggests that these methods may lower the magnitude threshold to less than 4.5.

Unfortunately, as the magnitude of events is reduced the number of recording stations is correspondingly reduced. Several authors have suggested that fairly complete source information can be extracted from a single seismic station given certain conditions. *Langston* (1979; 1982) used P and SH waveforms to discriminate between fault types.

Ekstrom et al. (1986) applied the centroid moment tensor (CMT) method to retrieve focal mechanisms of large events, and *Jimenez et al.* (1989) developed a technique utilizing regional distance surface waves. Since new techniques of locating earthquake epicenters have been developed, it is possible to determine the epicentral parameters of an earthquake by using seismic data recorded from a single, three-component station (*Ruud et al.*, 1988). In this paper we present a simple linear moment tensor inversion procedure to retrieve the seismic source parameters at a single station which is situated at local to regional distances from a hypocenter. In this distance range the structure of the crust has a strong effect on body waves and therefore there are trade-offs between modeling assumptions and source parameters. Fortunately, the effect of the source orientation on the waveforms is fairly decoupled from the effects of the structural details, and essential information, such as the type of faulting, can be retrieved with very simple assumptions about the crustal model.

The inversion procedure is tested on two small earthquakes which were recorded on an IRIS/USGS GSN station located 65 km from the epicenter. The events were also well recorded on a local short-period network, which provides a basis for comparison of the fault plane parameters. The ability to recover accurate source parameters from a single station will be proved useful on at least two counts: (1) it will lower the magnitude threshold for which accurate source parameters can be determined from sparse broad band networks, and (2) it will greatly improve the information that can be recovered from portable instrumentation, such as a PASSCAL field recorder (with broad band sensors) which might be used for monitoring aftershocks or low level seismicity.

The Inversion Procedure

Linear moment tensor inversion techniques using body wave synthetic seismograms have been developed by numerous investigators (*Stump and Johnson, 1977; Langston, 1981; Wallace et al., 1981; Wallace and Helmberger, 1982*). Here we minimize the difference between observed and predicted ground displacements in three-components. Observed seismograms are windowed from the onset of P (or S) to arrivals of multiply reflected S (or surface wave). The synthetics are calculated using generalized ray theory. Following *Langston (1981)* the cylindrical displacements from a purely deviatoric point source in a layered stack can be represented as

$$\begin{aligned}
 v(t,r,z) &= s(t) * \sum_{i=1}^3 H_{vi}(t,r,z) A_i' \\
 q(t,r,z) &= s(t) * \sum_{i=1}^3 H_{qi}(t,r,z) A_i' \\
 w(t,r,z) &= s(t) * \sum_{i=1}^2 H_{wi}(t,r,z) A_{i+3}'
 \end{aligned} \tag{1}$$

where v , q , and w represent the displacements for vertical, radial and tangential components respectively, $s(t)$ is the normalized far-field source time function and $*$ represents convolution. The H_{di} terms (where $d=v, q, \text{ or } w$) represent the Green's functions for the three fundamental faults: vertical strike-slip, vertical dip-slip, and 45° dip-slip (*Langston and Helmberger, 1975*). The coefficients of the horizontal radiation pattern A_i' can be written as

$$A_1 = 0.5(M_{yy} - M_{xx})\cos(2AZ) - M_{xy}\sin(2AZ)$$

$$A_2 = M_{xz}\cos(AZ) + M_{yz}\sin(AZ)$$

$$A_3 = 0.5(M_{xx} + M_{yy})$$

$$A_4 = 0.5(M_{xx} - M_{yy})\sin(2AZ) - M_{xy}\cos(2AZ)$$

$$A_5 = M_{yz}\cos(AZ) - M_{xz}\sin(AZ)$$

where AZ is the azimuth between the source and receiver measured in a clockwise manner.

Most small events have simple time functions, which can be treated as "known" in equation (1). The other terms in (1) can be rearranged so that the moment tensor elements are factored; we can rewrite the displacements in terms of a linear combination of the moment tensor elements:

$$\begin{aligned} d_v = & 0.5 \cdot [GV45D - GVST \cdot \cos(2AZ)] \cdot M_{xx} \\ & + 0.5 \cdot [GV45D + GVST \cdot \cos(2AZ)] \cdot M_{yy} \\ & - GVST \cdot \sin(2AZ) \cdot M_{xy} \\ & + GVDP \cdot \cos(AZ) \cdot M_{xz} \\ & + GVDP \cdot \sin(AZ) \cdot M_{yz} \end{aligned}$$

$$\begin{aligned} d_r = & 0.5 \cdot [GR45D - GRST \cdot \cos(2AZ)] \cdot M_{xx} \\ & + 0.5 \cdot [GR45D + GRST \cdot \cos(2AZ)] \cdot M_{yy} \\ & - GRST \cdot \sin(2AZ) \cdot M_{xy} \\ & + GRDP \cdot \cos(AZ) \cdot M_{xz} \\ & + GRDP \cdot \sin(AZ) \cdot M_{yz} \end{aligned} \tag{2}$$

$$\begin{aligned}
d_t &= 0.5 \cdot \text{GTST} \cdot \sin(2AZ) \cdot M_{xx} \\
&- 0.5 \cdot \text{GTST} \cdot \sin(2AZ) \cdot M_{yy} \\
&- \text{GTST} \cdot \cos(2AZ) \cdot M_{xy} \\
&- \text{GTDP} \cdot \sin(AZ) \cdot M_{xz} \\
&+ \text{GTDP} \cdot \cos(AZ) \cdot M_{yz}
\end{aligned}$$

where GV (ST, DP, 45D) are the vertical Green's functions for the three fundamental fault orientations. GR and GT are Green's functions for the radial and tangential displacements respectively. The character of the Green's functions is related to the crustal structure and the source configuration, therefore it changes with source depth. Assuming a multi-layered crustal structure with a source located in the first layer, the three fundamental Green's functions were generated at a range of focal depth for an epicentral distance of 60 km. Figure 1 a), b) and c) show the three fundamental Green's functions for the tangential, radial and vertical component, respectively.

Equation (2) can be written as a series of simple expressions:

$$d_k(\mathbf{x},t) = \{G_{ki,j} * s(t)\} M_{ij} \quad (3)$$

where $d_k(\mathbf{x},t)$ represents the displacement vector and M_{ij} is the seismic moment tensor. Equation (3) has been used extensively to model regional distance seismograms (*Helmberger and Engen, 1980; Wallace and Helmberger, 1982; Wallace, 1986; Holt and Wallace, 1987*).

The matrix form of equation (3) is

$$\mathbf{d} = \mathbf{Gm} \quad (4)$$

Tangential Component Green's Function

(Unit of Max. Amp. = $1.0E-4$ cm)

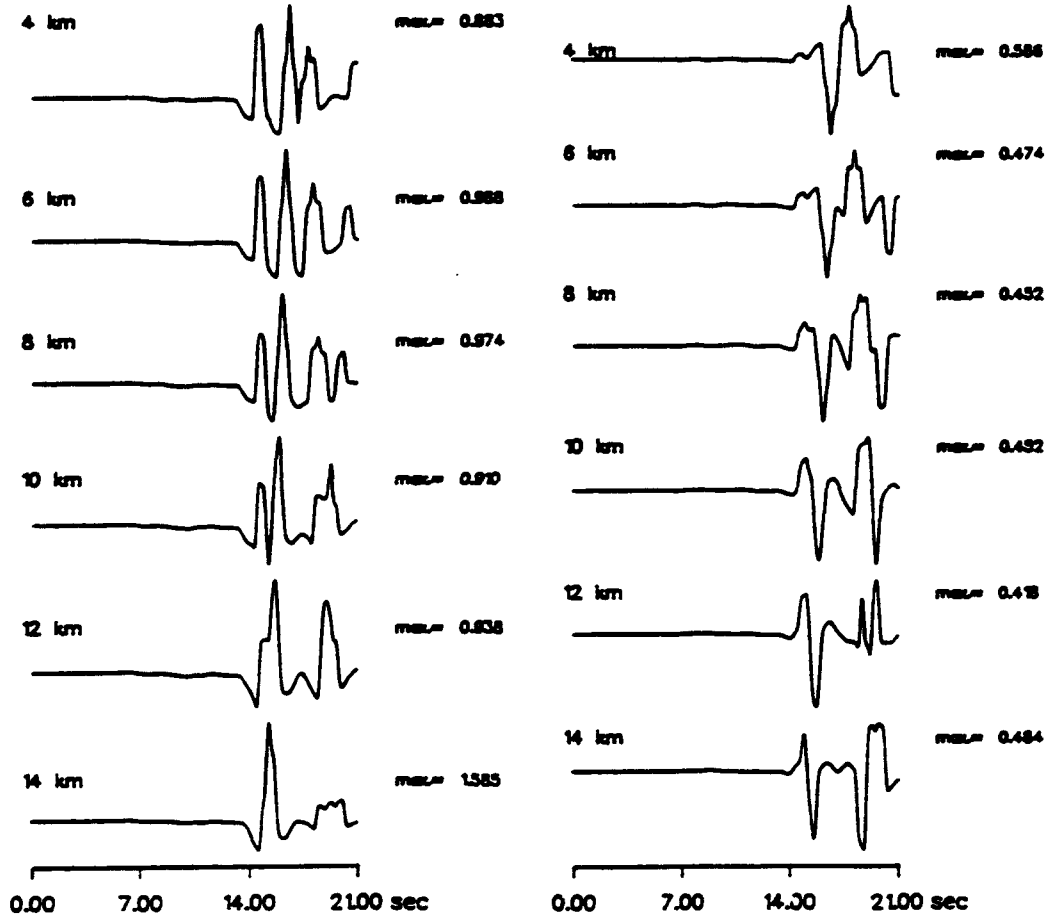


Figure 1a

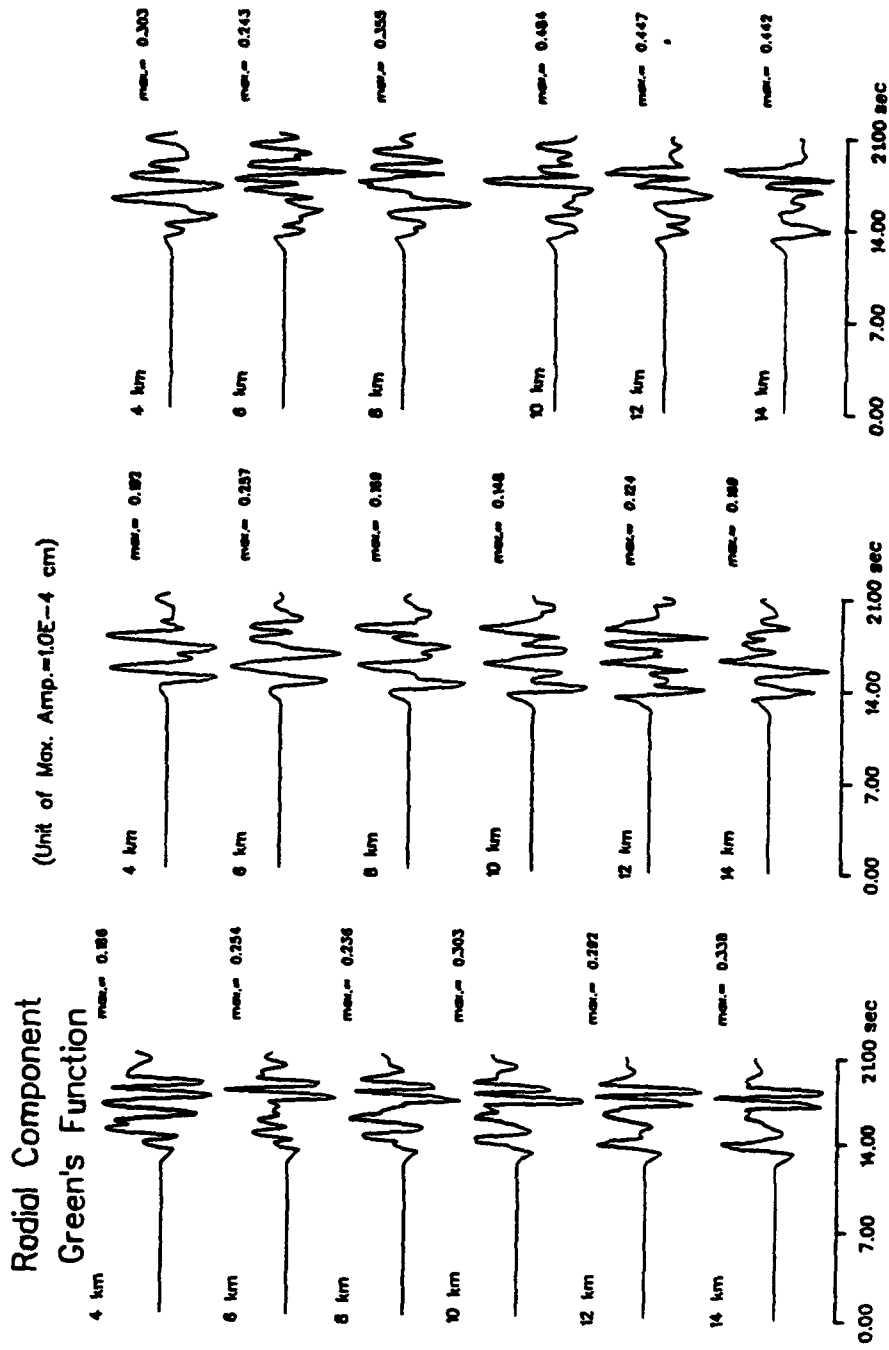


Figure 1b

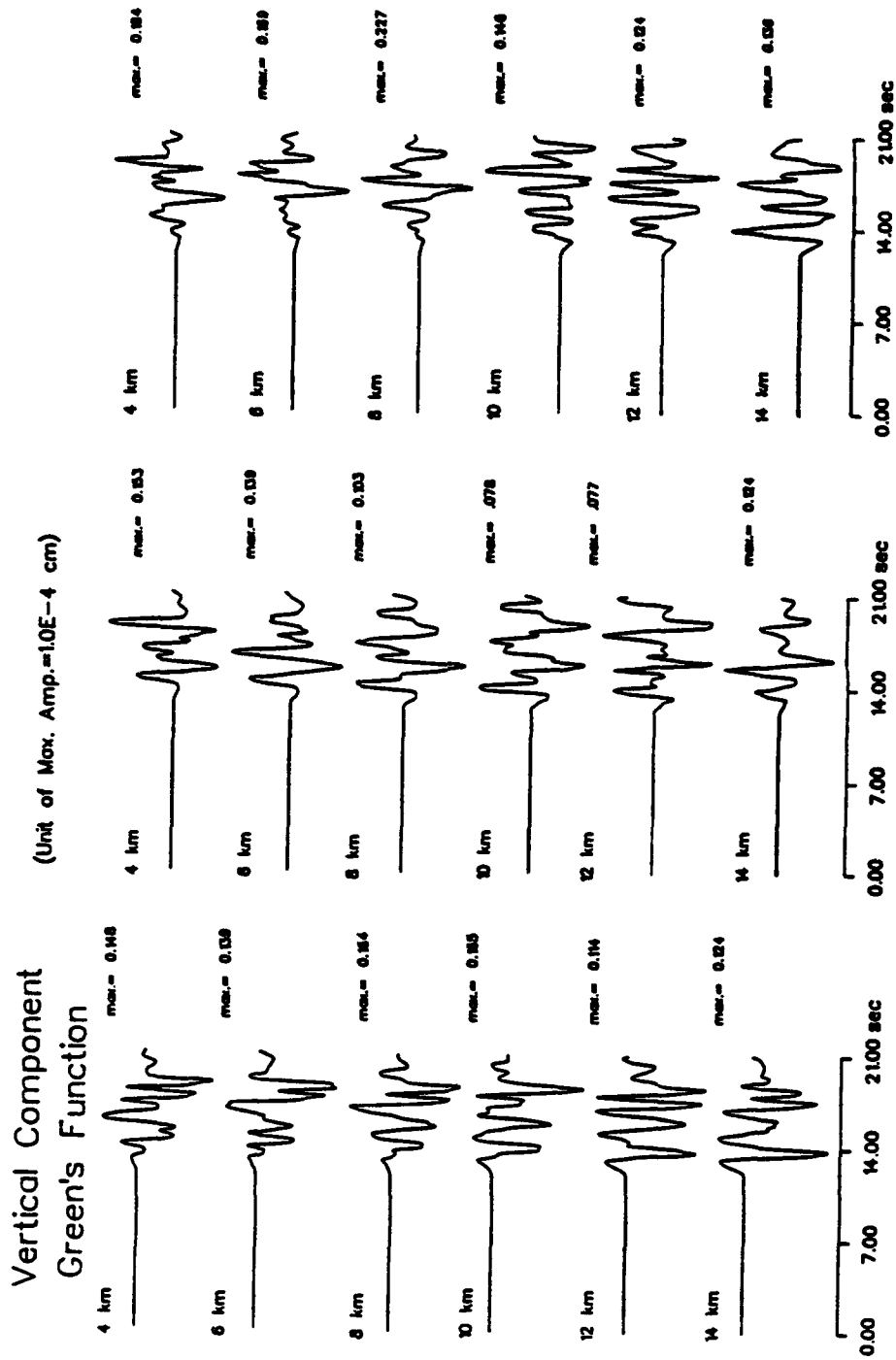


Figure 1c

where \mathbf{d} is a n -vector representing displacements sampled in the time domain; \mathbf{G} is a $n \times 5$ matrix and composed of the Green's functions, which are calculated from the generalized ray theory (although any technique is applicable) and convolved with the source time function and instrument response. Assuming a purely deviatoric moment tensor, \mathbf{m} is a vector containing five model parameters (the moment tensor elements: M_{xx} , M_{yy} , M_{xy} , M_{xz} , and M_{yz}). The moment vector \mathbf{m} can be determined by a generalized inverse method which minimizes the difference between the observed and synthetic waveforms. For uncorrelated data with a number of samples larger than 5, the system of equation (4) is overdetermined. This suggests that the moment tensor elements can be determined from a single, three-component seismic recording if the Green's functions are accurate enough.

The inversions are performed at a suite of focal depths, and the solutions obtained at various depths are objectively compared to constrain the "best" hypocentral depth. The inversion uses singular value decomposition (SVD), which allows us to evaluate the resolvability, stability and the trade-offs between moment tensor elements (*Menke, 1989*). Typically the largest non-zero singular values are less than 10, and the smallest are between 0.03 to 2. The condition number, λ , is the ratio of the largest to smallest non-zero singular value. We consider the inversion to be stable if λ is less than 100. However, it must be noted that smaller condition numbers do not necessarily mean a better fit between the synthetics and observed waveforms. Thus, we do not use the condition number λ for assessing the fits at various focal depths. The best fit focal depth and the fault plane solution are chosen in accordance with (1) the RMS error and (2) the moment variance.

The summed root-mean-squared (RMS) error measures the goodness of the fit, and can be written as:

$$E_{RMS} = [1/N \sum_{i=1}^N (O_i - C_i)^2]^{1/2} \quad (5)$$

and the summed squared misfit (SSM) obtained in the inversion can be represented in a similar way as

$$E_{SSM} = \sum_{i=1}^N (O_i - C_i)^2 \quad (6)$$

where O_i and C_i are observed and predicted ground displacements, respectively; and N is the total number of samples within the inversion window for each component. Figure 2 is a map of the RMS error versus depth obtained in our numerical experiments, which used synthetic seismograms as "observed" data and moment tensor inversion method to resolve typical sources of strike-slip, normal and reverse fault. It shows that the RMS error changes with depth and the minimum of the RMS error corresponds to the assumed "best" source depth of 10 km, thus providing a means for determining the focal depth and source parameters if three components were equally weighted. The SSM curve is similar to the RMS error curve, as expected (see Figure 3).

The moment variance measures the match in the amplitude and polarity between observed data and synthetics assuming that the seismic moment inferred from each component is constant. The moment variance is defined by

$$\sigma^2 \geq \sum_i (M_i - M_0)^2 \quad (7)$$

where σ^2 is the summed specified error, M_i is the ratio of the maximum amplitudes between the observed data and the synthetics, and M_0 is the predicted scalar seismic moment, determined by the average ratio of the maximum amplitudes between the

RMS ERROR CURVES

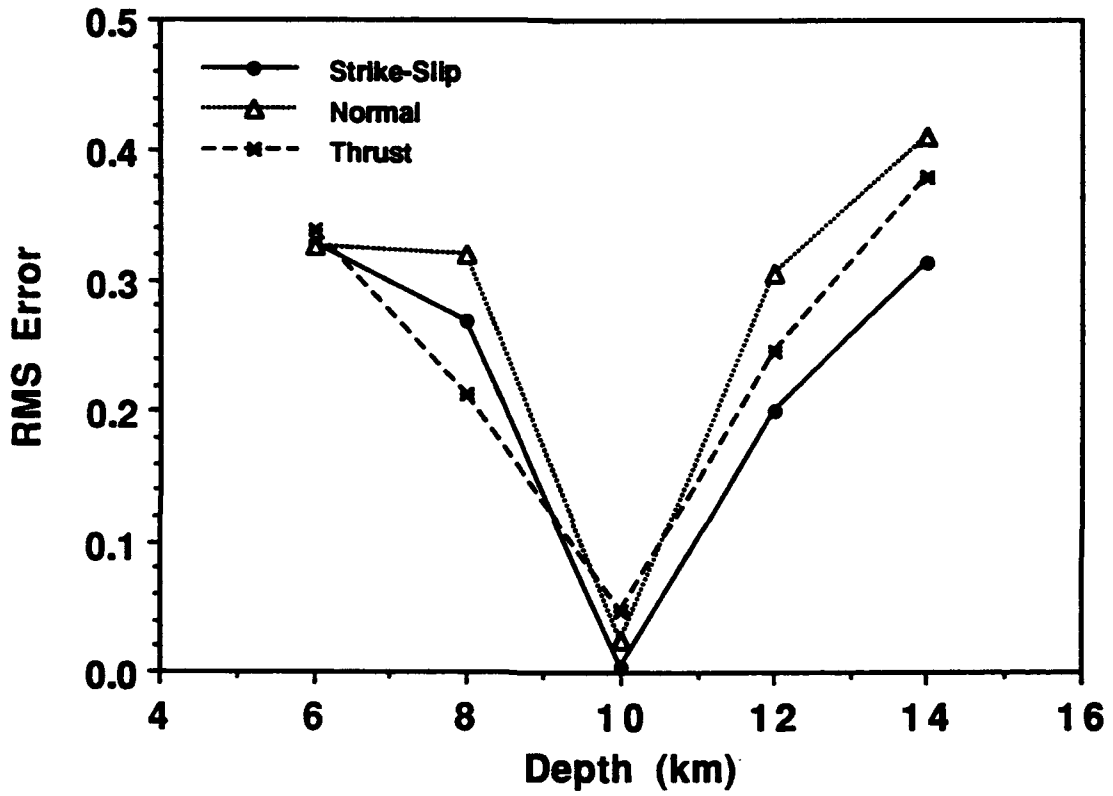


Figure 2

SSM ERROR CURVES

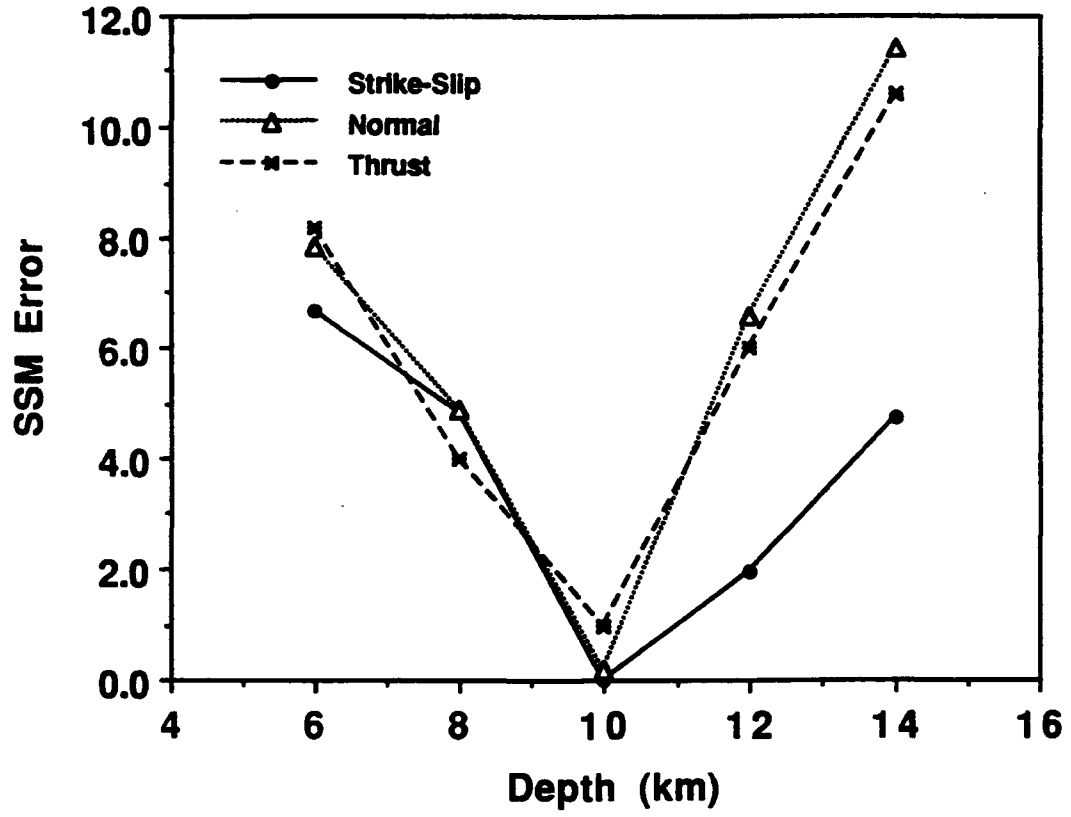


Figure 3

observed data to the synthetics for each component. The first motion polarity matches between the observed seismograms and the synthetics are also used to satisfy this criterion. The moment variance is similar to the objective function adopted by *Langston* (1981). Table 1 shows that the moment variance and the objective function both change with depth from numerical experiments for strike-slip, normal and reverse faults. Apparently, the minimum of the moment variance occurs at the assumed source depth, which then provides another means for determining the best-fit source parameters.

To test the inversion procedure we conducted several numerical experiments. In particular, we explored the trade-offs between inaccurate source models and source orientation, determined source depth using "best fit" criteria, and assessed the resolvability of various moment tensor elements. The "data" used in the experiments were synthetic seismograms computed for a range of 60 km; the source time function was a trapezoid (rise time, fault duration, and stopping time equal to 0.2, 0.4, 0.2 seconds, respectively) appropriate for small earthquakes. The crustal model used in the computation of the "data" has three crustal layers over a half-space mantle with a total crustal thickness of 32 km, which is illustrated by Figure 4a). For synthetics we used several models. In all models the density and P velocity increases with depth and usually range about 2600 - 2800 kg/m³ and 5.5 - 6.4 km/s, respectively, except for a model with a thin sedimentary layer. The mantle half-space has a density of 3300 kg/m³ and P velocity of 7.9 - 8.2 km/s. The seismic source resides within the upper crust and has a fixed depth of 10 km. Usually several hundreds rays were evaluated and summed, including the direct and reflected rays as well as converted phases. Since the seismic events are at local distances, the effects of attenuation are negligible, and no attenuation is used in our analysis.

Table 1 Moment Variance and Objective Function at
Different Focal Depths for Three Typical Faults

Depth (km)	Moment Variance			Objective Function		
	Strike-Slip	Normal	Thrust	Strike-Slip	Normal	Thrust
6	1.1400	0.3544	0.4936	20.3002	0.9810	0.7114
8	0.9208	0.1966	0.9073	9.9816	0.7945	1.2618
10	0.4698	0.0227	0.0242	3.8092	0.3285	0.2770
12	1.0647	0.7353	0.4630	7.6729	0.4739	0.9738
14	0.7333	0.5676	0.3979*	3.6079	1.0634	2.0110*

* indicates the reversed polarity for some of predicted synthetics.

MULTI-LAYERED CRUSTAL MODELS

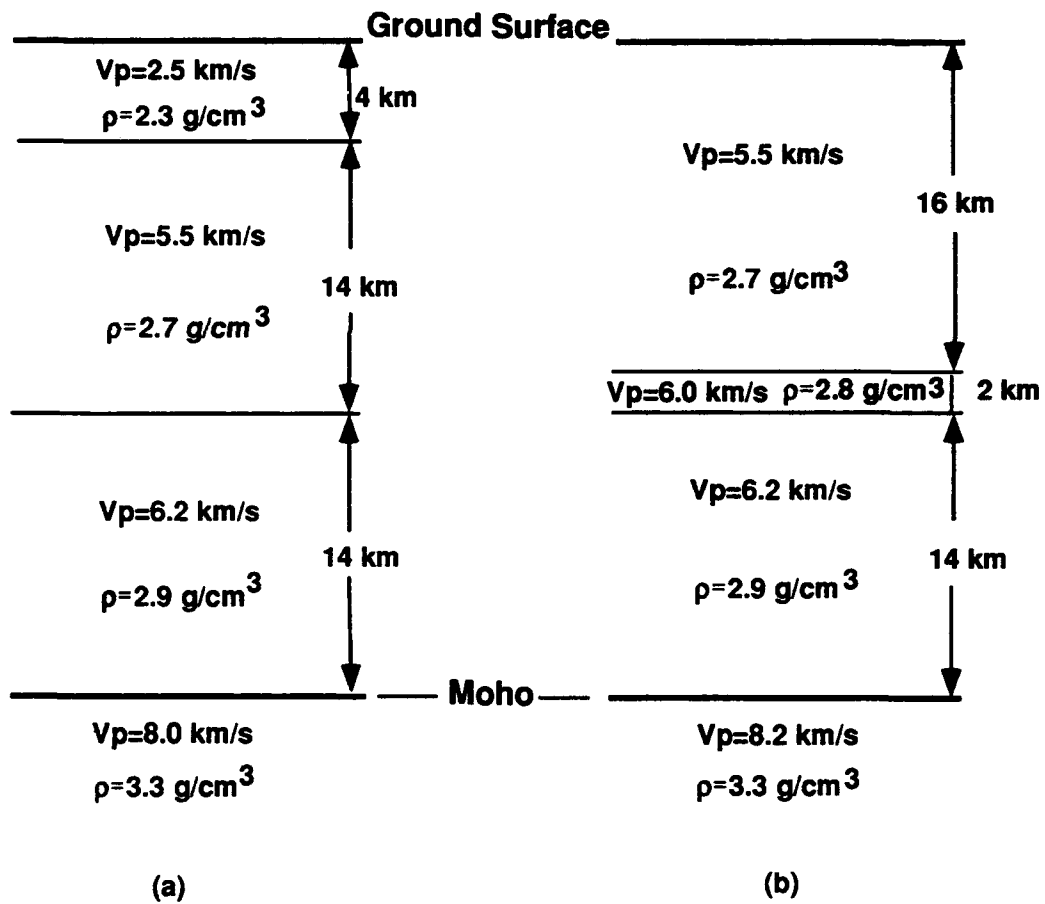


Figure 4

Generally speaking, this moment tensor inversion method is able to retrieve the focal depth and the source orientation of different kinds of model earthquakes. Table 2 a), b) and c) shows results from the moment tensor inversion for strike-slip and dip-slip (normal and thrust) faults, respectively. In all three cases, the focal mechanisms were well recovered around the best-fit depth with a small uncertainty. As the dip angle of a dip-slip fault changes, the best double couple solutions from the moment tensor inversion are also in good agreement with the original source orientations (see Table 3).

The most important rays in resolving the source orientation are direct rays and early arriving reflected rays and converted phases. The rays that arrive later provide less constraint on the source (*Wallace, 1986*). Since some converted phases and higher-order multiples have little effect on the shape of the waveforms in the inversion, they are less important in resolving the source mechanism. Generally speaking, upgoing waves are more important than downgoing waves.

It is instructive to test the model dependence of the method in its ability to recover the source. We conducted several experiments by varying the crustal models used in generating the Green's functions. Except for the one-layer crustal model, all multi-layered models have the same uppermost source layer, and we introduce small perturbations in crustal structure in the lower crust beneath the source (see Table 4). Both a dip-slip and a strike-slip source were tested. In nearly all cases the principal stress axes determined from the inversion are in good agreement with the starting source mechanism. At the local distance range (60 km) structural perturbations in the upper crust most strongly affect the source recovery; in contrast, the lower crustal structure has minor influence on the seismic source if the source resides in the upper crust. Better knowledge of the upper crust (above the source, including the source layer) enhances the ability to retrieve the seismic source (*Helmberger and Johnson, 1977*) and the effects of the lower crust have little influence on

Table 2a). Results of Moment Tensor Inversion for
a Strike-Slip Fault at Different Focal Depths

Depth (km)		6	8	10	12	14	Model
M _{xx}		-0.1069	1.0000	0.7753	1.0000	0.8180	0.6403
M _{yy}		-0.5599	-0.0021	-0.8682	-0.4691	-0.2332	-0.6403
M _{xy}		0.1953	-0.5512	-0.5015	-0.4871	-0.4730	-0.7631
M _{xz}		0.1258	0.1330	0.1599	0.1319	0.1732	0.0819
M _{yz}		-0.4108	-0.0066	-0.0215	0.0476	0.4920	0.0298
STRIKE (°)		18.6	62.5	28.8	32.2	36.1	20.0
DIP (°)		61.7	42.0	81.7	64.5	57.9	85.0
SLIP (°)		-91.6	84.7	-6.7	21.6	40.1	0.0
P axis	AZ(°)	285	336	344	343	159	335
	PL(°)	73	3	11	4	1	4
T axis	AZ(°)	110	205	254	251	249	245
	PL(°)	17	85	1	32	50	4
SSM Error		6.689	4.806	7.30E-3	1.973	4.746	
RMS Error		0.3279	0.2688	0.0033	0.1998	0.3150	
CLVD(%)		4.484	21.516	6.493	53.209	2.801	
Condition Number		4.077	6.154	7.502	6.687	4.268	

Table 2b). Results of Moment Tensor Inversion for
a Normal Fault at Different Focal Depths

Depth (km)	6	8	10	12	14	Model	
M_{xx}	-1.0562	0.1862	0.1436	0.3554	-0.2597	0.0153	
M_{yy}	-0.8344	-0.3688	-0.5514	-0.4718	-0.3961	-0.3561	
M_{xy}	0.7038	-0.0697	-0.0880	-0.1063	-0.0003	0.0437	
M_{xz}	-0.1043	-0.0352	0.4216	-0.2410	0.2827	0.3344	
M_{yz}	-0.3315	-0.8834	-1.3149	-1.2257	-0.2960	-0.8745	
STRIKE (°)	41.0	358.2	16.6	347.9	29.0	20	
DIP (°)	47.8	81.3	81.4	83.3	63.7	80	
SLIP (°)	-101.3	-86.9	-79.6	-93.1	-81.4	-85	
P axis	AZ(°)	244	272	299	254	317	296
	PL(°)	81	54	52	52	70	55
T axis	AZ(°)	139	85	98	81	113	106
	PL(°)	2	36	36	38	18	35
SSM Error	7.870	4.865	0.185	6.577	11.40		
RMS Error	0.3255	0.3201	0.0253	0.3051	0.4107		
CLVD(%)	15.512	20.567	2.784	28.326	46.288		
Condition Number	4.478	9.973	7.163	8.006	3.996		

Table 2c). Results of Moment Tensor Inversion for
a Thrust Fault at Different Focal Depths

Depth (km)	6	8	10	12	14	Model	
M_{xx}	1.0003	-0.7742	0.2391	-0.8310	0.2736	0.0950	
M_{yy}	0.2315	-0.3301	0.2759	-0.0927	0.1757	0.2457	
M_{xy}	-1.1699	-0.0369	-0.4384	0.02841	-0.2233	-0.1753	
M_{xz}	-0.1491	-0.0296	-0.5541	0.0941	-0.4523	-0.3059	
M_{yz}	-0.2531	0.8932	1.2164	0.9519	0.1346	0.8848	
STRIKE (°)	74.5	139.3	25.6	120.6	66.6	20	
DIP (°)	48.5	61.6	78.6	57.9	68.5	80	
SLIP (°)	119.7	-65.3	79.8	-53.5	101.5	85	
P axis	AZ(°)	324	92	124	85	148	114
	PL(°)	1	64	33	59	23	35
T axis	AZ(°)	55	212	283	186	356	284
	PL(°)	68	13	55	6	65	55
SSM Error	8.177	3.978	0.970	5.981	10.59		
RMS Error	0.3383	0.2128	0.0481	0.2462	0.3806		
CLVD(%)	31.216	64.127	6.809	56.510	4.648		
Condition Number	6.241	7.132	4.576	5.920	3.877		

Table 3 Inversion Results For a Dip-Slip Fault
with Different Dip Angles

Trial #	Starting Model			Double Couple			CLVD (%)	SSM Error	RMS Error
	ST	Dip	Rake	ST	Dip	Rake			
1	20	90	-85	205	84	75	3.758	0.843	0.040
2	20	80	-85	17	81	-80	2.784	0.185	0.025
3	20	70	-85	7	68	-89	9.464	0.043	0.107
4	20	60	-85	11	57	-93	26.43	2.7E-6	0.5E-4
5	20	50	-85	13	49	-89	24.36	0.129	0.006
6	20	40	-85	15	41	-87	14.70	0.347	0.014
7	20	30	-85	14	32	-92	2.678	0.663	0.027
8	20	20	-85	7	23	-110	4.322	1.427	0.088
9	20	10	-85	28	14	-92	1.895	1.568	0.046

Table 4

Different Crustal Models Used in Numerical Experiments

Model	# of Layer	V _p (km/s)	V _s (km/s)	ρ (kg/m ³)	Th (km)
Original	1	5.8	3.35	2600	16
3-layer	2	6.0	3.5	2700	02
Crustal	3	6.2	3.6	2800	14
Model	4	8.0	4.6	3300	01
1-layer	1	6.0	3.5	2700	32
Model	2	8.0	4.6	3300	01
2-layer	1	5.8	3.35	2600	16
Crustal	2	6.2	3.6	2800	16
Model	3	8.0	4.6	3300	01
3-layer	1	5.8	3.35	2600	16
Crustal	2	6.2	3.6	2800	02
Model	3	6.4	3.7	2900	14
(A)	4	8.0	4.6	3300	01
3-layer	1	5.6	3.2	2500	16
Crustal	2	6.2 (6.0)	3.6 (3.5)	2800 (2700)	02
Model	3	6.4	3.7	2900	14
(B)	4	8.0	4.6	3300	01
	1	5.8	3.35	2600	16
4-layer	2	6.0	3.5	2700	02
Crustal	3	6.2	3.6	2800	08
Model	4	6.4	3.7	2900	06
	5	8.0	4.6	3300	01

our ability to resolve the source. This is because the relative timing of various arrivals are more sensitive to the velocity perturbation in the upper layer than that in the lower layer. Stretched or squeezed waveforms have to be compensated in some way to reduce the phase shift. Fortunately, the consequences of a "wrong" crustal model are usually compensated by changing focal depth if the velocity perturbation is small. Thus the assumption of one layer over a half space works surprisingly well if the layer velocity is equal to the average crustal velocity. As a result of this, there is a trade-off between structure and focal depth and a reasonably recovered source might be accompanied by a "wrong" source depth. Figure 5 a) and b) show the "true" sources of dip-slip and strike-slip faulting compared to fault plane solutions found in inversion by using various "wrong" crustal models. In general the source orientation can be well recovered.

Another limitation to the inversion is the level of the random noise. The fault plane parameters are unreliable if the signal-to-noise ratio is too small, especially if the character of the first pulses in vertical and radial components is lost. Even though the model parameters were still well resolved mathematically, fault plane parameters converted from the moment tensor elements showed a large departure from the actual source parameters and indicated that recovery of the source failed. A comparison between the observed and synthetic waveforms also showed a relatively large RMS error and some inconsistencies between the waveforms. In general, the moment tensor elements, as well as the fault plane parameters could be recovered from the inversion if the noise level is equal to or less than 10% of the maximum amplitude within the inversion windows and there are distinct first motions. Numerical experiments show that the fault plane parameters were not as good as those obtained with the noise-free data, but they were fairly consistent with the starting model. Obviously, the less the noise in the data, the better the recovery of the source. The early part of record, especially the first motion, plays a very important role in

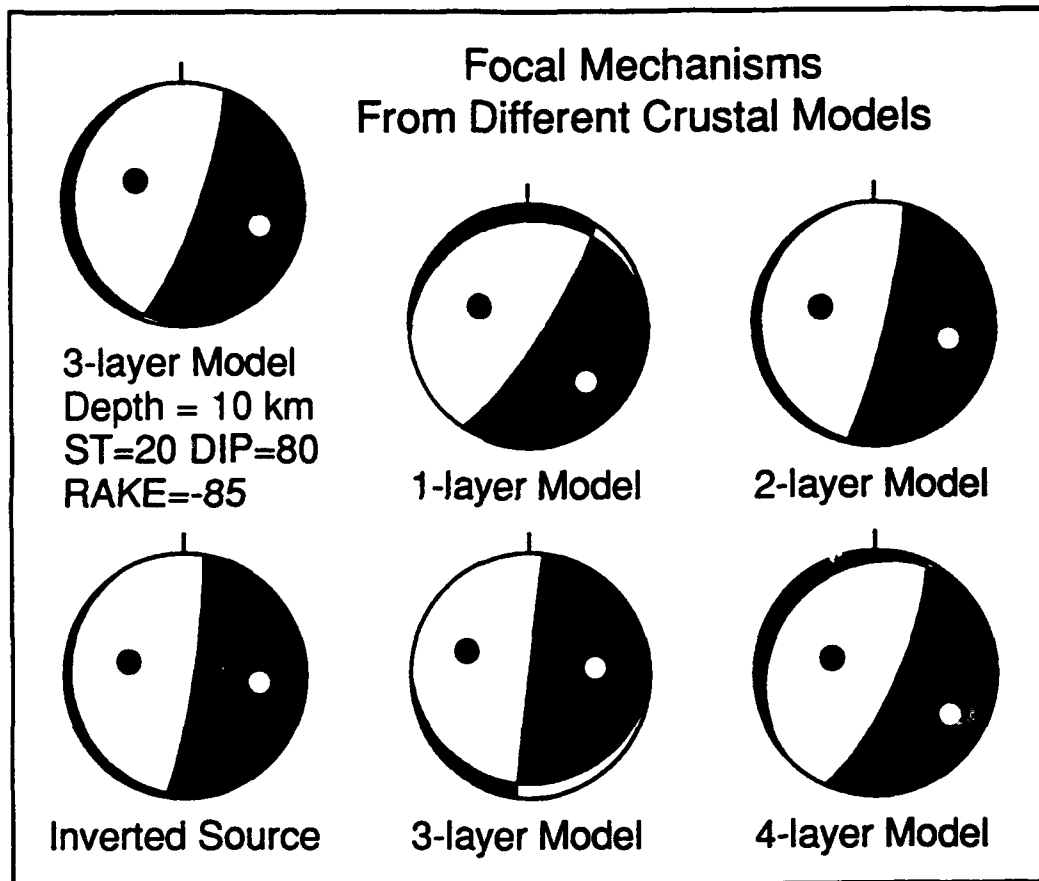


Figure 5a

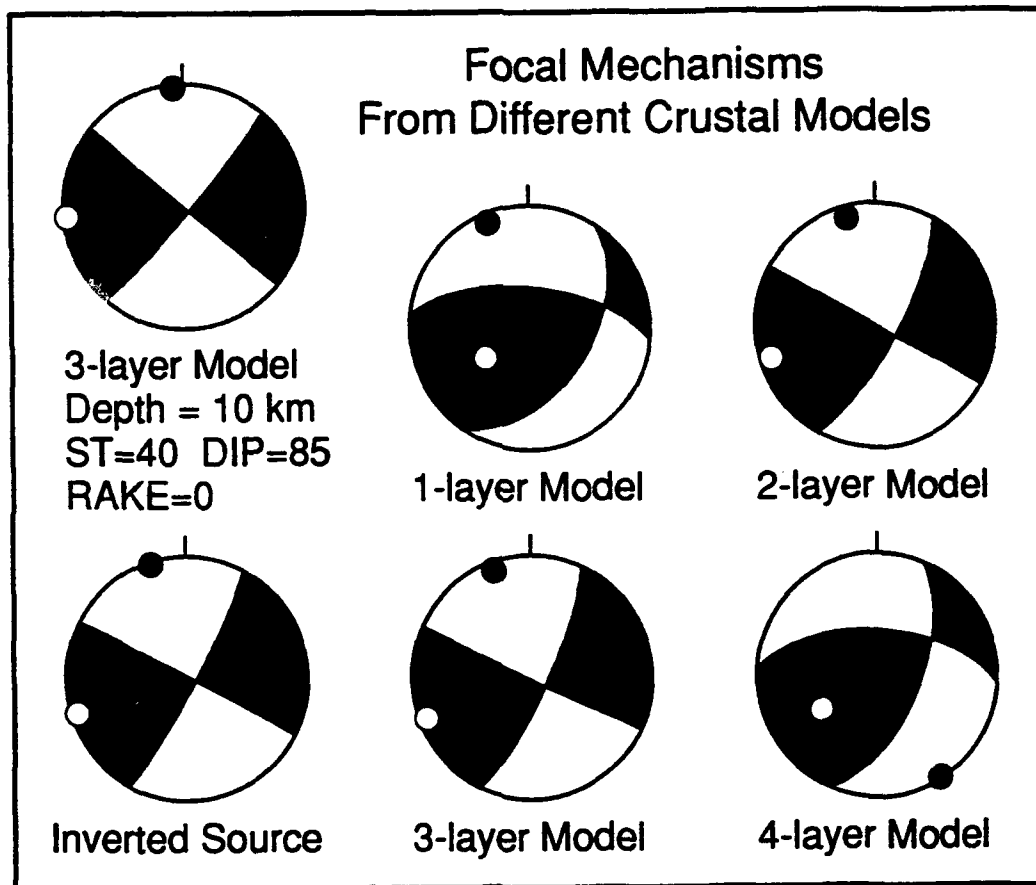


Figure 5b

this process. On the basis of practical experience (discussed below), it should be possible to recover the source parameters of events as small as magnitude 2.5 at 60 km if recording conditions are favorable.

Earthquake Analysis

The moment tensor inversion procedure outlined in the preceding section was applied to two small earthquakes which occurred near Bernardo, New Mexico on 29 November 1989 (event #1) and 29 January 1990 (event #2). The earthquakes are part of a strong earthquake swarm which began with the November event and has continued through at least January 1991. There were 15 events with $M_L > 2.5$ and hundreds of smaller events in the swarm. The epicenters for the events are in the Rio Grande Rift; they are the largest earthquakes in the Rift since 1906-1907 (*Sanford*, personal communication, 1990). Figure 6 is a simplified map showing the epicentral region and the focal mechanisms obtained in this study. The seismograms used in this analysis were recorded at ANMO (Albuquerque, New Mexico) approximately 65 km north of the epicenters. The epicentral parameters obtained from a local network are presented in Table 5 (*Sanford*, personal communication, 1990).

Several crustal structural models have been used in generating the Green's functions for the inversion. One of the crustal models used is shown in Figure 4b). We were most concerned with developing a procedure for the routine recovery of the source mechanism, rather than developing an ideal structural model. The "best" crustal model was a three-layer crustal model with a total thickness of 32 km which was only a rough approximation to the real structure. From geophysical studies, a magma body with a

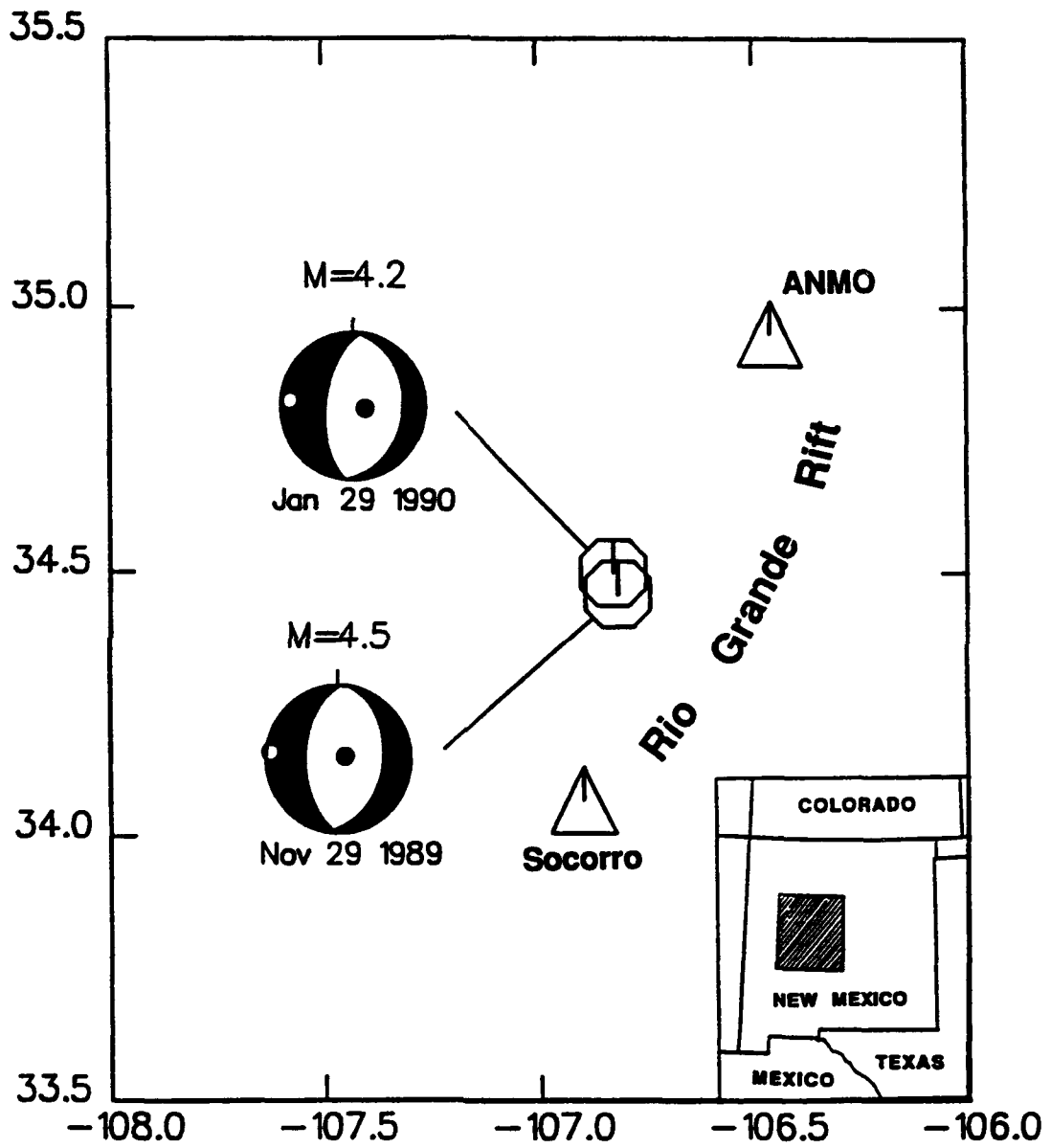


Figure 6

Table 5 The Epicentral Parameters for Two New Mexico
Events Derived From Local Network

Event	Date	Origin Time	Epicenter		Depth (km)	M_L	Δ at ANMO (km)
			Lat ($^{\circ}$)	Lon ($^{\circ}$)			
1	29 Nov.,1989	06 ^h 54 ^m 37.9 ^s	34.46	-106.82	9	4.5	63.5
2	29 Jan.,1990	13 ^h 16 ^m 09.6 ^s	34.50	-106.83	9	4.2	60.2

thickness of about 150 m is located at a depth of 19 km in the central Rio Grande Rift and extends over an area of at least 1700 km² near Socorro, New Mexico (*Brown et al.*, 1980; *Sanford et al.*, 1977). Seismic study from Rayleigh wave data also indicates the evidence for a magma-filled dike-like structure about 200 m thick and 28 km long in the middle of the Albuquerque-Belen basin of the Rio Grande rift (*Schlue et al.*, 1988). The three-layer crustal model was designed to model the upper crust of the area (neglecting details such as the magma bodies) and apparently crucial source information has been extracted.

Based on the assumed crustal model, a set of Green's functions were generated for different focal depths from 4 to 14 km and the generalized inversion was performed. The time function is a trapezoid ($\tau = 0.5\delta\tau_1 + \delta\tau_2 + 0.5\delta\tau_1$) (*Helmberger and Malone*, 1975) with a total source duration τ being determined from the corner frequency: $f_0 = 1/(\pi\tau)$. The total source duration was 0.5 - 0.7 seconds, which is consistent with the magnitude of the events. The smallest non-zero singular value in this case was order 1, and the estimated condition numbers λ were about 2.5 to 4.5 which imply stable solutions were obtained. The moment tensors corresponding to different focal depths were compared. Based on the two post-inversion criteria (the RMS error and the moment variance), the best fit fault plane solution could be chosen from a set of diverse double couple parameters. Table 6 shows the RMS error, the moment variance and the objective function obtained from our moment tensor inversion at different depth for two New Mexico small earthquakes.

For event #1 both the RMS error and moment variance were minimized at a depth of 8 km. Since the transmission paths for P and SH waves are nominally the same, the amplitudes depend only on the source orientation and seismic moment; and are independent of details of the source rupture. *Slunga* (1981) has shown that at a distance of less than 100 km the earthquake source can be determined based on only observation of the polarities

**Table 6 RMS Error, Moment Variance and Objective Function
at Different Focal Depths for Two New Mexico Events**

Depth (km)	RMS Error		Moment Variance		Objective Function	
	#1	#2	#1	#2	#1	#2
4	0.431	0.355	0.017*	0.028*	1.115*	2.938*
6	0.479	0.382	0.138	0.009	3.554	1.215
8	0.431	0.394	0.005	0.002	0.559	0.545
10	0.474	0.449	0.021	0.510	3.258	6.711
12	0.487	0.411	0.065	0.011	7.840	0.841
14	0.448	0.418	0.113	0.007	24.319	0.710

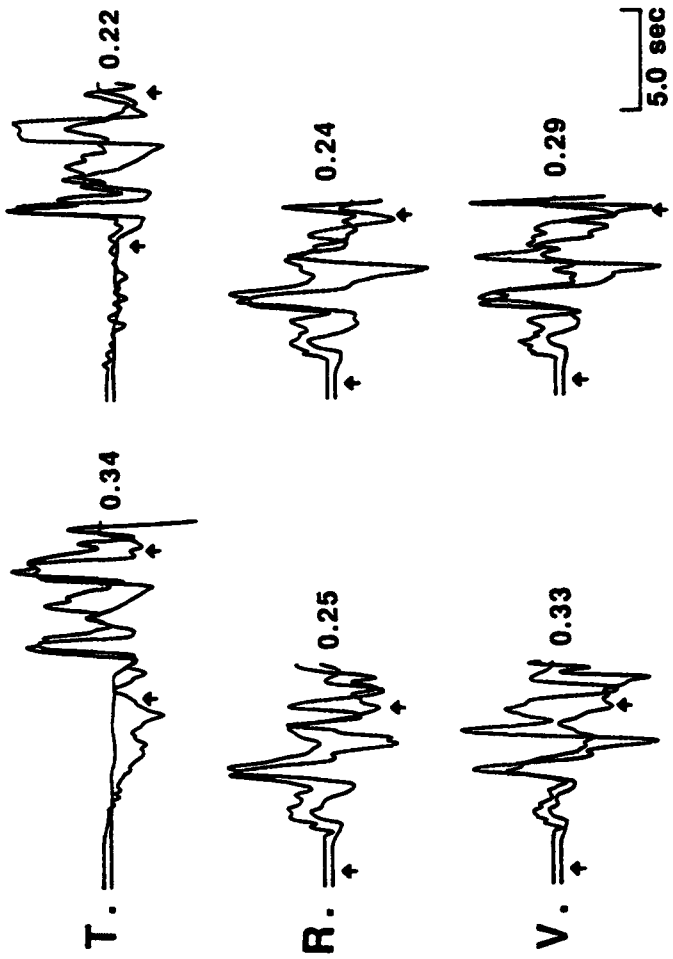
* indicates the reversed polarity for some of predicted synthetics.

and amplitudes. Therefore, the solutions at depths of 4 or 14 km were rejected because of the large moment variance or opposite polarities of the predicted first motions against the observed seismograms for the radial and vertical components.

The waveforms for the 29 January, 1990 event are similar to the first event. The first motion polarities in vertical and radial components were the same, but their amplitudes were smaller by a factor of 10. The same procedure was applied to the second event, and a similar conclusion is obtained based on the analysis of RMS errors and the moment variance. The moment variance reached a minimum at 8 km, although the depth was not well resolved. We prefer to choose a best fit solution at a depth of 8 km, because of its consistency with the fault plane solution of the first event.

Using the moment tensor solutions obtained in the inversion, a comparison between the synthetics and the observed waveforms for the two events is shown in Figure 7. The RMS errors are of 0.43 and 0.39 for the first and the second event, respectively. The match was good considering the simplified crustal model. Table 7 and Table 8 show the moment tensor elements, the corresponding major double couple parameters, the percentage CLVD (Compensated Linear Vector Dipole) of the moment tensor, and the condition number of the inversion for the two events, respectively.

Figure 8 summarizes the fault plane solutions obtained for various crustal models. Note the orientation of the principal stress axes (and type of faulting) is fairly consistent for all models. The solutions are similar to the P-wave first motion solution (*Sanford*, personal communication, 1990). All the moment tensor results require a normal faulting focal mechanism with two north-south striking nodal planes. The depth determined is strongly model dependent. The preferred depth ranges from 8 to 12 km comparable with the results obtained by *Sanford* (personal communication, 1990). It is clear that a multi-layered crust gives the best results and a detailed crustal structure is



NOV. 29, 1989 **JAN. 29, 1990**
Depth = 8 km **Depth = 8 km**
RMS ERROR = 0.41 **RMS ERROR = 0.39**

Figure 7

Table 7
 Estimates of Moment Tensor Elements and Double-Couple
 Fault Parameters for the 29 November, 1989 Event

DEPTH (km)	4	6	8	10	12	14
M_{xx}	0.4682	0.0899	-0.2919	0.2874	0.5833	0.3345
M_{yy}	0.9029	0.2351	-0.4833	0.1773	0.1531	-0.4801
M_{xy}	-0.6996	-0.2884	0.0296	-0.4897	-0.1614	-0.2167
M_{xz}	0.0716	0.0398	0.0489	0.3516	-0.1246	-0.3747
M_{yz}	0.0700	0.1989	0.1680	0.2843	0.4692	-0.1483
STRIKE ($^{\circ}$)	32	14	10	17	33	305
DIP ($^{\circ}$)	45	60	38	53	61	79
SLIP ($^{\circ}$)	84	59	-84	39	63	-138
CLVD (%)	2.8	12.5	44.7	11.8	14.1	2.3
Condition Number	4.38	4.27	4.08	3.29	3.37	4.38

Figure 8

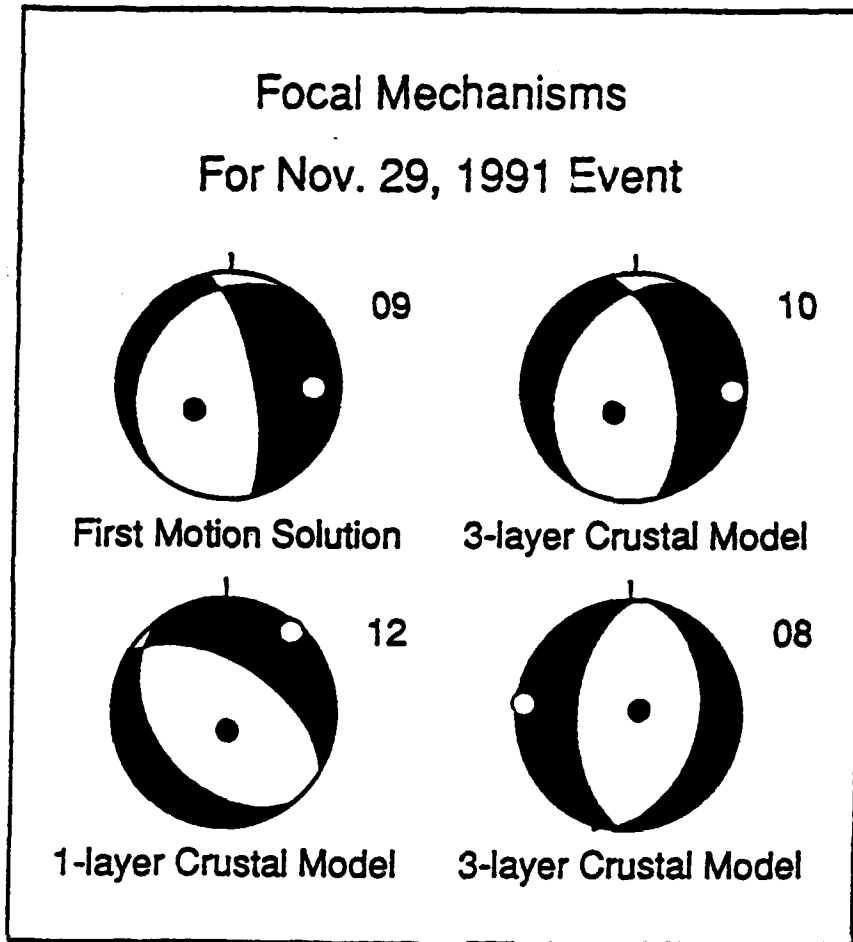


Table 8

Estimates of Moment Tensor Elements and Double Couple
Fault Parameters for the 29 January, 1990 Event

DEPTH (km)	4	6	8	10	12	14
M_{xx}	0.6951	0.1383	-0.0621	0.1253	0.2726	-0.1503
M_{yy}	0.6078	-0.1079	-0.6532	-0.1709	0.2467	-0.3360
M_{xy}	-0.7282	-0.3435	0.0526	-0.1362	-0.1999	0.1910
M_{xz}	0.1254	0.1862	-0.0492	-0.2333	-0.4261	-0.1941
M_{yz}	-0.0786	0.2160	0.3722	0.2712	0.1219	-0.3891
STRIKE (°)	45	15	4	304	64	1
DIP (°)	42	65	31	30	66	65
SLIP (°)	88	19	-92	-174	102	-114
CLVD (%)	5.7	29.7	7.4	23.9	15.0	30.5
Condition Number	4.08	3.10	4.10	2.64	3.02	3.54

COMPOSITION of EIGENVECTORS in Vp SPACE

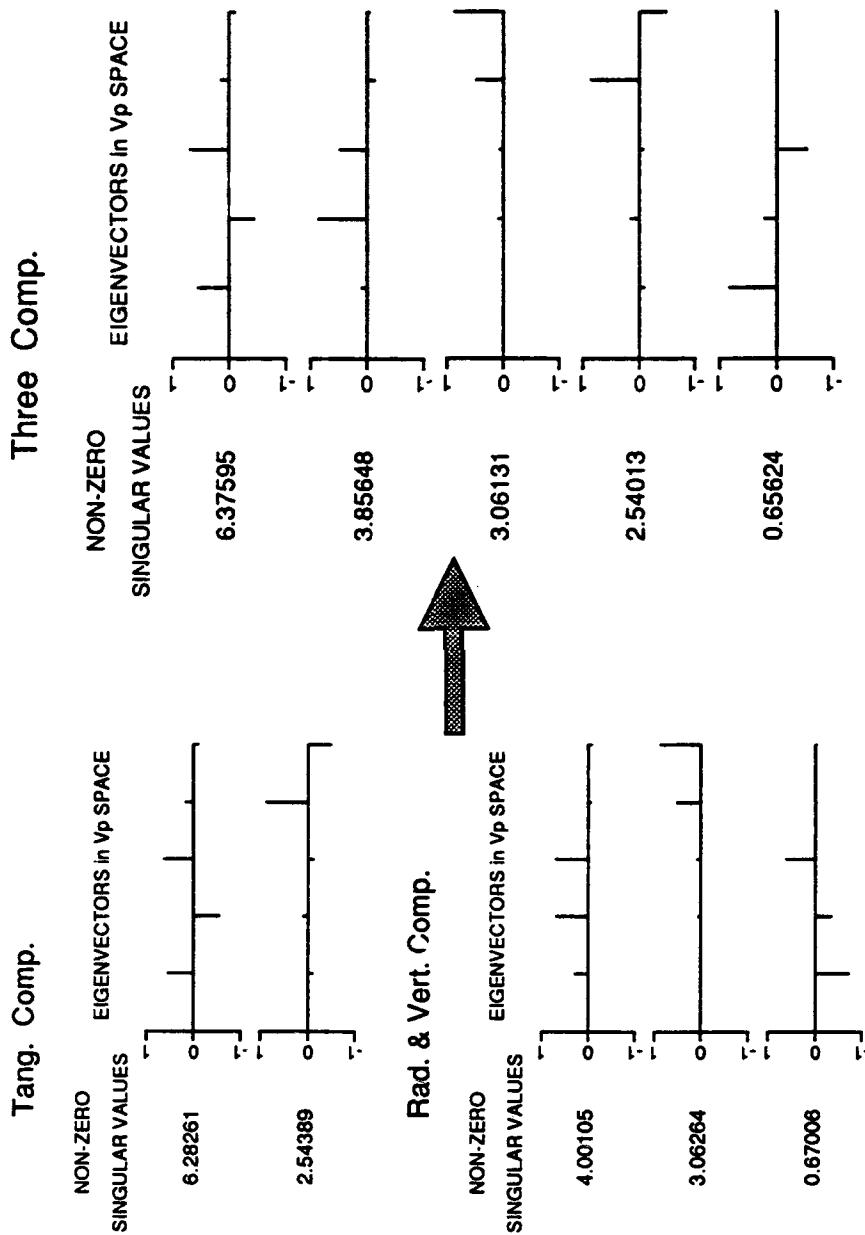


Figure 9

superior for generating the Green's functions, but surprisingly, even a single-layered crust can provide valuable source information. This is extremely important if this inversion process is to be automated.

After a best fit moment tensor mechanism was selected, the scalar seismic moment of the earthquake could be determined based on the ratio of the maximum amplitudes between the observed waveforms to the synthetic seismograms within the time window used in the inversion. We found that the scalar seismic moment M_0 for the first event was about 2.0×10^{15} N-m, and for the second event about 1.7×10^{15} N-m. The CLVD calculated ranges from 2-45 % for the 29 November, 1989 event, and from 5-30 % for the 29 January, 1990 event. However, it was impossible to attach any importance to the size of the CLVD since the CLVD size was very strongly dependent on the different crustal structural models used in inversion.

Discussion

To determine the moment tensor from a single seismic station is possible as long as more than one component of motion is used and sufficient number of data points are used. *Stump and Johnson* (1977) showed this for body wave data; others have shown it for various types of teleseismic data: normal mode data (*Gilbert and Dziewonski*, 1975), and surface wave data (*Kanamori et al.*, 1981). Which components of the moment tensor are best resolved depends on the type of seismic data used in the inversion and the distance range concerned. It is clear that if only one component of displacement is used in the inversion only 2 or 3 model parameters are resolvable; neglecting the tangential component

COMPOSITION of EIGENVECTORS in Vp SPACE

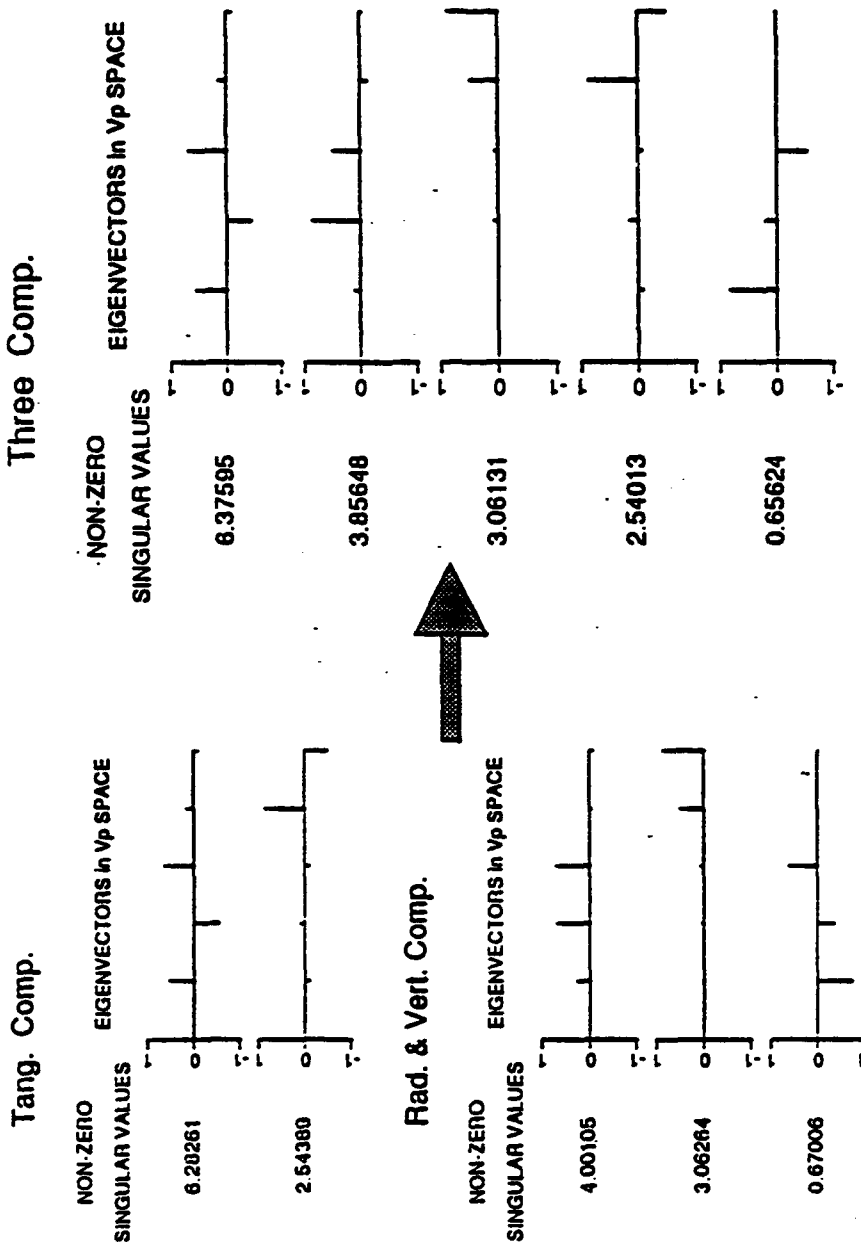


Figure 9

always results in less than 5 non-zero singular values. Figure 9 shows the eigenvectors in model space, V_p from three components, which can be decomposed into two parts from the tangential component and vertical plus radial component. Two components of motion, one being the tangential, the other being the radial or vertical, will provide 5 non-zero singular values, although the results are not as good as those obtained when all three components of motion are used (see Table 9).

At a short distance range (about 60 km or more), interferences between various reflected phases made the shape of waveforms more complicated as the source depth changed. This could be seen clearly from the change in shape of the Green's functions. As a result of this the focal depth is model-dependent and only can be constrained within a certain range as we have discussed. Obviously, better knowledge about the crustal structure, especially upper crustal structure, will be helpful in determining an accurate focal depth.

Adding independent data from another seismic station will greatly improve the quality of the inversion. In an experiment using two independent seismic stations with epicentral distances of 60 and 90 km and azimuths of 60° and 150° , respectively, all model parameters were well resolved. Larger non-zero singular values resulted in a sharp decrease of the condition number λ compared with that in the case of a single seismic station. The diagonal terms of the posterior model covariance matrix are also reduced. In other words, a much better solution with better stability and smaller variance was achieved in our inversion by adding more stations.

Nevertheless, a single station can be used for the recovery of the seismic source parameters as long as it has high dynamic range and is very broadband. Since many earthquakes are only recorded on a limited number of seismic stations, or a single station, this inversion procedure can greatly extend the usefulness of such sparse recordings.

Table 9 Non-zero Singular Values and Corresponding Eigenvectors in Model Space V_p

Cases	Non-Zero Singular Values	Eigenvectors in V_p Space					Condition Number
Tang. Comp.	5.93406 2.32509	0.54669 -0.54669 0.63127 0.05308 -0.03064				-0.03357 0.03357 -0.03876 0.86440 -0.49906	
Vert. Comp.	2.52857 0.68190 0.26518		0.18887 0.59276 0.69956 -0.17576 -0.30443	0.12281 0.25152 0.22294 0.46689 0.80868		0.72158 0.39598 -0.56396 -0.03346 -0.05795	
Rad. Comp.	3.81329 2.74719 0.59127		0.35544 0.68664 0.57366 -0.13520 -0.23416	0.10980 0.19661 0.15037 0.48132 0.83367		-0.65806 -0.24759 0.71095 0.00729 0.01262	
Vert. + Rad. Comp.	4.54841 2.83597 0.79754		0.30458 0.65879 0.61352 -0.15557 -0.26946	0.13121 0.22937 0.17003 0.47467 0.82216		-0.67930 -0.29121 0.67218 0.02193 0.03798	
Vert. + Tang. Comp.	5.96603 2.45522 2.32292 0.68010 0.26067	-0.54915 0.51185 -0.65767 -0.04439 0.04401	-0.04823 -0.74525 -0.54355 0.29679 0.24240	0.08704 0.30497 0.18713 0.46518 0.80499	-0.26870 0.13357 0.03432 0.83210 -0.53653	0.82934 0.26790 -0.48562 -0.03400 -0.05863	22.887
Rad. + Tang. Comp.	6.00271 3.71009 2.74293 2.32482 0.57540	0.57277 -0.44706 0.68421 0.04111 -0.04726	0.19532 0.85287 0.38734 -0.16678 -0.23795	0.08335 0.24953 0.12280 0.46791 0.83472	-0.27354 0.05141 -0.02973 0.86688 -0.49420	0.79126 0.08858 -0.60486 -0.00791 -0.01207	10.432
Three Comp.	6.07857 4.36072 2.83029 2.32484 0.77815	0.57687 -0.35480 0.73130 0.01994 -0.07834	0.07578 0.87781 0.34274 -0.18830 -0.26603	0.09867 0.28639 0.13667 0.46117 0.82273	-0.02794 0.05016 -0.03026 0.86657 -0.49482	0.80682 0.13794 -0.57283 -0.02296 -0.03675	7.812

CHAPTER 3

REGIONAL DISTANCE RECORDINGS OF LARGE MINING EXPLOSIONS: DISTANCE DEPENDENT DISCRIMINATION

Introduction

Regional distance seismology will play an important role in monitoring a non-proliferation treaty or a restricted, low yield test agreement. The two technical facets of such monitoring are the discrimination between explosions and earthquakes, and discrimination between chemical and nuclear explosions. The focus of this research has been on the chemical/nuclear explosion identification. Most large mining explosions have a unique signature in the frequency domain due to the "ripple fire" detonation of explosions separated by small distances and times. Ripple fire produces a unique spectral signature which is strongly scalloped, and this signature can be used to discriminate between chemical and nuclear explosions (Smith, 1988; Baumgardt and Ziegler, 1988; Hedlin et al., 1988; Suteau-Henson and Bache, 1988). This nuclear/chemical explosion discriminant is best at very high frequencies (> 20 Hz), but many of the GSN and Soviet-IRIS stations are limited by a sampling rate of 20 sps. In order to investigate the robustness of a ripple fire discriminate we have constructed a data base of seismic waveforms from chemical explosions in New Mexico, Arizona, Utah, California, Missouri, and Germany recorded on broad band seismic systems. In all cases we have standardized the sampling rate to 20 sps. The data base now contains 712 recordings with travel paths ranging from 12 km to 1456 km. The travel paths represent many different geologic environments, many different blasting procedures and two orders of magnitude in explosion size.

Construction of the Data Bases

Much of the recent work in seismic yield determination and discrimination has emphasized the use of regional distance data. There are several advantages to using regional distance data. First, regional distance seismic stations can significantly reduce the detection threshold over that achieved by teleseismic monitoring. The Lg amplitude recorded at regional distances provides a very stable yield estimate. Finally, spectral discriminate based on the fact that earthquakes produce more high frequency seismic energy than explosions can be used with a high degree of confidence to small magnitudes ($m_b \sim 3.5$). Although much work remains to be done on quantifying the effects of travel path on discrimination and yield determination, the outstanding problem in regional distance verification is the identification and characterization of large chemical explosions. Is it possible to always discriminate between nuclear and chemical explosions? Is it feasible to develop an evasion scenario in which a nuclear explosion is fired in conjunction with a series of chemical explosions? The only way to answer these questions is to develop a data base of observations which can be analysed in terms of travel path, explosion configuration and recording instrumentation. We have begun to develop data base which now contains 712 recordings with travel paths ranging from 12 km to 1456 km. The travel paths represent many different geologic environments, many different blasting procedures and two orders of magnitude in explosion size.

Most chemical explosion discriminates have been investigated for very high frequencies (40 Hz) because the spectra stripping is most obvious when broad band width is used. Unfortunately, the high frequencies attenuate rapidly for many regions; the effectiveness of a scalloping discriminate is strongly dependent on travel path, which is probably a reflection of variation in attenuation. We have used a lower pass band (20 cps) to detail the effectiveness of various parameterization of spectra stripping as function of distance. We have developed a significance test for scalloping based on the strength of the

holes, and their periodicity. A spectra which has strongly developed, periodic scalloping will have a significance of 1; a non periodic scalloping will have a much lower significance. For the various regions studied we have developed relationships between significance versus distance.

The Southwestern U.S. Chemical Explosion: We used the recordings at two IRIS stations (ANMO and TUC) which are equipped with STS -1 seismometers to develop a catalogue of explosions. 16 mines or quarries produced a least one usable seismogram at ANMO, which resulted in 136 recordings. The size of the explosions ranges from 17,000 to 171,000 pounds. The travel paths cross several different geologic provinces (the Rio Grande Rift, the Colorado Plateau, the Datil Plains), and attenuation ($Q\beta$) probably varies by a factor of 3. The mines in northern New Mexico and Arizona are primarily coal; the mines in southern New Mexico and Arizona are open pit copper mines. In general, the coal mines have larger explosions but the signal amplitude corrected for distance is smaller than those explosions from copper mines. The frequency content is higher, suggesting that attenuation is not responsible for the reduction in amplitude, but rather, it is the result of the explosion medium.

Figure 10 shows 9 mines which produced recording at TUC. Table 10 gives the coordinates of the mines and the size of the largest explosion recorded from a given mine. Several of the mines have multiple explosions daily, and blasting practices varies considerably between mines. We have developed a catalogue of 393 explosions recorded at TUC. Figure 11 is a histogram of the explosion as a function of distance for recordings at ANMO and TUC. The bulk of the explosions are at distances of less than 600 km, although some clear recordings are seen all the way out to 1100 km. Figure 12 shows a comparison between the waveforms from an earthquake (July 28, 1992, $M_L = 2.8$) and copper mining explosion approximately the same distance from TUC. A causal inspection of the whole waveform spectra does not offer obvious discrimination between the

Explosion Sources in the Southwestern U.S.

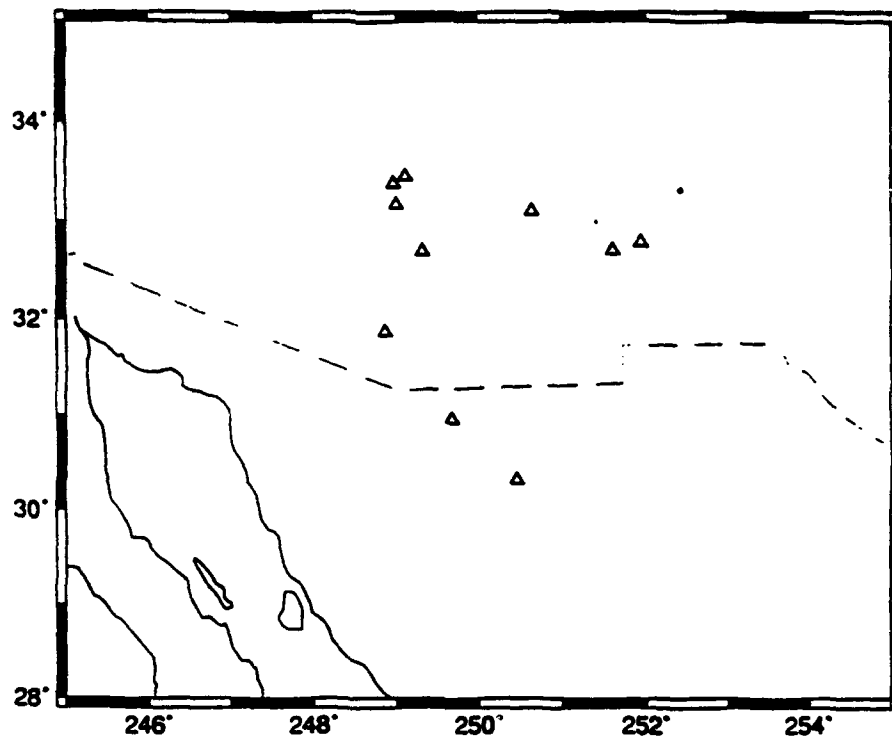


Figure 10

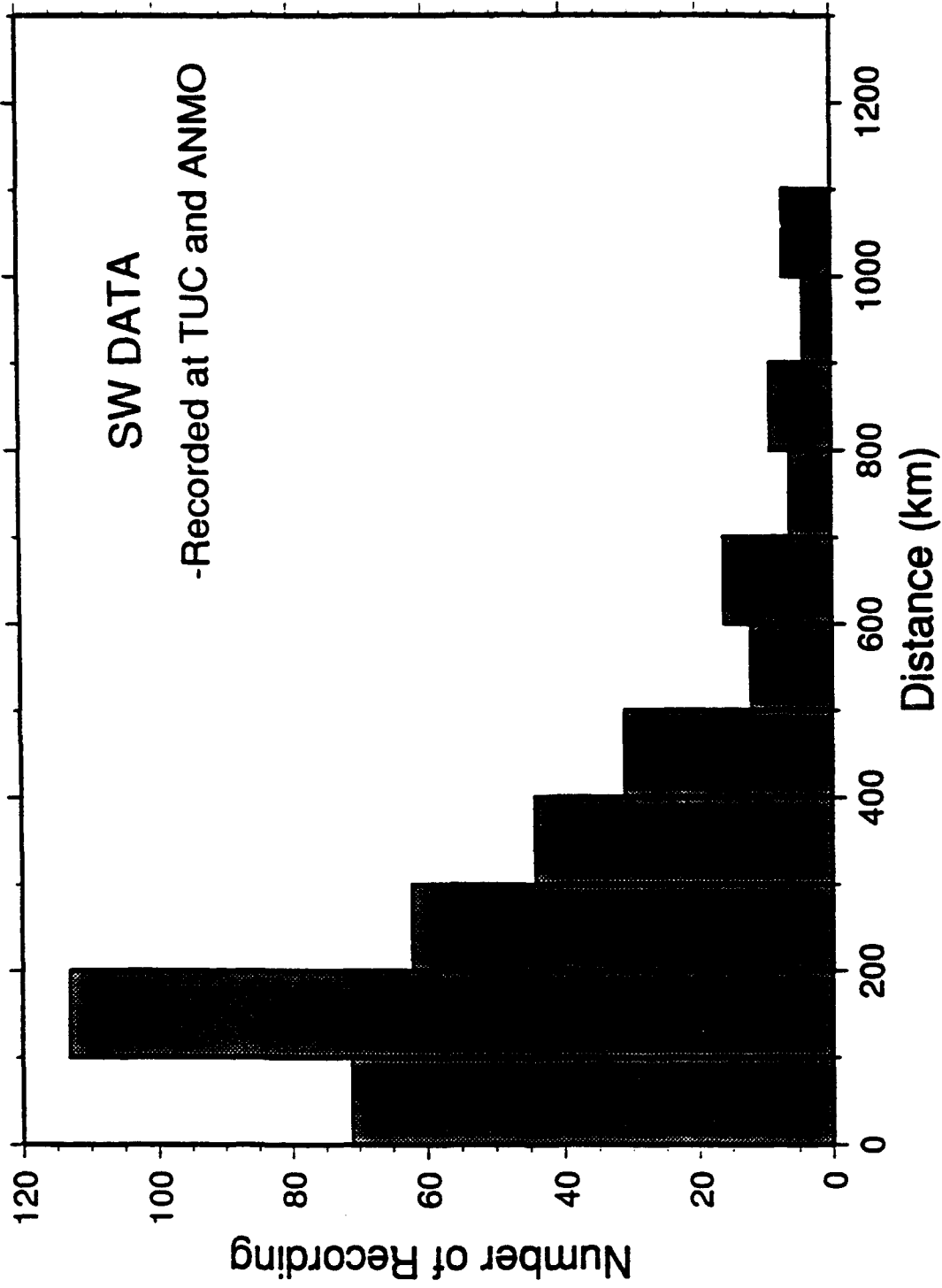


Figure 11

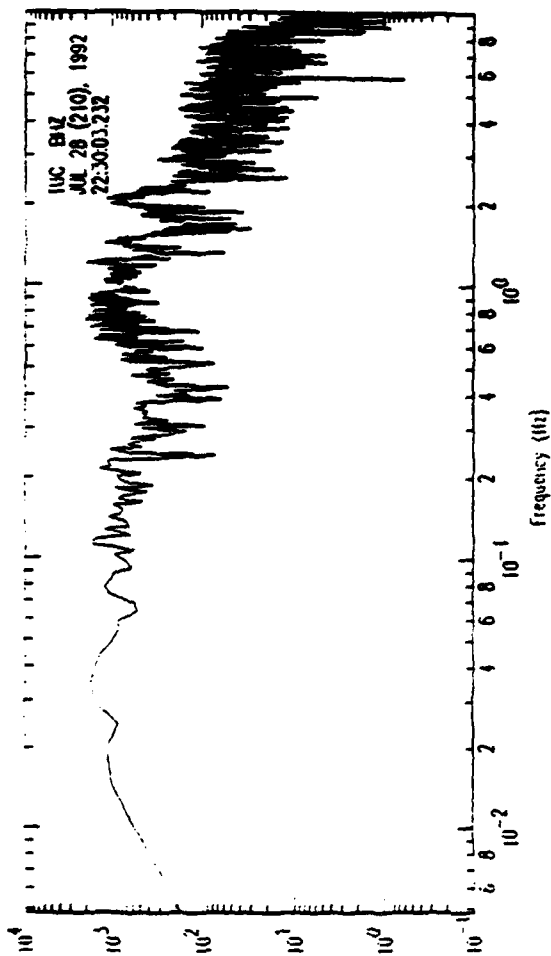
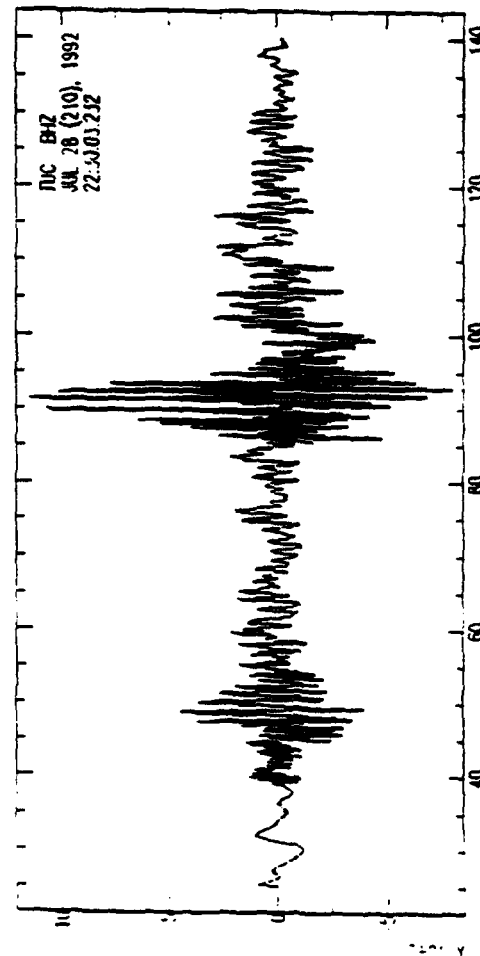
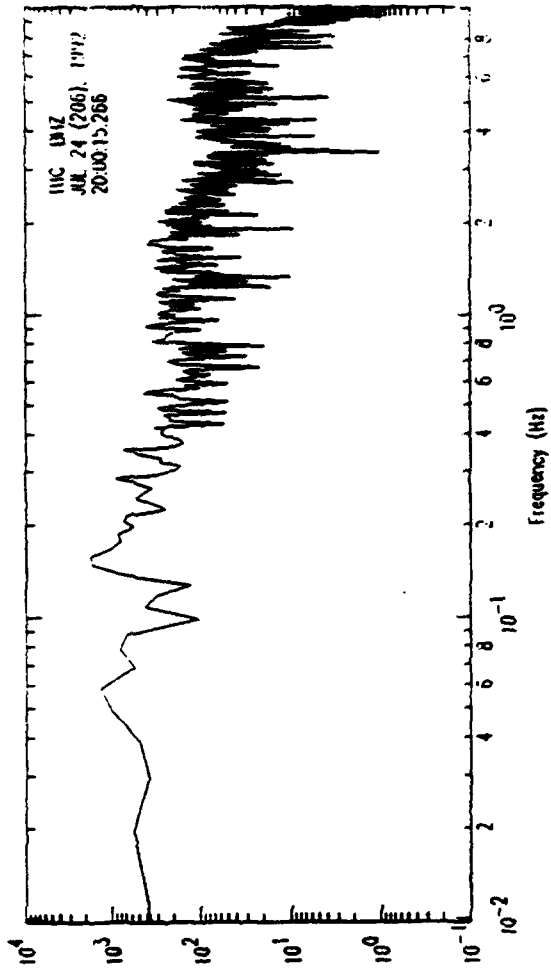
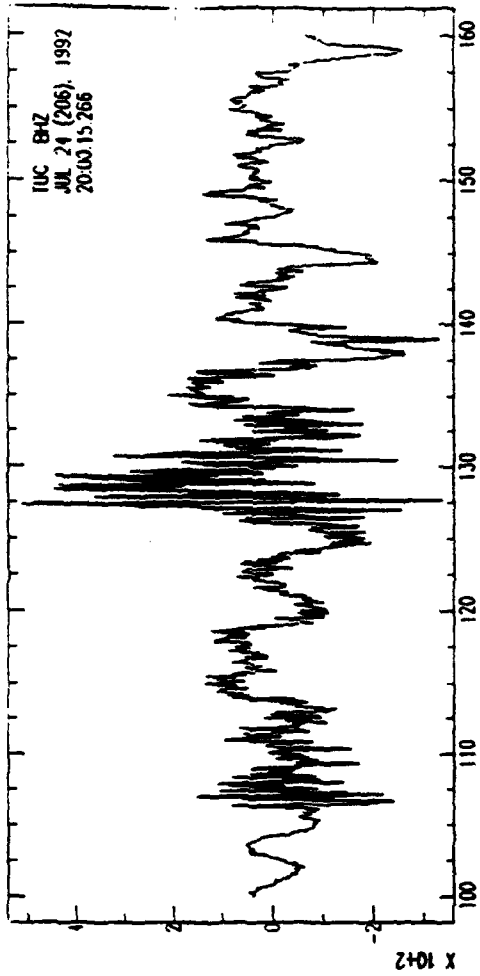


Figure 12

earthquake and explosion. However, if a sonogram is constructed the spectral hole at 3 Hz persists for the explosion ; the significance algorithm assigned this waveform a value of 0.82.

Explosions in stable continental regions: the Midwest US and Europe. We have collected chemical explosion waveforms recorded on the IRIS station CCM (Cathedral Caves, Missouri) and the Graftenberg Array (GRF) in Germany. At present we have cataloged about 80 events recorded on CCM, although all are much smaller than the Southwestern U.S. explosions. We have collected approximately 100 records from 19 different sources from GRF; the largest event was a magnitude 2.8 explosion (see Figures 13a and 13b.)

Preliminary Analysis of Data Bases

Preliminary analysis of waveforms from mine explosions in the southwest United states indicates that characteristic spectral scalloping disappears beyond distances of 890 km. The significance indicator is typically less than .40 at this distance, and the explosions are indistinguishable from shallow earthquakes. Figure 14 summarizes the significance analysis. This is the result of the attenuation of the high frequencies; we also document this effect in the spectral ratio of Pn and Pg phases. Using the Taylor et al. (1988) algorithm which compares a high frequency and a low-frequency pass band (6 to 8 Hz and 1 to 2 Hz, respectively), the Pn and Pg phases both behave similar to earthquakes with like travel paths.

The waveforms collected thus far for stable continental paths indicate that the significance indicator does not drop to a value of 0.40 until 1,050 -1,100 km. We have not yet collected any earthquakes in these regions for direct comparison.

We have correlated the "significance" with a number of parameters such as Pn velocity, roughness of topography, and Sn velocity as a function of distance. Sn velocity appears to be the best indicator of the range over which a scalloping discriminate is effective. For Sn velocities of less than 4.3 km/s the discriminate fails 25% of the time

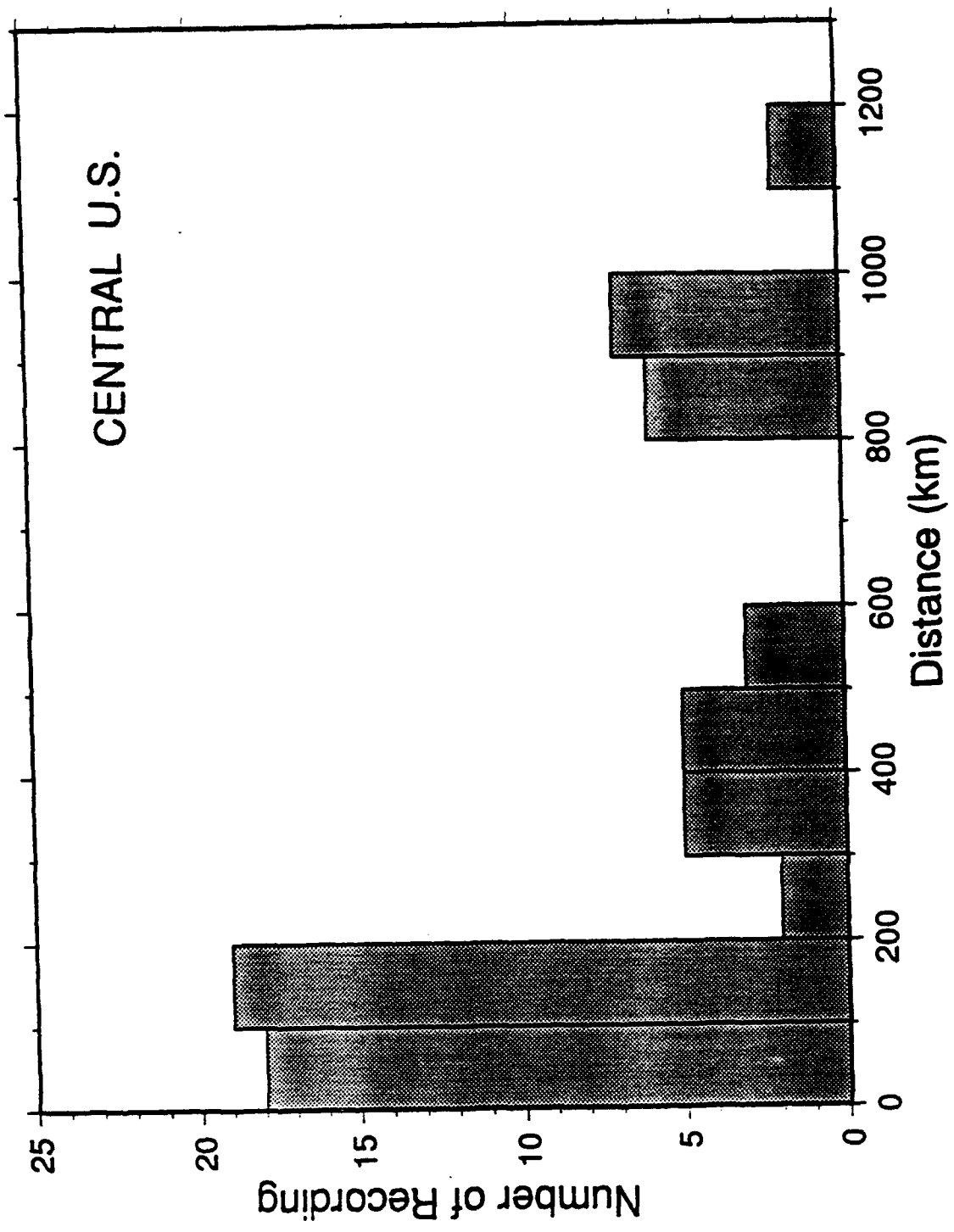


Figure 13a

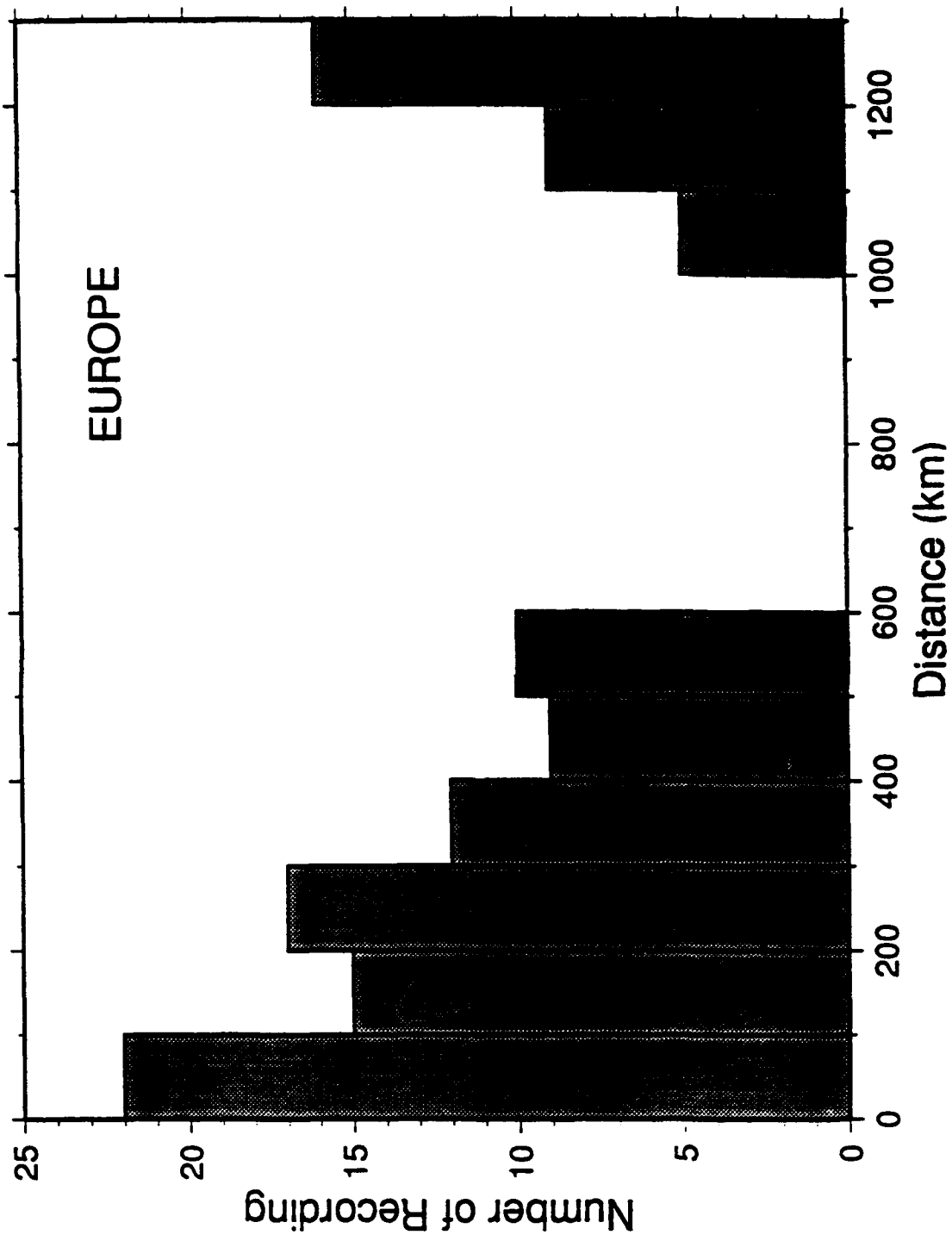


Figure 13b

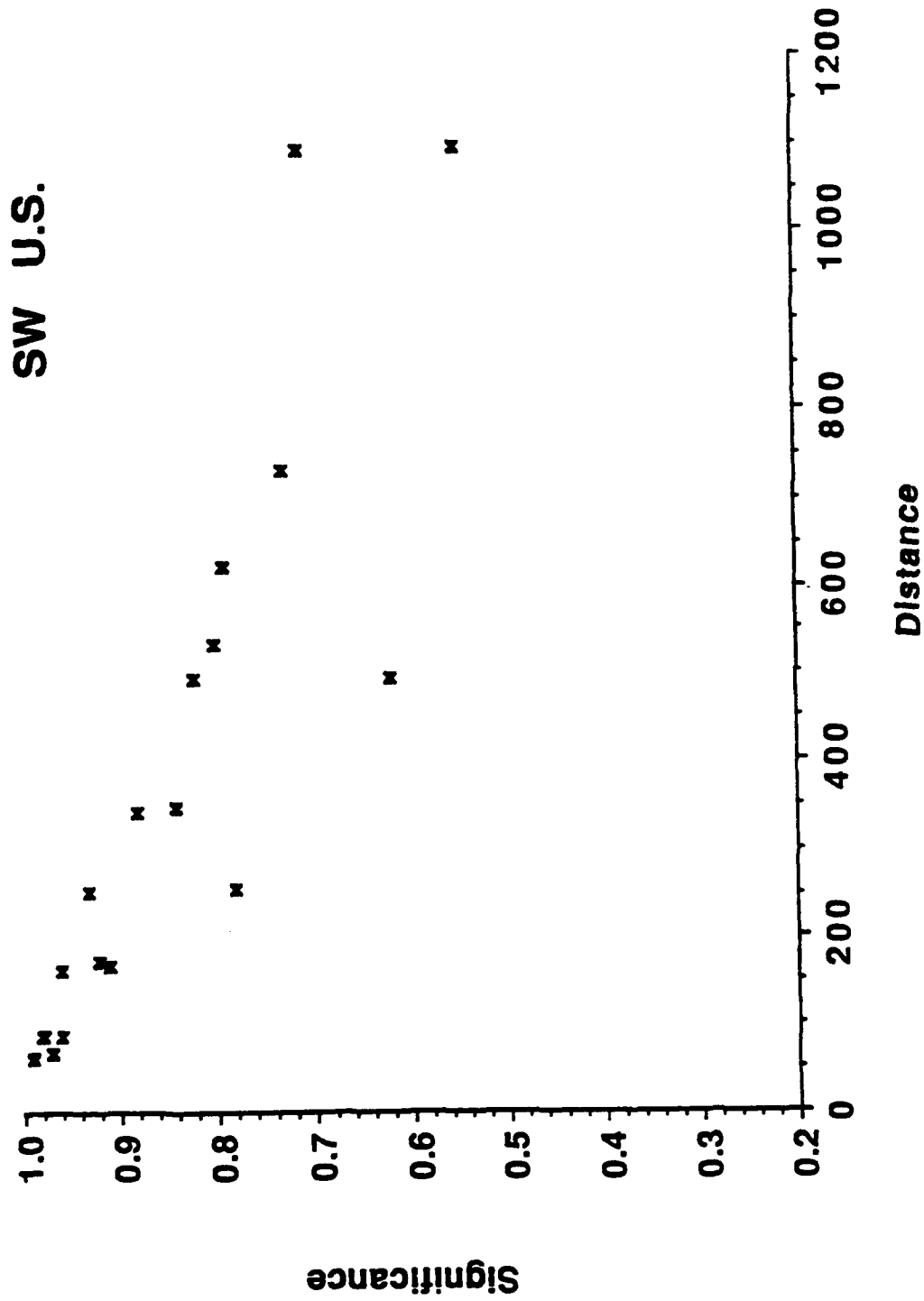


Figure 14

beyond 800 km. For S_n velocities greater than 4.4 km/s, the discriminant fails 25% of the time beyond 1100 km.

References

- Baumgardt, D. R. and K. A. Ziegler (1988). Spectral evidence for source multiplicity in explosions: Application to regional discrimination of earthquakes and explosions, Bull. Seism. Soc. Am., 78, 1773-1795.
- Hedlin, M., J. Orcutt, B. Minster and H. Gurrola (1989). The time-frequency characteristics of quarry blasts, earthquakes and calibration explosions recorded in Scandinavia and Kazakhstan, USSR, in 11th DARPA/AFGL SEISMIC RESEARCH SYMPOSIUM, pp. 40-48, GL-TR-90-0301, ADA229228.
- Smith, A. T. (1998). High-frequency seismic observations and models of chemical explosions: Implications for the discrimination of ripple-fired mining blasts, Bull. Seism. Soc. Am.
- Suteau-Henson, A. and T. C. Bache (1988). Spectral characteristics of regional phases recorded at NORESS, Bull. Seism. Soc. Am., 78, 708-725.

Table 10: Source Locations in the Southwestern U.S.

Source Name	Lat	Long	Elevation	M_L
Cananea	30 57.606	110 19.560	1700	2.4
Chino Pit	32 47.432	108 4.149	2000	2.6
Morenci	33 6.396	109 21.420	1311	2.4
Nacozari	30 19.600	109 33.000	1000	2.1
Pinto Valley	33 27.360	110 53.250	1341	2.3
Live Oak	33 23.160	111 2.292	1280	2.2
Ray	33 10.440	111 0.000	610	2.2
San Manuel	32 41.831	110 41.131	914	2.7
Sierrita	31 52.196	111 8.431	1219	2.1
Tyrone	32 42.576	108 24.127	1829	2.6

Chapter 4

THE EFFECTS OF CRUSTAL STRUCTURE ON SPECTRAL DISCRIMINANTS

Introduction

A comprehensive or low-yield threshold test treaty will require monitoring at regional distances, and the seismograms at these distances are very difficult to deterministically model. The character of the phases Pg and Lg show a very strong dependence on travel path. Although scattering is apparently very important in controlling the character of these phases, the gross features of the crustal waveguide, such as crustal thickness, Pn velocity, and "continuity" of the waveguide, have a strong signature on the efficiency of Pg and Lg propagation. It has been shown that Lg (and to a lesser extent Pg) can be blocked by certain geologic structures such as grabens or mountain ranges. Further, the efficiency of Pn propagation is strongly dependent on the uppermost mantle velocity structure. For these reasons it is important to empirically characterize the efficiency of regional distance propagation in areas in which seismic monitoring is important.

In the final phase of this research we have concentrated on regionalizing the crustal structure in areas around the Western Himalayan syntaxis (Iran, Afghanistan, Pakistan and northwestern India). The crustal structure in this region is extremely heterogeneous; there are signatures of the India-Eurasian collision and the Arab-Eurasian collision. The method we used to invert for the gross crustal structure is that of Wallace (1986) and Holt and Wallace (1990). The P_{n1} waveforms from explosions and earthquakes are strongly affected by the waveguide nature of the crust. If the source terms of the waveform are understood, then a P_{n1} waveform can be parameterized in terms of the average crustal thickness and Pn velocity along a travel path. It is possible to determine these gross parameters using an

iterative, linear inversion which minimizes the differences between an observed and a synthetic P_{n1} waveform. The norm, or error function, used for the inversion is given by:

$$e_i = 1 - \left\{ \frac{\int fg}{\left\{ \int f^2 \right\}^{1/2} \left\{ \int g^2 \right\}^{1/2}} \right\}$$

where f is the observed P_{n1} waveform and g is the corresponding synthetic waveform. The limits of integration correspond to the starting and ending time of the window over which the waveform was inverted (these windows are typically 60-100 seconds). This error function is minimized in terms of average crustal thickness and P_n velocity by using numerical derivatives.

We have been successful in applying this methodology to a number of regions (for example, see Holt and Wallace, 1990) and thus have tested the various trade-offs which may affect the uniqueness of the structure model. Both the crustal thickness and average crustal velocity influence the relative timing of the multiple reflections and mode-converted phases and thus influence the shape of the P_{n1} waveform. A change in crustal thickness will affect the waveform much in the same manner as a change in average crustal velocity (Wallace, 1986). Because of this trade-off, the average velocity is held constant in the inversion, and we solved only for crustal thickness. Another possible source of error in crustal thickness and P_n velocity is the seismic source parameters. In the inversion for crustal thickness and upper mantle velocity, the source is assumed to be known. Most of the sources for the moderate-sized earthquakes used here were obtained from body wave modeling and body wave inversions. Holt and Wallace (1990) showed the regional distance P_{n1} waveforms have a characteristic signature that depends on the source, but small source variations, within the bounds of uncertainty from body wave modeling or

inversion have little influence on the P_{nl} waveform, and accurate estimates of crustal thickness and P_n velocity can usually be obtained.

Crustal Structure of the Western Syntaxis

Figure 15 shows the study area, the seismic stations, the earthquakes used and a series of blocks used to regionalize the region. The blocks were partitioned on the basis of topography, geology and path coverage. A total of 32 earthquakes in the Hindu Kush, Pamirs, Zagros, Turkey and the Quetta syntaxis recorded at 4 WWSSN stations were used for the regionalization. The average crustal thickness and upper mantle velocity were determined for each block by performing a linear weighted least squares inversion using the crustal thickness and P_n velocity results for the individual paths. The average thickness and slowness ($1/P_n$) of a given path are assumed to be the sum of the fraction of path length in a given block multiplied by the thickness or slowness of the block:

$$X_j = \sum_{i=1}^n X_i d_{ij}/D_j$$

where X_j is the average crustal thickness or slowness obtained from each inversion of the P_{nl} waveform that travel path j , X_i is the same parameter for block i , d_{ij} is the distance travel in block i by raypath j , and D_j is the total raypath length. The *a priori* variance-covariance matrix is assumed to be a diagonal matrix composed of the variance from crustal thickness and the slowness obtained from the individual inversions for each path. Holt and Wallace (1990) have determined that errors in crustal velocity of ± 0.1 km/s can lead to errors in crustal thickness estimates of $\pm 5\%$ of the true thickness. On the basis of experience with inversions in the Tibet and China region, it is assumed that the average standard deviations for crustal thickness and P_n velocity are ± 2.5 km and ± 0.1 km/s

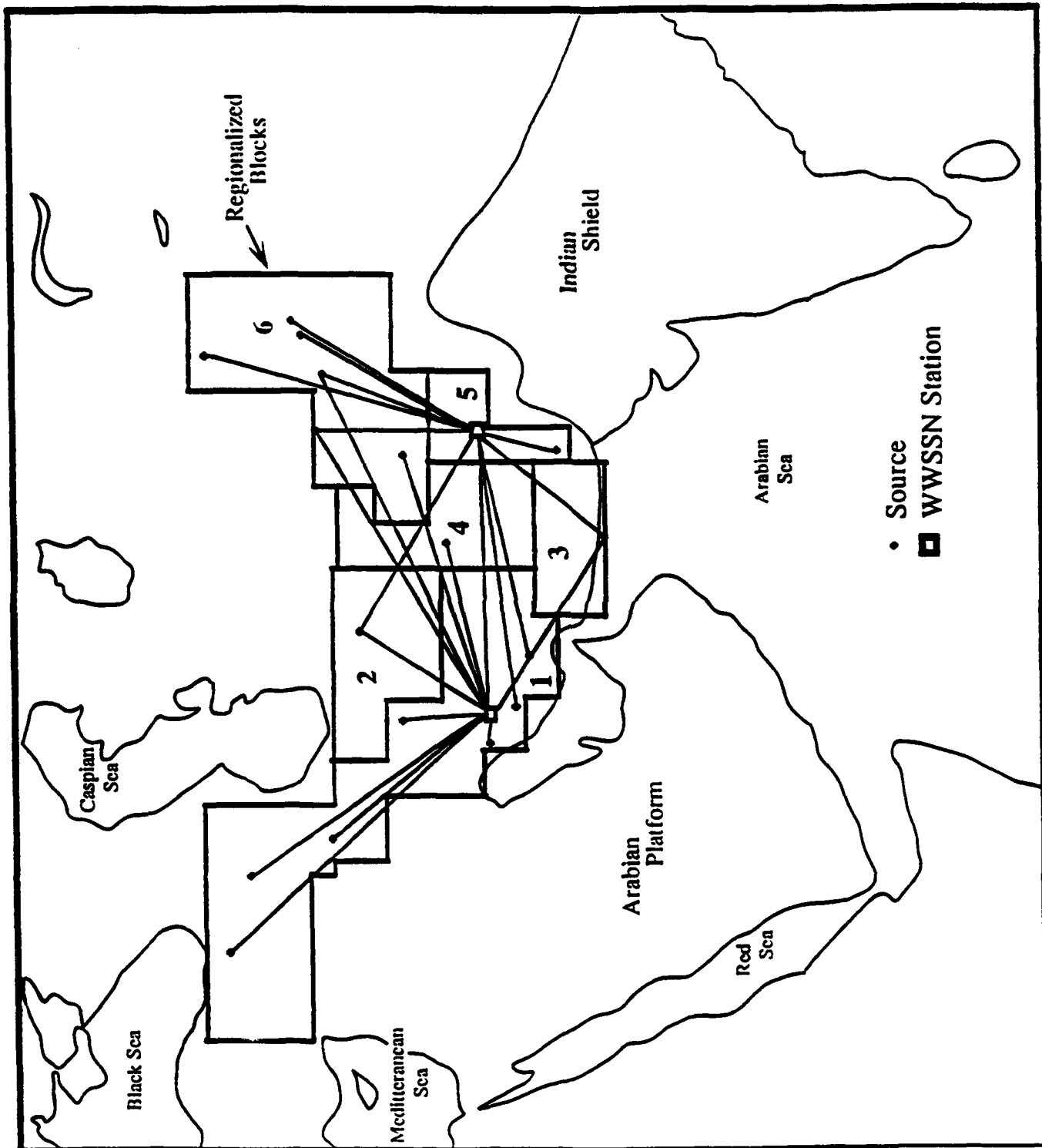


Figure 15

respectively. Uncertainties in Pn velocity are due to errors in origin time of hypocenter location.

Figures 16 and 17 summarize the results of the regionalized inversion. The standard deviation of each parameter was obtained from a *posteriori* model variance-covariance matrix after the inversion was performed. Block 1, which is dominantly south of the Zagros has a crustal thickness of 33 km. Block 2 is in central Iran and is associated with the Zagros. Although the crustal thickness is the most poorly resolved of any block, the value of 60 km is consistent with the collision zone. Central Iran is believed to be relatively rigid (Jackson and McKenzie, 1984), with a very low level of seismicity. There is considerable evidence for crustal shortening in the Kopet Dag. If thickening accompanies this shortening, the crust should be overthickened. The Pn velocity is very high for this region, and, as will be discussed later, the Pn and Sn propagation appears to be very efficient, but the Lg propagation is at least partially blocked.

Block 3 is a region known as the Makran, and there is documented subcrustal seismicity in this region indicating that the Arabian plate is being underthrust beneath Eurasia (Ni and Baraznagi, Quitmeyer et al., 1979). This underthrusting is consistent with the value of 56 km we obtained for the crustal thickness; the low Pn velocity indicates that the uppermost mantle is at elevated temperatures. Block 4 encompasses the Helmond Basin (in regions into the southern USSR), and the inversion results are similar to those obtained for the Makran. Block 5 is the Quetta Syntaxial region. The crust here is relatively thin (30 km) and the Pn velocity is very low (7.5 km/sec). At first glance this would seem inconsistent with a zone of convergence, but the Chaman fault is a major left-lateral fault which may accommodate the collision. Finally, block 6 which is in the Hindu Kush and Pamirs, has an extremely thick crust (75 km) and a high Pn velocity (8.2 km/sec). This is consistent with other studies of the region (for example, Holt and Wallace, 1990).

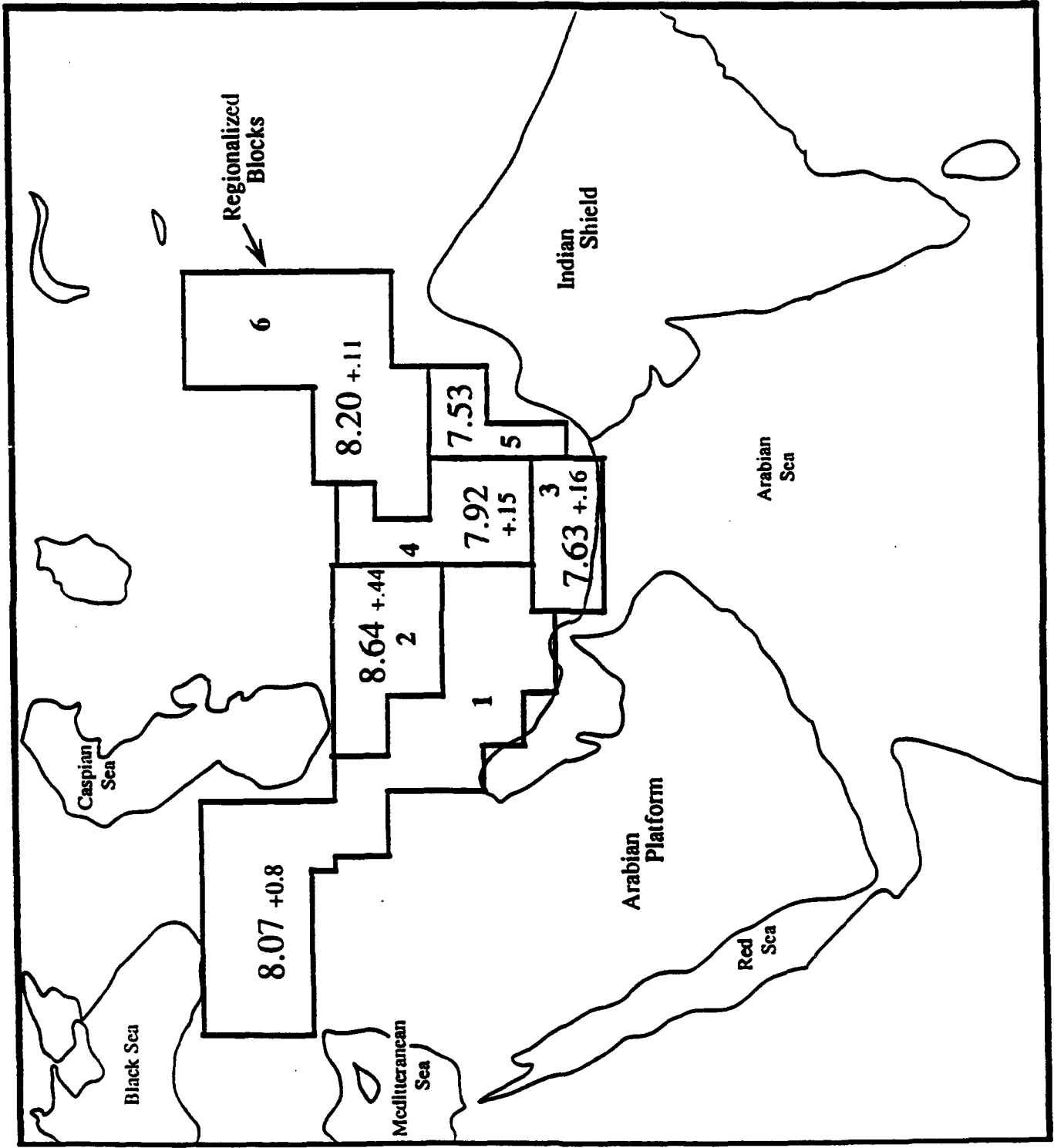


Figure 16

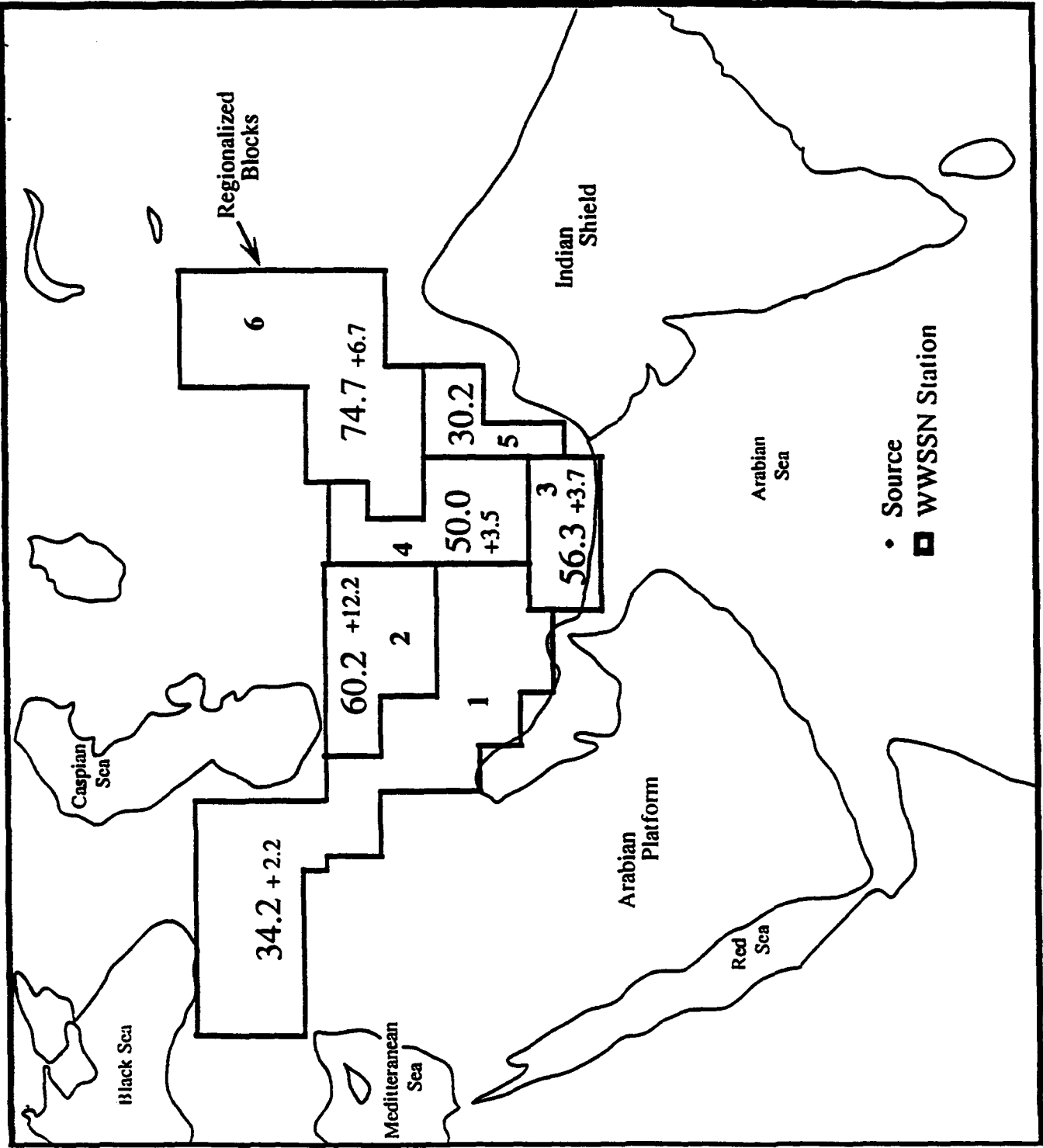


Figure 17

We investigated the efficiency of the propagation of Lg and Pg several ways. The first method is based on the empirical algorithm of Kennet et al. (1985). Each Lg train is assigned a numerical code on the basis of Lg appearance. Although the size of the Lg packet is not simply related to the nature of the crustal structure along the path, the largest effects (such as blockage) come from prominent structural heterogeneity. A similar empirical approach is used to assess Pg efficiency. The installation of two very broad band seismic stations in the Soviet Union allowed us to also assess the efficiency of propagation more rigorously. An envelope function was fit to Pn, Sn, Pg and Lg; these envelopes were calculated at 1, 3 and 5 Hz. The ratio of the envelope functions for Pg and Pn was used to calculate the relative efficiency of Pg. Similarly, the ratio of Lg to Sn was used to calculate the efficiency of Lg.

Figure 18 summarized the Lg efficiency. Paths which traveled through relatively constant thickness crust (for example, blocks 2, 4, and 3) were fairly efficient. As expected, when paths crossed regions of rapidly varying crustal thickness, the Lg was much diminished. For example, ray paths from the Hindu Kush to Quetta syntaxis were nearly devoid of Lg. Similarly, earthquakes in southern Iran recorded at ASH (only two events studied thus far) had poorly developed Lg. Figure 19 summarizes the Sn efficiency (from Kadinsky-Cade et al., 1981). Again, crustal thickness heterogeneity plays a role in the efficiency of propagation, although the correlation is much less well developed. For example, the Pg phase is much more efficiently propagated for the Hindu Kush to the Quetta syntaxis than Pn. This is probably the result of very low Pn velocities in block 65 (as associated high attenuation of the uppermost mantle.)

Summary

The crustal thickness has a strong effect on the character of short-period regional phases. With the improved models developed from crustal and upper mantle structure present in the Western Syntaxial region presented here, it is possible to predict the

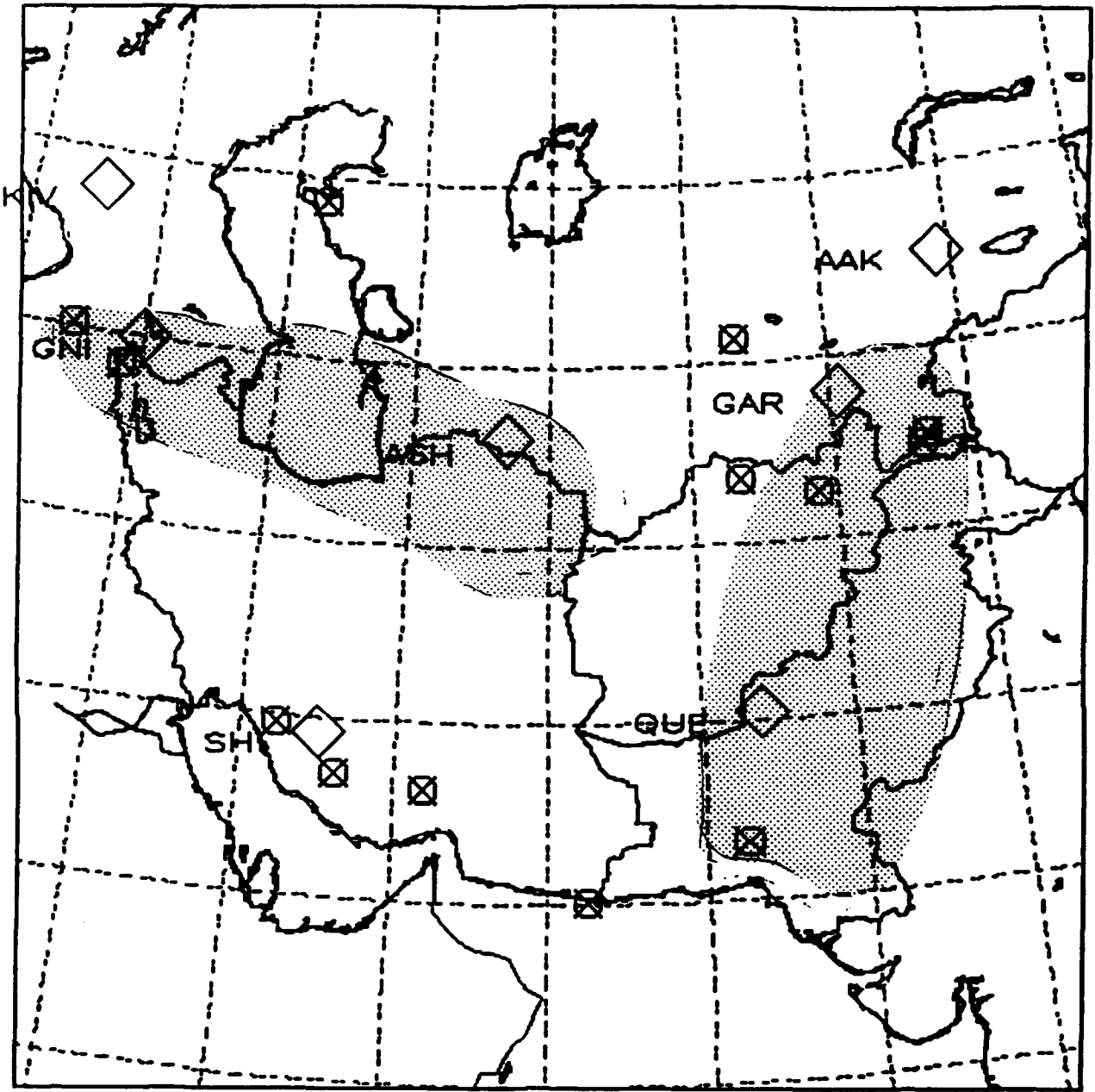


Figure 18

character is signals for events of interest in the Soviet Union or India and Pakistan. Clearly Lg and Pg do not necessarily have similar propagation characteristics, and spectral discriminate methodologies should take this into consideration.

Future work will rely on the digital data from the GSN and the new Soviet stations. The envelop function developed for this study appears to yield a very good measure of the efficiency of propagation for regional distance phases.

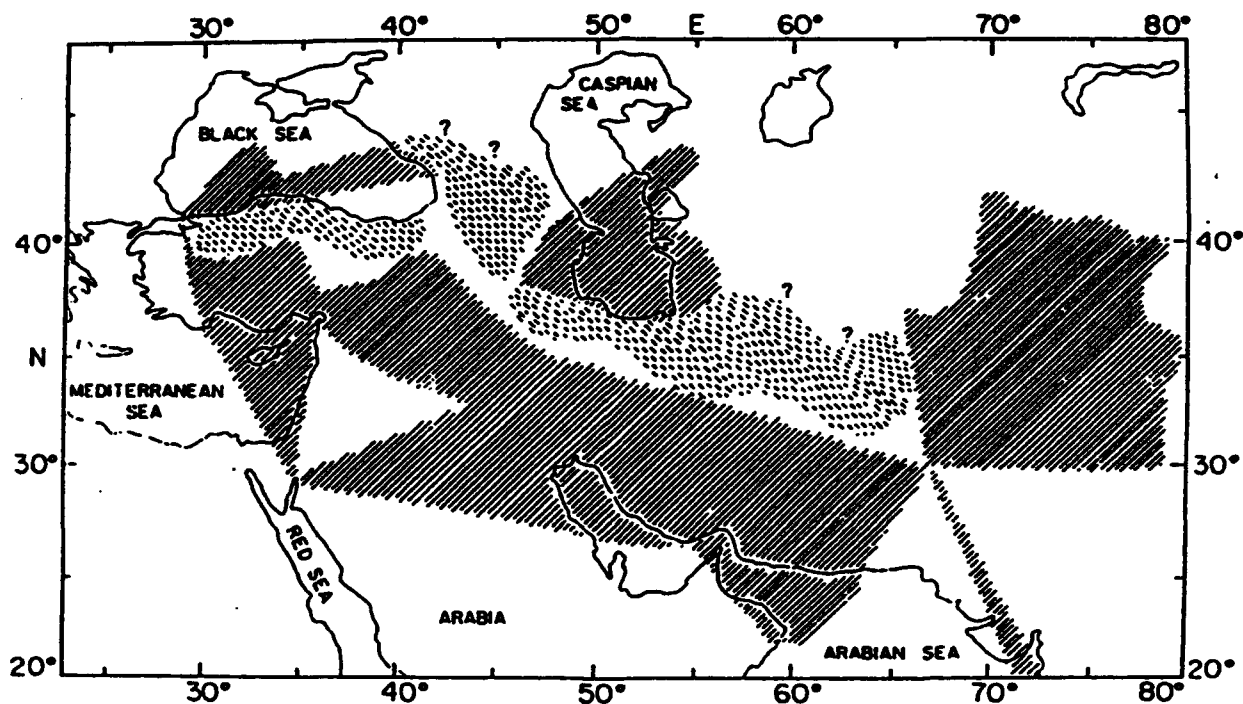


Figure 19

References

- Holt, W.E. and T.C. Wallace (1990). Crustal thickness and upper mantle velocities in the Tibetan Plateau from the inversion of regional P_{nl} waveforms: evidence for a thick upper mantle lid beneath southern Tibet, J. Geophys. Res., 95, 12,499 -12,525.
- Jackson, J.A. and D.P. McKenzie (1984). Active tectonics of the Alpine-Himalaya Belt between western Turkey and Pakistan, Geophys. J.R. astr. Soc., 77, 185-264.
- Kennett, B.L.N., S. Gregersen, S. Mykkeltveit and R. Newmark (1985). Mapping of crustal heterogeneity in the North Sea Basin via the propagation of Lg waves, Geophys. J. R. astr. Soc., 83, 299-306.
- Ni, J. and M. Barazangi (1986). Seismotectonics of the Zagros continental collision zone and a comparison with the Himalayas, J. Geophys. Res., 91, 8205-8218.
- Quimyer, R.C., A. Farah and K. Jacob (1979). The seismicity of Pakistan and its relation to surface faults, in *Geodynamics of Pakistan*, editors, A. Farah and K. Delong.
- Wallace, T.C. (1986). The inversion of long-period regional distance body waves for crustal structure, Geophys. Res. Let., 13, 749-752.

CHAPTER 5

THE SEISMOTECTONICS OF THE LOP NOR, XINJIANG PROVINCE PEOPLE'S REPUBLIC OF CHINA

Introduction

Underground nuclear explosions detonated at the Lop Nor test site have varying degrees of nonisotropic seismic radiation. Four events (May 21, 1992, $m_b = 6.6$; August 16, 1990, $m_b = 6.2$; June 5, 1987, $m_b = 6.2$; October 3, 1984, $m_b = 5.7$) produced strong regional distance Love waves which have an azimuthally dependent amplitude variation consistent with that expected for a double-couple source. We have interpreted these in terms of tectonic release. The May 21, 1992, event was the largest underground explosion to occur since 1977; the tectonic release was large enough such that the Harvard CMT project was able to recover a double-couple component corresponding to $M_W = 5.2$ (Ekstrom, personal communication, 1992).

Historically, the area around the Lop Nor test site has had a very low level of seismicity. Since the first underground test (September 22, 1969, $m_b = 5.2$), only 23 earthquakes have been reported in the PDE to have occurred within a 200-km radius of Lop Nor. Most of these events were too small to be well recorded on the global seismic network. Since the late 1980s, a new digital seismic station has been operating in Urumqi (WMG), the capital of Xinjiang Province, ~260 km away from the test site. In this study we have collected the regional records for 14 earthquakes recorded at WMQ to detail the focal mechanisms of the events around the Lop Nor test site and explore the relationship between the tectonics of the Tarim Basin and tectonic release from underground nuclear explosions.

Lop Nor Test Site

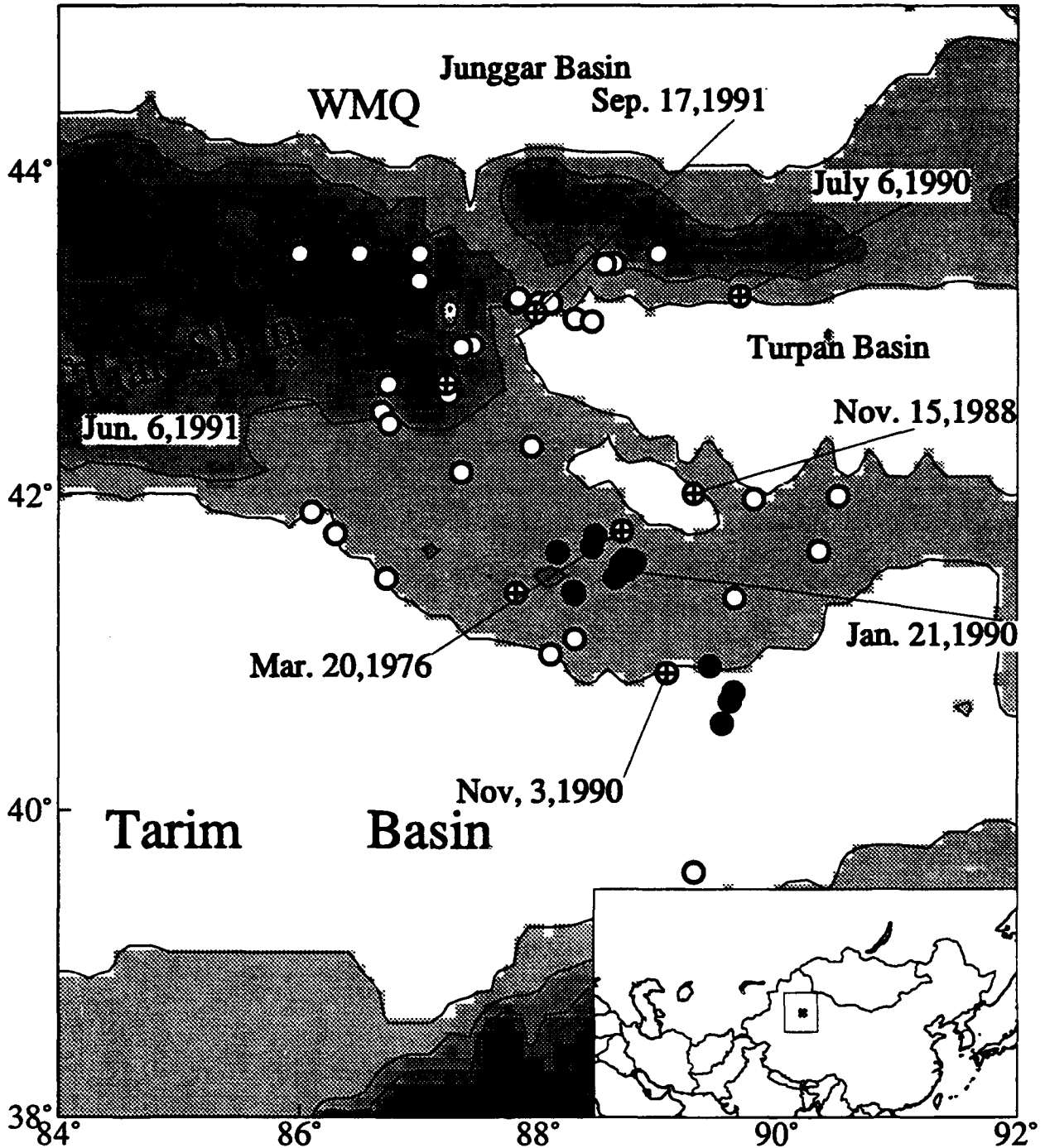


Figure 20. Topographic map of the area around the Lop Nor Test Site. The interval of the contour lines is 1000m. The inset shows the geographic location of the map. The black dots are the unclear explosions which began in 1964. The black dots in the south are the atmospheric explosions, while those in the north are underground nuclear explosions. The open circles are the epicenters of the earthquakes with a total number of 25 since 1950 within 200 km around the Lop Nor. The open circles with a cross are the events we studied in this paper. The open triangle is the CDSN station WMQ.

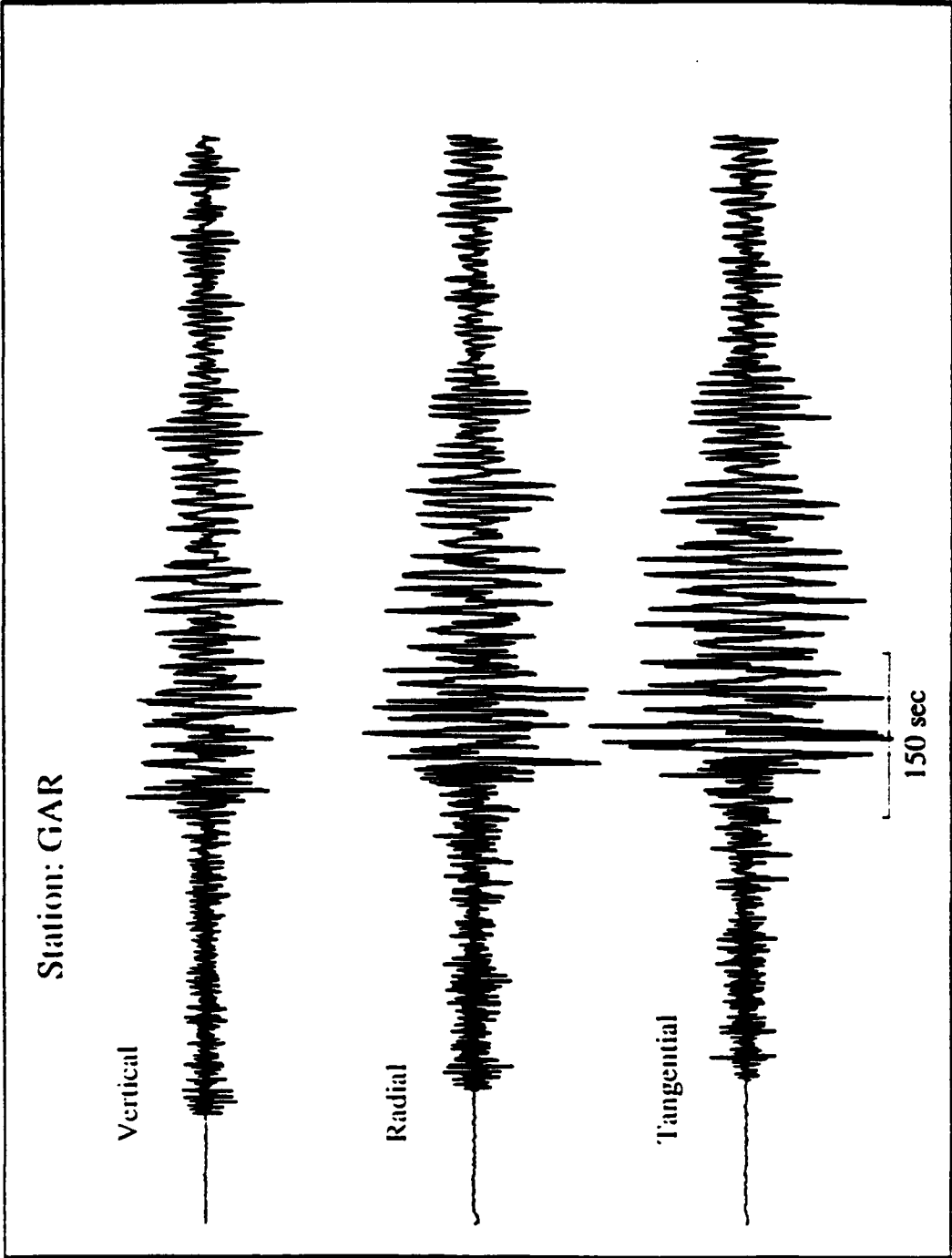


Figure 21a

May.21,92 (SH dis)

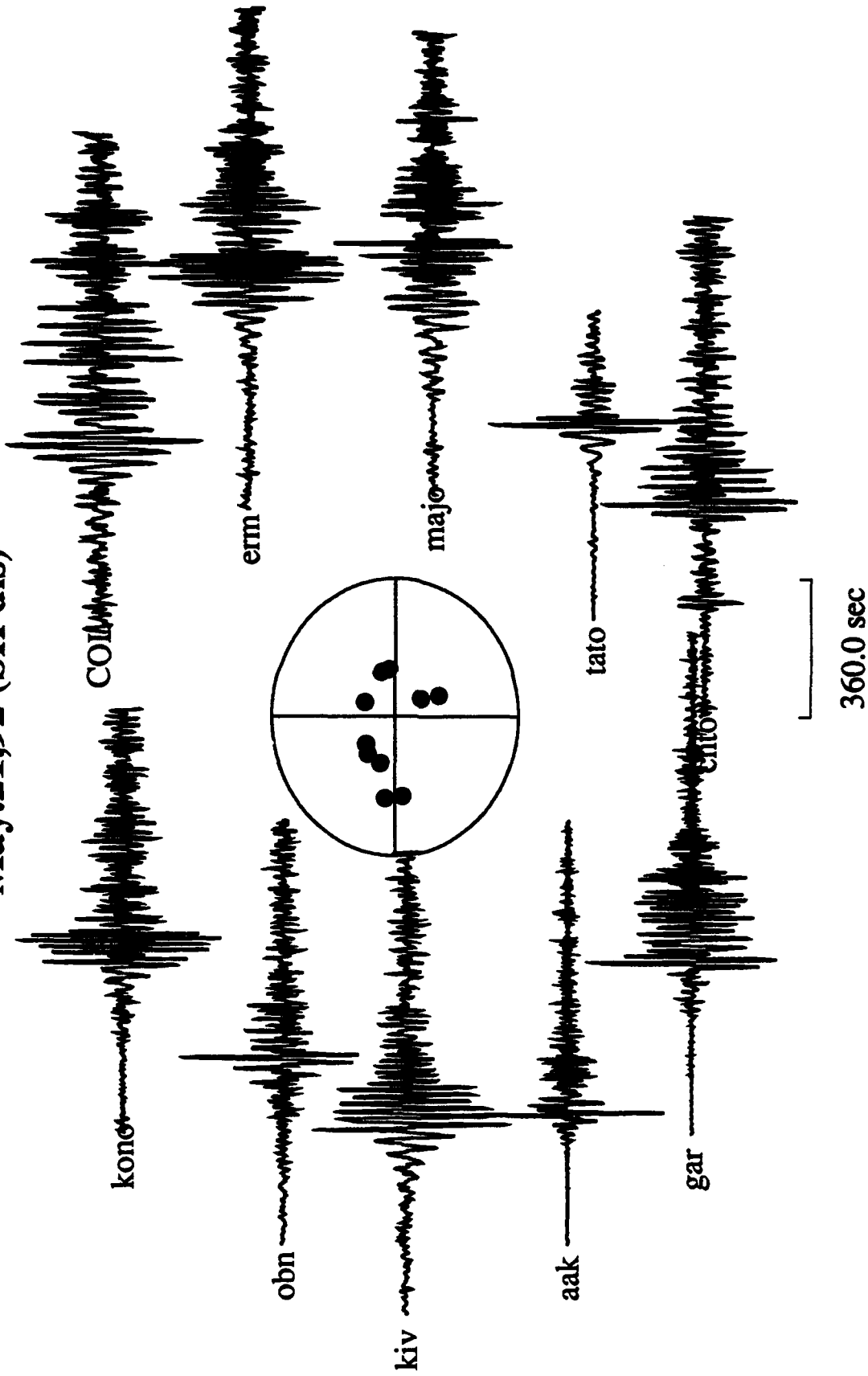


Figure 21b. The latest and the largest explosion in Lop Nor (M-6.6) was very well recorded world wide. At all azimuths, there is a large love wave (Tangential component). The records shown are filtered to 20 seconds.

Most of these underground nuclear explosions have non-isotropic component. Figure 21b shows some of the tangential records for the explosion on May 21, 1992, the largest nuclear explosion in last 15 years. At almost all the azimuths, the Love waves are very large and coherent at periods of 20 seconds.

Geological and Geophysical background

Lop Nor is located in Northeast corner of Tarim basin, Xinjiang province, China (Figure 20). The Tarim Basin is a rigid block of Precambrian and Paleozoic rocks which has survived relatively undeformed during the ongoing collision between Indian and Eurasian Plates. Most of the Tarim Basin is covered with a Quaternary sedimentary sequence. Within the vicinity of the Test Site this cover is very thin (a few meters to 10's of meters thick), and Paleozoic "hard" rocks are exposed [Matzko, 1992]. But at some other places in the basin, the bedrocks is buried as deep as 13-16km [Lithospheric Dynamics Atlas of China]. The southern edge of Tarim Basin is the north margin of Tibetan Plateau with average elevation of 5 km and north of the basin is the Tian Shan mountain belt. The evolution of Tarim basin is closely related to the evolution of the Tibetan Plateau to the south and Tian Shan to the north [Molnar and Tapponiar 1971, 1975 etc.]. The detailed geological history of the Tarim basin and adjacent areas such as Tian Shan, Junggar basin and Kunlun mountain range in northern Tibetan Plateau is not well known. but according to some of the geological studies [Carroll et al., 1990; Hendrix, et al., 1992; Feng, 1985], the structure and the topographic features of this area are the result of a series of the collisions throughout the Phanozoic time.

Since Late Paleozoic time, the entire Xinjiang area has undergone several deformation cycles. The Junggar Basin was the Junggar ocean during the Paleozoic; it was formed as a foreland basin adjacent to a subduction zone to the south (Tian Shan) at Late Paleozoic time

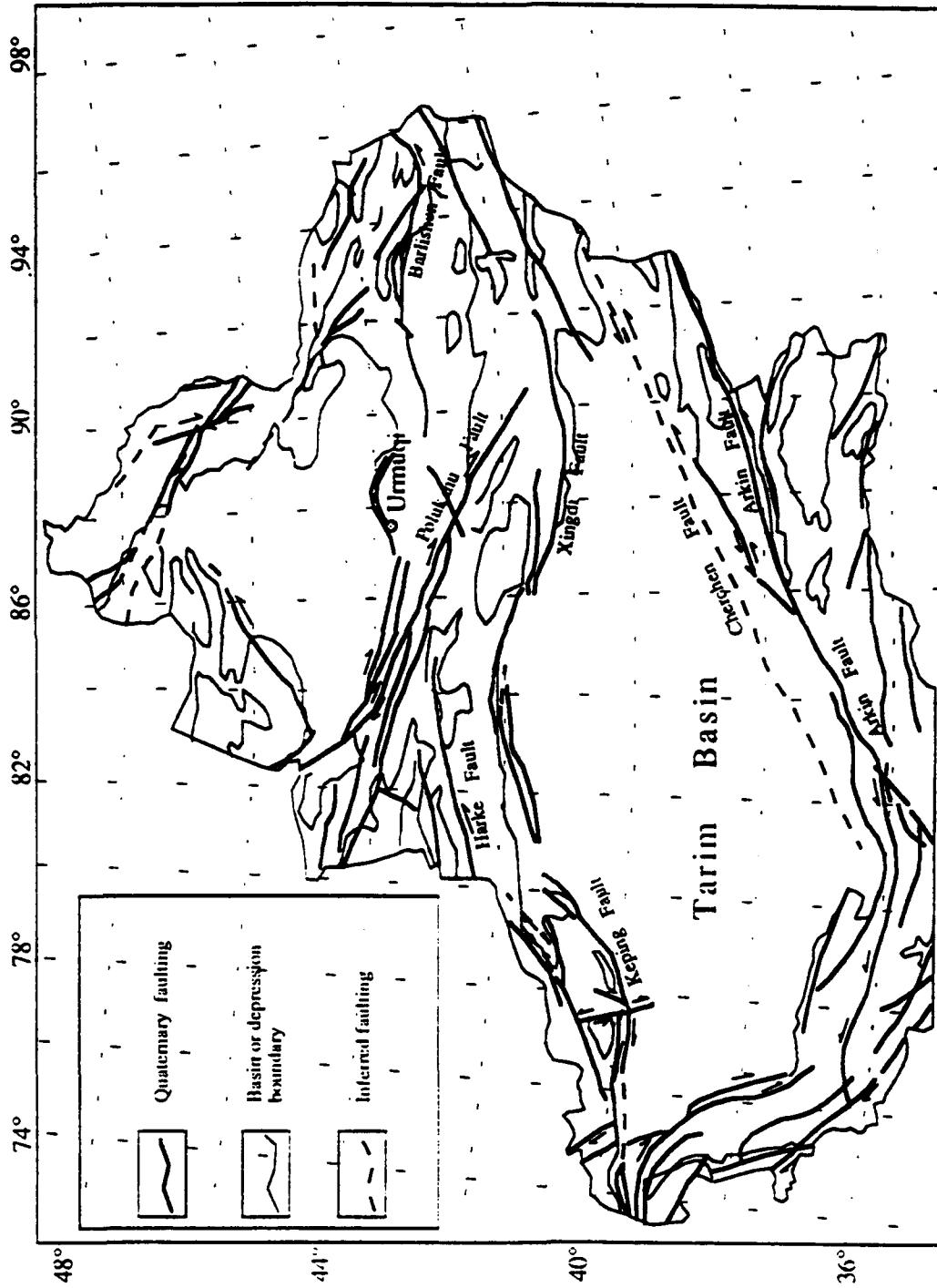


Figure 22

[Carroll, et al., 1990]. The initiation of the Tian Shan mountain range may be the result of the arc system and the subduction. The collision between the Tarim block and Siberia blocks (including Junggar basin and arc system at south--Tian Shan) enhanced the size of Tian Shan [Hendrix, et al., 1992] and at the same time the Tarim block had undergone clockwise rotation [Li, 1990; Li, et al., 1991; Enkin, et al., 1992]. During the Mesozoic time, there was some type of mountain ranges in the Tian Shan area providing the depocenter for both of the Junggar basin and Tarim basin [Hendrix, et al., 1992]. Throughout much of the Mesozoic era, the Tian Shan may have had several large-displacement strike-slip faults. This is similar in many ways, to the modern Tian Shan fault system and it is likely that a series of reverse and/or thrust faults bounded the range on either side [Hendrix, et al., 1992]. The Cenozoic collision between Indian Plate and Eurasian Plate accelerated the uplifting of the Tian Shan and subsidence of the Tarim and Junggar basin and reactivated the fault systems in Tian Shan area.

The detailed uplifting history of Tian Shan is not well known, Although it has been postulated that the part within the Chinese border seems to have achieved its topography relatively recently [e.g. Feng, 1985]. Unlike the Himalayas which are thought to have experienced rapid uplift in the Miocene [Harrison, et al., 1992], the massive uplift of the Tian Shan range maybe much later [Feng, 1985]. It might have started at the Eocene, when the Indian Plate collided with the Eurasian Plate but the uplift rate was very slow. Uplift in Tian Shan accelerated in the early Pliocene [Feng, 1985]. This rapid uplift accompanied by extensive faulting at the edge of the mountain range. There was deposition of a thick pile of conglomerate in the foot hills of Tian Shan. It is not known whether this deposition episodes were caused by rapid erosion or severe weather change.

By analyzing the geomorphic features of the fault system in Xinjiang area, Feng [1985] also pointed out that, at the end of the early Pleistocene, large scale deformation of these

deposits occurred, most of which were tilted and folded due to the N-S compression. In the northern Tian Shan, the dip angle is 10° - 20° , but at some area in southern Tian Shan (northern Tarim basin), the dip angles reach 80° . At Kunlun (southern Tarim basin), the dip angles are 30° - 40° . From Mid-Pleistocene the mountain ranges are characterized by episodic uplifting, forming many valleys cut by rivers. Some of the well developed ancient river beds are above the current river drainages by 40-80m. Some of these river beds are tilted by faultings, dip angles are about 14° .

Despite of all of the controversy on the detailed history of the area, one thing seems to be in common: the fault system in Tian Shan area generated during the collisions at Late Paleozoic and Mesozoic time has undergone both reverse/thrust and strike-slip motions to accommodate the collisional convergence. Many of the faults are still active today [Carroll, et al, 1990; Hendrix, et al, 1992 and Feng, 1985]. Most of these faults are parallel of the topography, trending W-E or in a NW-SE direction. By studying the earthquakes and geomorphologic features on these active faults, Feng [1985] has summarized that they can be characterized by two types: 1) Thrust faulting and 2) strike-slip faulting. The thrust faults are mainly in Tian Shan, parallel to the trend of the mountain range in W-E direction. The strike-slip faults are mainly in NE-SW, N-S or NNW-SSE direction and have right lateral motion. Some of these faults have been reactivated many times during Cenozoic.

Lop Nor test site is located in the eastern tail of the Tian Shan range, at the transition zone from the basin to the mountains. Historically, Lop Nor region has a relatively low rate of seismicity within 200 km of the test site. From 1950 to 1992, only 23 earthquakes have been located by the PDE or ISC and most of them are small ($M_s < 5.1$). Most of the fault mechanisms are reverse faults although some have oblique right lateral shear motion.

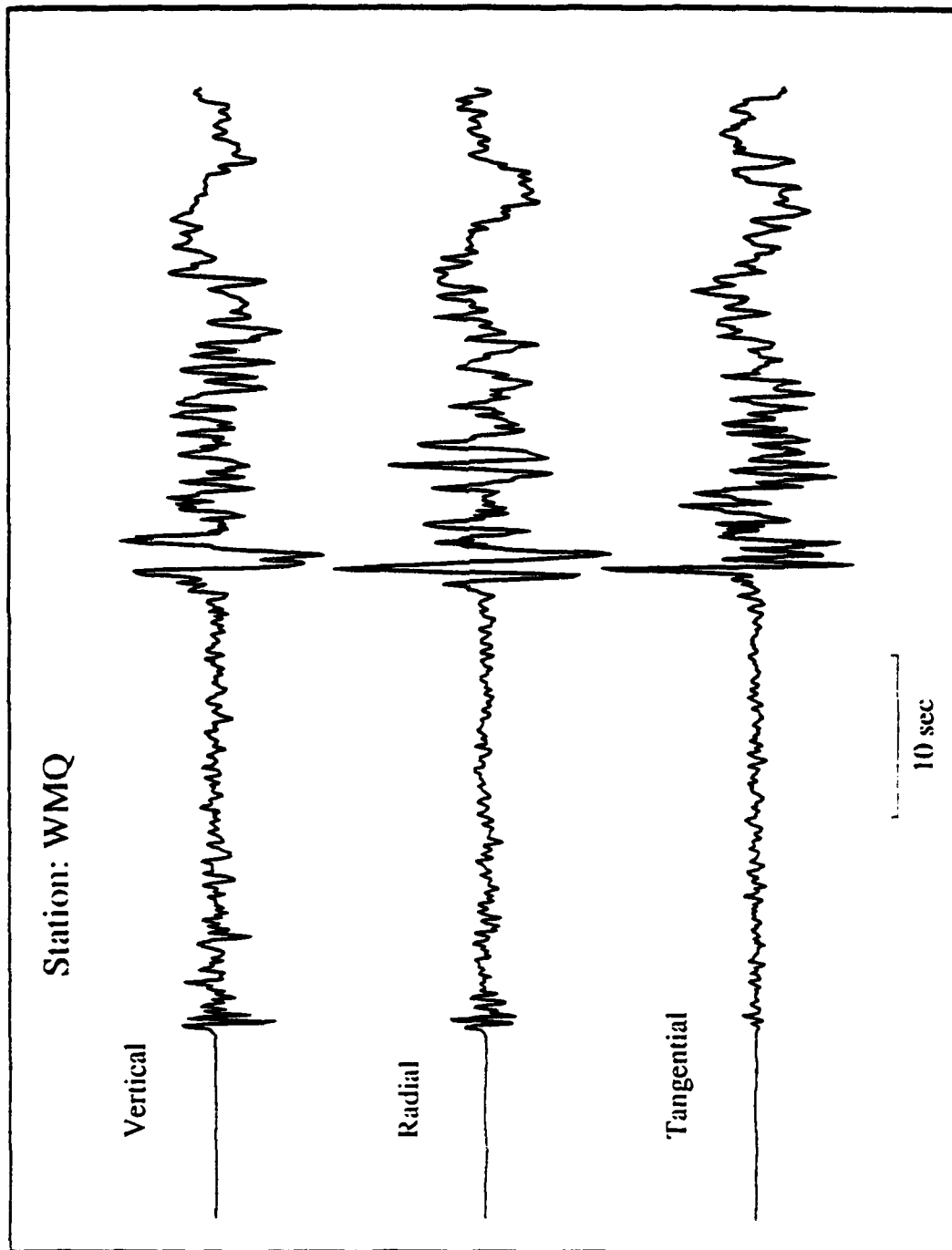


Figure 23

The Earthquakes Around Lop Nor

SSMT results:

Most of the earthquakes in Lop Nor are in magnitude range of $M_b = 5.3$ or less. They are too small to be well recorded at teleseismic distance, but many were very well recorded at regional distance. Figure 23 shows a typical regional recording at station WMQ of an earthquake which occurred near Lop Nor. In this study, we collected 6 events within 200 km around the Lop Nor test site and very well recorded at the station WMQ (distance ~ 250 km). We use the Single Station Moment Tensor inversion method (SSMT) [Fan and Wallace, 1991; Gao and Wallace, 1992] to study the focal mechanisms of these events. The parameters of these events are listed in Table 11.

Regional distance body waves, the Pnl waves, are very useful in determining the earthquake source parameters [e.g. Helmberger and Engen, 1980; Wallace, et al., 1981, 1982; Wallace, 1985; Xu et al., 1989; Gao and Wallace, 1993]. If the regional data is of very high quality (Broad band, high dynamic range), the source parameters can be obtained by inverting the three components of a single station records [Langston, 1982; Ekstrom, et al., 1986; Jimenez, et al., 1989; Fan and Wallace, 1991]. Fan and Wallace [1991] have illustrated that the 3 components of a single regional station seismic records can be used to determine the focal mechanisms, this algorithm works especially well for small and intermediate earthquakes. By assuming a point source and a simple source time function scaled to earthquake size, five Green's functions corresponding to the five elements in the moment tensor can be constructed, then the five moment tensor elements can be inverted in a least square sense by the SVD (Single Value Decomposition) method. The seismic phases arriving at a regional seismic station ($3^\circ < \Delta < 13^\circ$) are of relatively low frequency, and somewhat insensitive to the regional velocity structure. Most the seismic rays in the travel path are the head waves and multiple reflections between the earth surface and the Moho (Pnl waves) [Wallace, 1985, 1986; Xu, et al., 1989]. The velocity structure in Tian

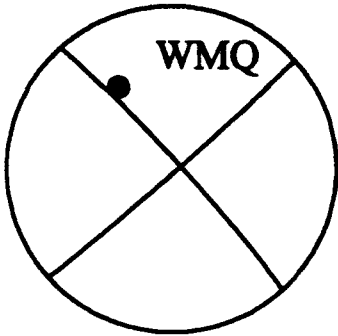
Table 11. Earthquake locations around Lop Nor

Event (No.)	OT (PDE)	Epicenters (PDE)		Magnitude
	Date, hour:minute:sec	Lat (N°)	long(E°)	
Event 1	Mar. 20, 1976, 4:34:3.6	41.783	88.697	5.1
Event 2	Nov. 15, 1988, 16:56:46.2	42.018	89.295	5.3
Event 3	Jan. 21, 1990, 7:53:31.9	41.534	88.728	4.6
Event 4	July 6, 1990, 17:22:50.3	43.240	89.681	4.2
Event 5	Nov. 3, 1990, 17:25:13.8	40.882	89.071	5.1
Event 6	June 6, 1991, 8:2:7.5	42.705	87.221	5.1
Event 7	Sept. 17, 1991, 18:53:22.2	43.141	87.968	4.8
Event 8 *	Feb. 26, 1987, 19:56:35.5	38.01	89.15	6.4

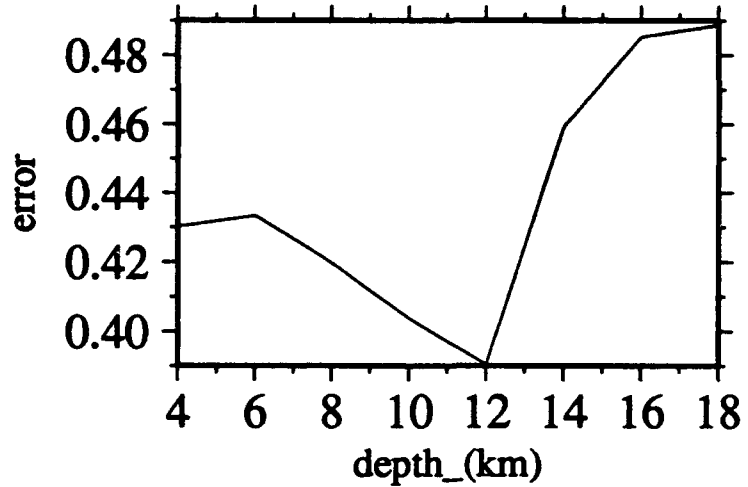
* -- From Xu, et al, 1989.

Shan and Tarim Basin is no doubt complex, with the thickness of the crust varying from 45 km in the central of the Tarim Basin and 55 km at the edge of the basin [Lithospheric Dynamics Atlas of China]. Although a 40 km thick crust is enough to fit the gravity data [Lyon-Caen and Molnar, 1984], surface wave dispersion studies give a much thicker crustal thickness ~ 62 km [Zhu. et al., 1982]. The receiver function studies at the station WMQ indicate a 55 km thick crust [Mangino and Ebel, 1992]. Similarly, Pn velocity varies from 8.0 to 8.2 km/s [Zhu, et al., 1982; Mangino and Ebel, 1992]. But for source parameter study, a very simple model is sufficient to fit the waveform [e.g. Wallace 1984; Xu, et al., 1989], since the waveform is much more sensitive to variations in the source orientations. We use a simple model with a crust over a half space; the thickness of the crust is 50 km with P wave velocity 6.1 km/s, S wave velocity 3.4 km/s, density 2700 g/cm³ and an average Pn velocity is 8.0 km/s, Sn velocity 4.4 km/s, density is 3300 g/cm³ in the mantle. The Green's function are calculated separately by Generalized Ray Method at a suite of hypocentral depths. In the inversion, there is an iteration over depths and the RMS (Root Mean Square) errors calculated. The best depth is chosen based on the minimum error (Figure 24a). If the values of the error are similar, a depth is picked to correspond to the depth where three moments from the three components are in closest agreement. In this study, we use the absolute value of the data (Earth displacement in meters) in the inversion. Thus, no objective functions are used. Figure 24a shows the displacement waveform fits for the inversion of Event on Nov. 15, 1988. Gao and Wallace [1993] have illustrated that SSMT results is much less sensitive to the crustal structure than to the source characteristics itself, so the variation of the assumed crustal structure does not affect the focal mechanism results much. But there is some trade-off between focal depth of the event and the crustal thickness of the regional structure [Wallace, 1986. Gao and Wallace. 1993], so the error versus depth curve only indicate

Event 88/11/15



Station: WMQ



— obs
— syn

clvd 0.0%

source time function 0.5 0.5 0.5



$M_0 = 2.26$
 $\times 10^{17}$ Nm



$M_0 = 1.30$
 $\times 10^{17}$ Nm

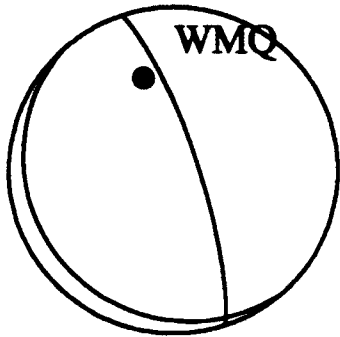


$M_0 = 2.55$
 $\times 10^{17}$ Nm

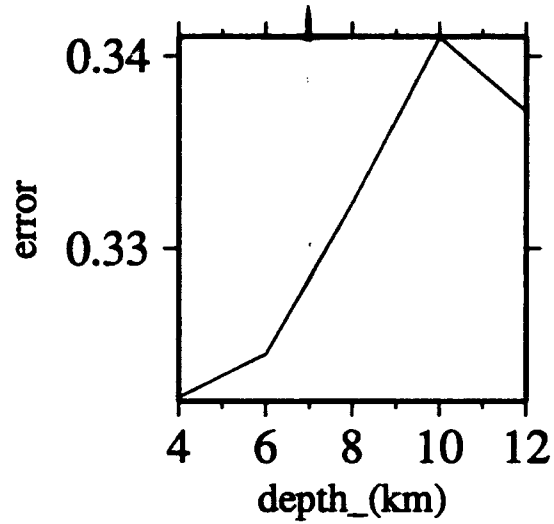
time 10.0 sec

Figure 24a

Event 90/1/21



Station: WMQ

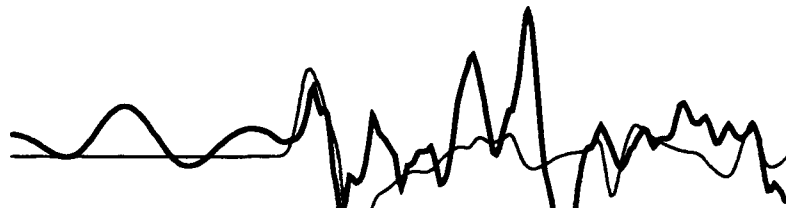


— obs
— syn

clvd 21.0%

source time function 0.2 0.5 0.2

Ver



$M_0 = 3.11$
 $\times 10^{17}$ Nm

Rad



$M_0 = 1.16$
 $\times 10^{17}$ Nm

Tan



$M_0 = 1.26$
 $\times 10^{17}$ Nm

time 10.0 sec

Figure 24b

Table 12. source parameters

Event (No.)	focal mechanisms (°)			source time functions (s)			depth (km)	Average Mo (Nm)
	θ	δ	λ	δt_1	δt_2	δt_3		
Event 1								
Event 2	318	86	-2	0.5	0.5	0.5	12	$2 \cdot 10^{17}$
Event 3	340	78	95	0.2	0.5	0.2	4	$1.5 \cdot 10^{17}$
Event 4	266	35	44	0.5	0.5	0.5	16	$1 \cdot 10^{17}$
Event 5	300	85	10	0.4	0.5	0.4	6	$1.5 \cdot 10^{17}$
Event 6	280	40	50	0.1	0.2	0.1	10	$1.5 \cdot 10^{17}$
Event 7	303	74	43	0.5	0.5	0.5	10	$2 \cdot 10^{17}$
Event 8*	274	70	90	1	3	1	16	$9.8 \cdot 10^{17}$

* -- From Xu, et al, 1989.

whether the event is relatively shallow or deep. The structure with 50 km thick crust is used throughout our study and the depths in Table 12 are the best depths with this structure. The numbers on the right of each component fit (Figure 24a and Figure 24b) are the moments calculated by

$$M_o = 4\pi\rho \times 10^{13} \times \frac{(\text{Amplitude of the observation in cm})}{(\text{Amplitude of the synthetics in cm})} \text{ (Nm)} \quad (1)$$

The average moment for each event is also shown in Table 12. Figure 24 shows two examples of the SSMT solution. The event on Nov.15, 1988 shows a strike-slip focal mechanism, while the earthquake on Jan. 21, 1990 is a thrust event. The thrust event in 1990 is within the Test Site (Figure 20).

Figure 25 summarizes the focal mechanisms of the events we have studied, there are both strike-slip and thrust events happen in this area. The P axis from the focal mechanisms trend N-S, NE-SW and NW-SE direction, which is consistent with the regional stress regime [Lithospheric Dynamics Atlas of China]. Two events (Event 1 and Event 8, see Table 11) from other studies are also plotted. Both of them are thrust events. The event in 1987 is from Pnl regional waveform modeling [Xu, et al. 1989], and the earthquake in 1976 is obtained from modeling the upper mantle records in QUE and a teleseismic record. The source parameters of all the earthquakes are listed in Table 12.

Tectonic release at Lop Nor

There has been total 15 underground nuclear explosions in Lop Nor area. Most of them are well documented in ISC bulletin. Usually, the CDSN stations do not record the nuclear explosion records, but there was an exception on Sept. 29, 1988. This was recorded on the CDSN station WMQ (see figure 26), but it was not reported as an explosion in ISC bulletin. Although this event is very small ($M=4.2$), it also has a significant Love wave, but it is not as large relatively as those records for the explosion on May 21, 1992 (Figure

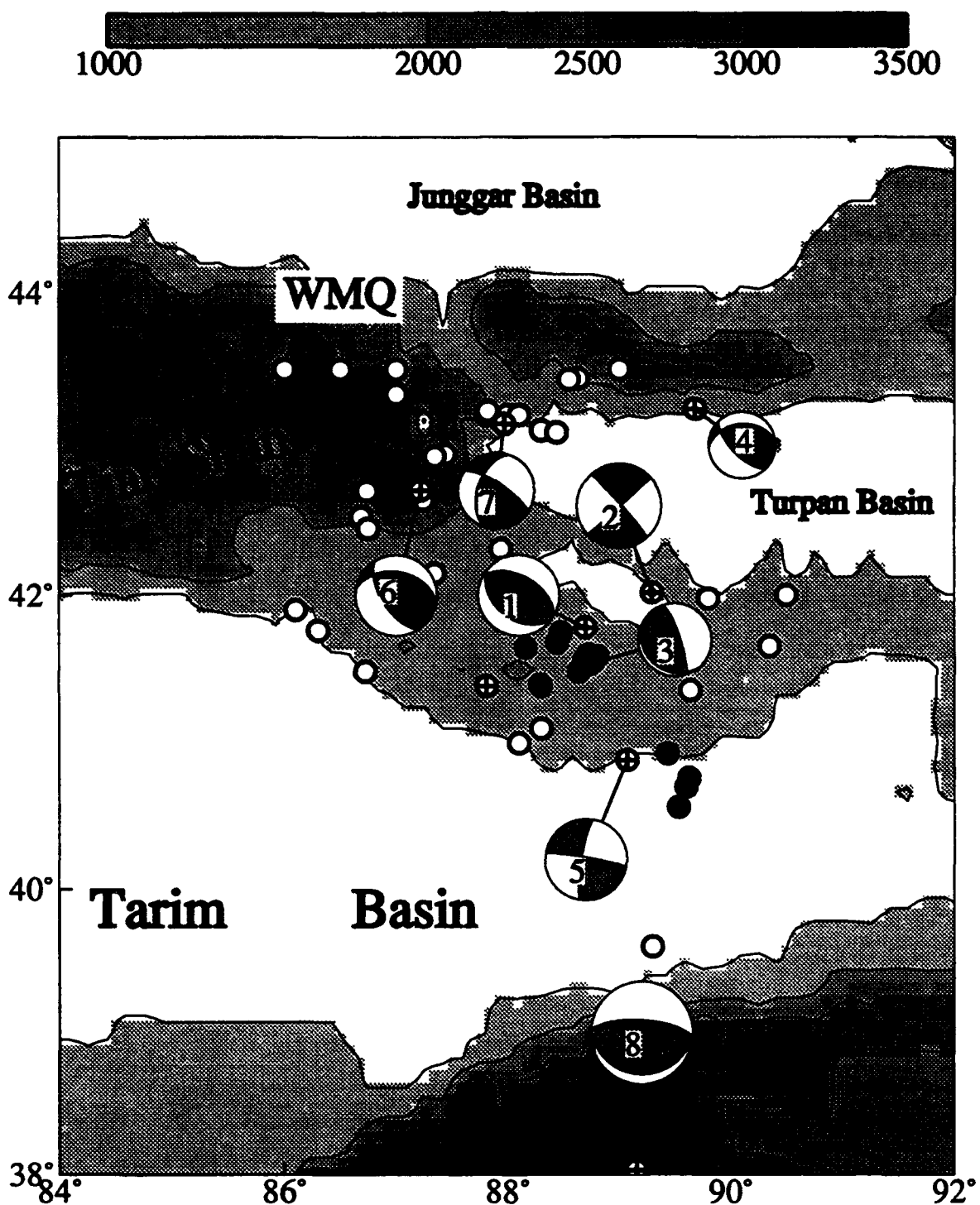


Figure 25. Focal mechanisms of the events studied here. Both strike-slip and thrust events happen in this area. The P axis from these events are in N-S or NE-SW direction which is very consistent with the regional stress regime. The numbers in the focal mechanisms are the events number (See Table 1).

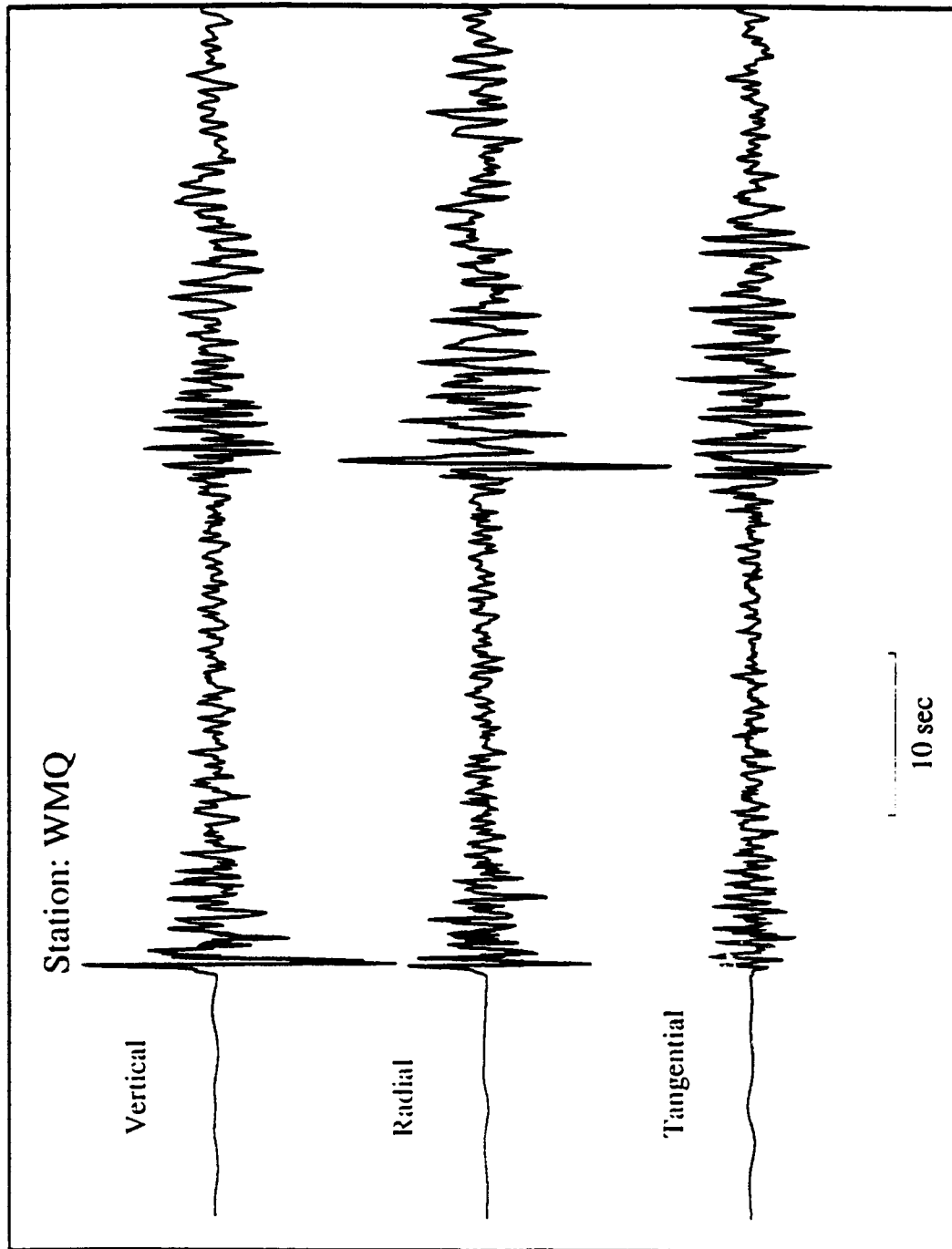


Figure 26

21). This might indicate that the tectonic release generated by this event is very small [Wallace, 1992]. This small tectonic release event can be used to study the larger explosions.

To understand the tectonic release by underground nuclear explosions, we modeled the body waves from the largest explosion (May 21, 1992). The modeling results are shown in Figure 27. We used the Helmberger-Harkrider source time function with $R=10$, $B=100$. The seismic record generated by this explosion seems to be complex. Figure 27 shows a typical record at OBN ($Dis = 36.4^\circ$, $Az = 310^\circ$). There are 3 major phases showing in the first 5 seconds, the P, pP and an unknown phase. The reflected phase pP timing seems to be delayed longer than for most of the explosions at NTS (usually 0.4 sec - 1.2 sec) [Lay, 1992]. It all appears at about 1.35 seconds. If we assume the average crustal P velocity is 6.1 km/s, the apparent depth of the explosion would be at least 4 km. The unknown phase after pP is very interesting. It could be sP generated by a earthquake source [Wallace et al., 1983]; or sP-like phase generated by slap down from spall [Douglas et al. 1986]; or a summation of several phases excited by an earthquake source. If we take a look of the available teleseismic P wave (Figure 28), we see that most of the records do have this unknown phase, but the amplitude of this phase varies from station to station. Some of them are large, but some are small. If this phase is generated by spall slap down, it would not be expected that there would be much amplitude variation. Tectonic release, and associated phenomena such as sP is most likely involved in the event. The CMT solution of the Love waves of this event shows a strike-slip focal mechanism [Ekstrom, personal communication]. This strike-slip earthquake with a delay time 0.3 seconds after the main explosion is added to the teleseismic P wave synthetics, and the records are fit reasonably well (Figure 27 . Figure 28).

Table 13. Focal mechanism of the tectonic release

$\theta(^{\circ})$	$\delta(^{\circ})$	$\lambda(^{\circ})$	$\delta t_1(s)$	$\delta t_2(s)$	$\delta t_3(s)$	depth(km)	time delay (s)	M_0 (Nm)
320	80	0	0.01	0.05	0.01	4	0.3	

Station: OBN

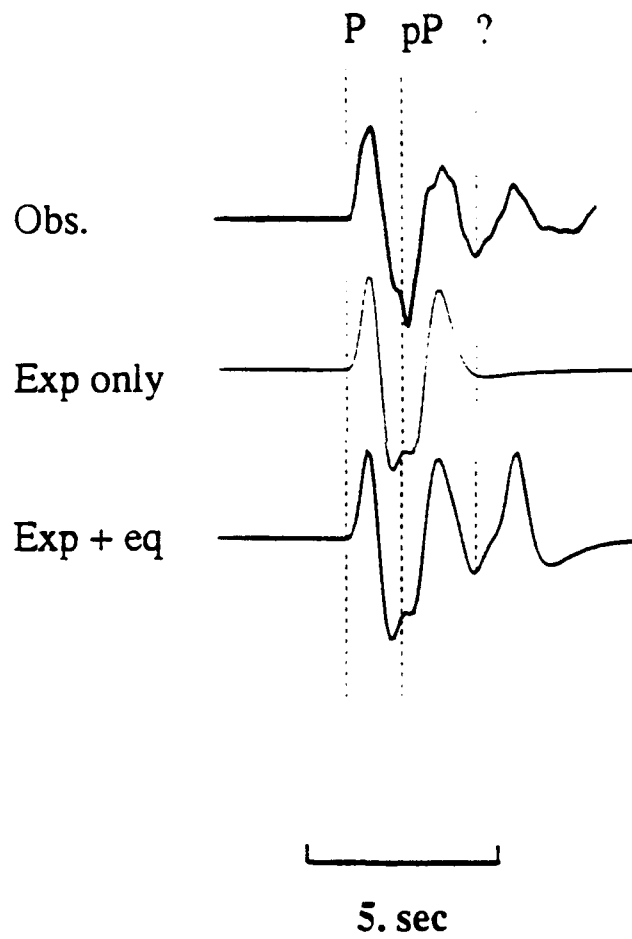
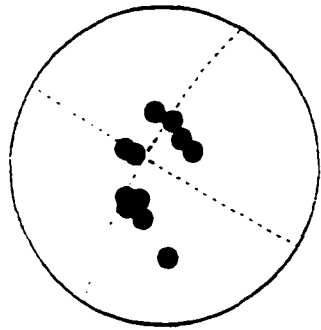


Figure 27

P WAVES



— Obs.
 - - - Exp only
 - - - Exp + eq

5. sec

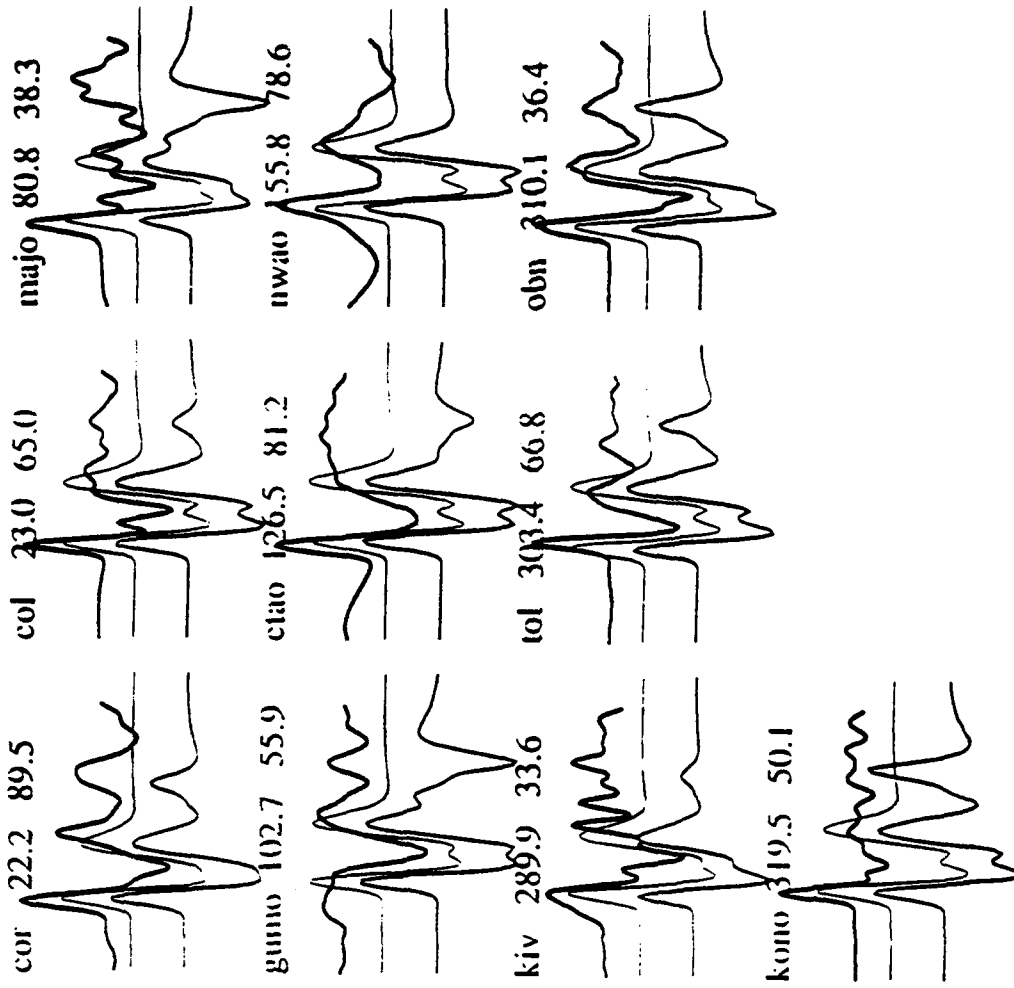


Figure 28

Almost all the nuclear explosions generate some sort of non-isotropic component which could be interpreted as tectonic release [Wallace, 1992; Patton, 1992]. This non-isotropic component is shown in the tangential component of the seismic records (SH or Love waves) [Wallace, 1992; Patton, 1992]. The amplitude of the Love waves indicates the size of the tectonic release [Wallace, 1992]; the higher the amplitude, the larger the tectonic release. Since the small explosion on Sept. 29, 1988 is a low release event (Figure 26) it could be used to simulate higher release explosions. Unfortunately, as we know, the CDSN usually do not report any records of the Chinese explosions, we do not have other explosions records at WMQ. Based on the unique records for the explosion on Sept. 29, 1988 and the WMQ earthquake records of the events around Lop Nor area, we can simulate what would look like once the tectonic release increases. The whole process is simply add an earthquake record to the explosion record which is shown in Figure 29. First we normalize both of the records for explosions and earthquakes to the same scale, then line them up at the first arrival of the P wave since the events we chose are very very close to the explosions, and simply add them together. The first trace on Figure 29 is the low tectonic release explosion records at tangential component. The second trace is the summation of the explosion and the earthquake with a proportion of 1:1. Then the third is with a proportion of 1:2 (with the double size of earthquake). Then the fourth is 1:3 and so on. When larger portion of earthquake records is added, the ratio of surface wave amplitude to the body wave amplitude becomes larger and larger indicating higher and higher tectonic release. Figure 29 shows an explosion with a strike-slip release (earthquake record of the event on Nov.15, 1988 shown in Figure 24a) and Figure 29 shows an explosion with a thrust event (Jan. 21, 1990 shown in Figure 24b). Clearly, different mechanism of the tectonic release generates different seismic records.

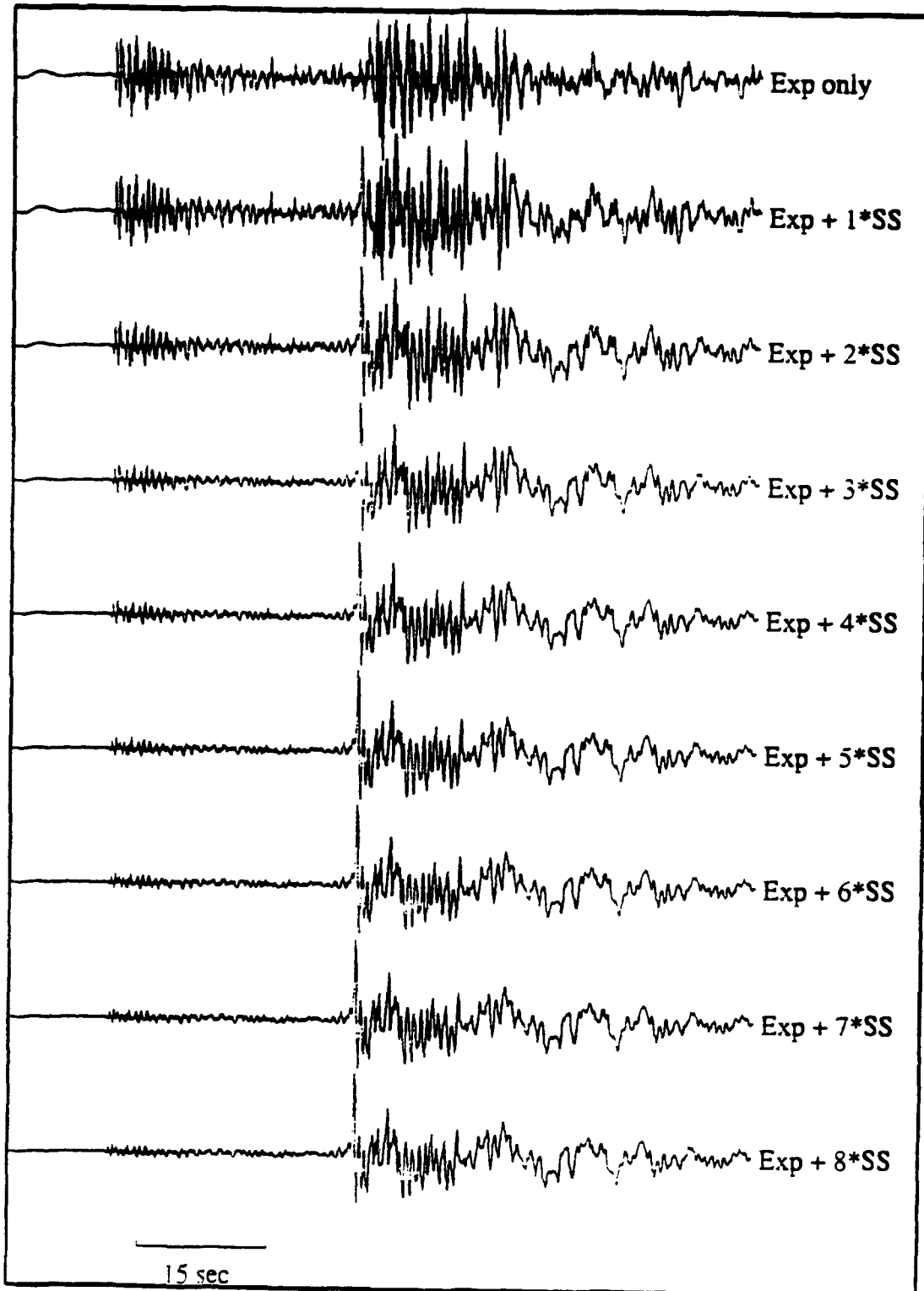


Figure 29a

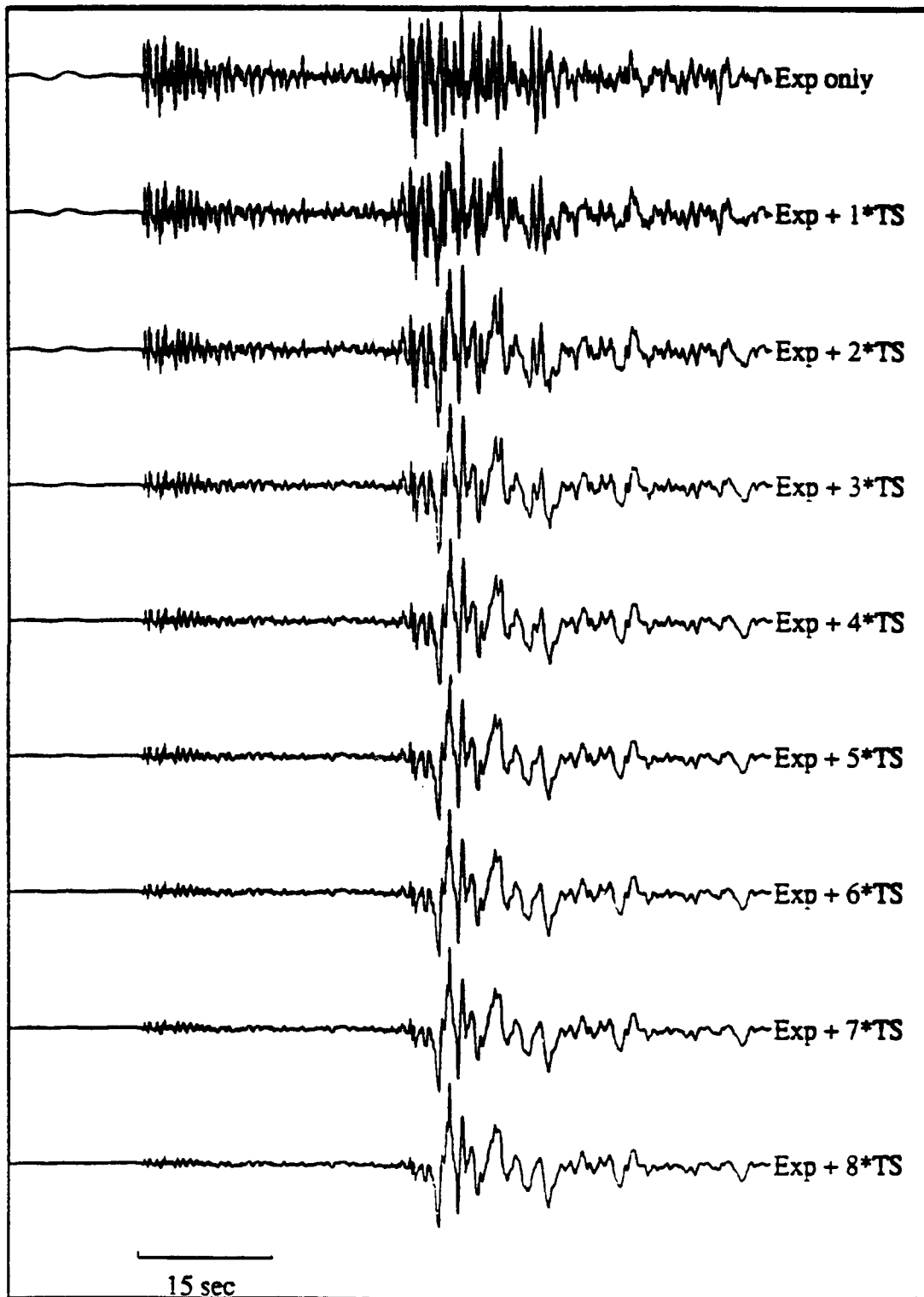


Figure 29b

The size of tectonic release is also described by the magnitude of the Love waves associated with the explosions. Smaller tectonic release has smaller M_s as determined from the Love waves. By analyzing the explosions at NTS, Patton [1992] illustrated that the M_s from an explosion and the size of the explosion (yield) has a simple power relationship. If we plot it in to a single log chart, the relationship is straight line (Figure 30). Depending on the size of the explosions, the slop of this straight line is different. When the yield is less than 100 kt, the slop is 0.84; once the yield is larger than 100 kt the slop is 1.33 (Figure 30). The tectonic release associated with the NTS tests is also falling into two categories based on the size of the explosions. For small tests (yield $W < 300$ kt), most of the tectonic release is represented as dip-slip reverse faulting, while when $W > 300$ kt, the tectonic release is dominated by vertical strike-slip faulting [Patton, 1992] (Figure 30). From all the digital records available from IRIS, the M_s of the Love waves of the explosion on May 21, 1992 at Lop Nor Test Site is 5.1. With a yield of 660 kt [Wallace, 1992b], this event is also plotted on Figure 30 . We also calculated the M_s for the Lop Nor explosions on Aug. 16, 1990 and Sept. 25, 1992. They are also shown on Figure 30 . It is remarkable that the points for the explosions at Lop Nor fall right on the statistic lines for the tests at NTS. And the body wave study of the explosion on May 21, 1992 indeed has a strike-slip tectonic release.

Discussion

The geography and geology in Lop Nor is no doubt very different from those in NTS, but the physical phenomena from the underground nuclear explosions are very similar. There is always some type of tectonic release associated with the explosions at both NTS and Lop Nor. It seems to be in common that the release associated with smaller explosions are dominated by thrust faulting while larger explosions generated vertical strike-slip mechanism tectonic release. For the small explosion on Sept. 29, 1988, which is a low

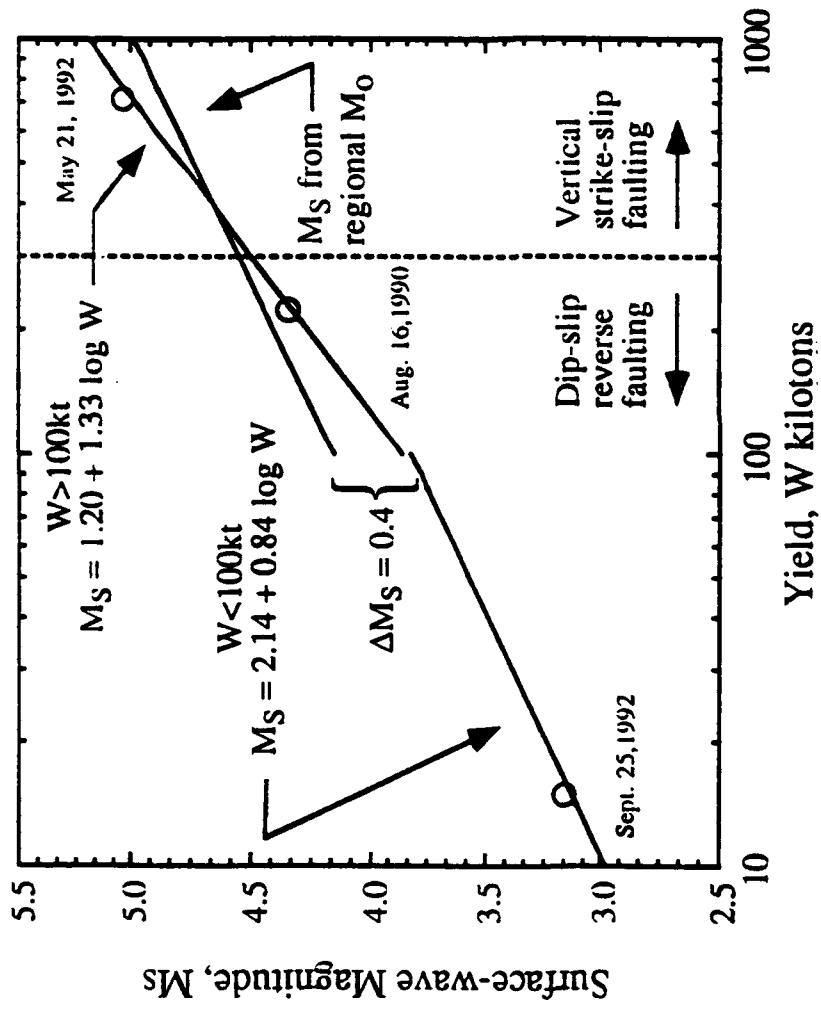


Figure 30

tectonic release event, one would expect the tectonic release would show a thrust focal mechanism. But unfortunately, for a small event (with yield 10-20 kt) like this, there are not enough small yield events to reliably determine if tectonic release scales differently above and below some yield cut-off. Also the waveform of this event (Figure 26) seems to be complicated and the tectonic release is too small to be well determined. For large explosions it appears that tectonic release is associated with a volume of material, and that volume is related to the size of the explosion [Wallace, 1992]. The rock type appears to be a very important parameter in controlling the size of tectonic release also [Toksoz and Kehrler, 1972; Wallace, 1992]. The harder the rock, the higher the tectonic release. The hard rocks at Lop Nor Test Site consists of Devonian (360-390 ma) metamorphosed conglomerate and sandstone and Carboniferous (290-360 ma) granite [Matzko, 1992], and these rocks are most capable to generate high tectonic release. In his review paper, Wallace [1992] summarized that the earthquake-like tectonic release are likely the result of three phenomena: 1) driven block or joint motion, 2) the release of the accumulated strains stored in volume surrounding the explosion, and 3) triggering slip on prestressed faults. The driven block motion is observed in all the explosions and is dominated by thrust type mechanisms, while the other two factors are dictated by the regional stress pattern. For smaller explosions, the driven block motion dominates because the energy is not high enough to either trigger any motions on faults or cause the release of accumulated strain. For larger explosions the volumetric stress-release can dominate, thus producing a seismic wavetrain which looks like a sum of an explosion and an earthquake. The mechanism of the earthquake is dependent on the regional level and orientation of stress. The earthquake studies of Lop Nor area show that both thrust and strike-slip earthquakes are happening and the tectonic release of the largest explosion so far on May 21, 1992 has a similar type mechanism as the earthquake occurred near by.

Conclusions

The non-isotropic component of the seismic records of the underground nuclear explosions at Lop Nor Test Site can be interpreted as tectonic release. This tectonic release is very consistent with the regional stress regime and earthquake mechanisms in this area. Despite of all the differences in geography and geology, the explosions in both Lop Nor and NTS do show something in common: larger explosions generate more tectonic release and this tectonic release is dominated by vertical strike-slip faulting, while small explosions generate less tectonic release which is dominated by thrust faulting. The orientation and the movement of the faultings are associated with the regional stress regime and fault distribution at the test site area.

Acknowledgment

Grant from Philip Labs F 19628-90-K-0038 at Department of Geosciences, University of Arizona.

Contribution number 8 to SASO, department of Geosciences, University of Arizona.

References

- Burger, R., T. Lay, T. Wallace, and L. Burdick, Evidence of tectonic release in long-period S waves from underground nuclear explosions at the Novaya Zemlya Test Sites, *Bull. Seism. Soc. Am.*, 76, 733–755, 1986.
- Carroll, A. R., Y. Liang, S. A. Graham, X. Xiao, M. S. Hedrix, J. Chu, and C. L. McKnight, Junggar basin, northwest China: Trapped late Paleozoic ocean, *Tectonophysics*, 181, 1–14, 1990.
- Ekstrom, G., A. M. Dziewonski, and M. M. Steim, Single station CMT: Application to the Michoacan, Mexico, earthquake of September 19, 1985, *Geophys. Res. Lett.*, 13, 173–176, 1986.
- Fan, G., and T. C. Wallace, The determination of source parameters for small earthquakes from a single, very broadband seismic station, *Geophys. Res. Lett.*, 18, 1385–1388, 1991.
- Feng, X., Seismogeological characteristics of the Xinjiang area, *Seismology and Geology*, 7 (2), 35–44, 1985.
- Gao, L., T. C. Wallace, Aftershocks of the June 1990 Rudbar–Tarom earthquake: Evidence for slip partitioning, submitted to *J. Geophys. Res.*, 1993.
- Harrison, T. M., P. Copeland, W. S. F. Kidd, and A. Yin, Raising Tibet, *Science*, 255, 1663–1670, 1992.
- Helmberger, D. V., and G. R. Engen, Modeling the long-period body waves from shallow earthquakes at regional ranges, *Bull. Seism. Soc. Am.*, 70, 1699–1714, 1980.
- Jimenez, E., M. Cara, and D. Rouland, Focal mechanisms of moderate-size earthquakes from the analysis of single-station three-component surface-wave records, *Bull. Seism. Soc. Am.*, 79, 955–962, 1989.
- Langston, C. A. single-station fault plane solutions, *Bull. Seism. Soc. Am.*, 72, 729–744, 1982.

- Lay, T., The teleseismic manifestation of pP: Problem and paradoxes, in Taylor, S. R., H. J. Patton, and P. G. Richards, eds., *Explosion Source Phenomenology, AGU Geophysical Monograph 65*, 190–126, 1992.
- Lee, K. Y., Geology of the Tarim Basin with special emphasis on petroleum deposits, Xinjiang Uygur Zizhiqu, northwest China, *U.S. Geol. Surv. Open-File Rep. 85-0616*, 55 pp., 1985.
- Li, Y., An apparent polar wander path from the Tarim block, China, *Tectonophysics*, 181, 31–41, 1990.
- Lyon-Caen, H., and P. Molnar, Gravity anomalies and the structure of western Tibet and the southern Tarim basin, *Geophys. Res. Lett.*, 11, 1251–1254, 1984.
- Mangino, S., and J. Ebel, The receiver structure beneath the Chinese Digital Seismography Network (CDSH) station: Preliminary results, Air Force report, 1992.
- Matzko, R., Geology of the Chinese nuclear test site near Lop Nor, Xinjiang Province, China, in J. Lewkowic and J. McPhetres, eds., *14th Annual PL/DARPA Seismic Research Symposium*, 297–303, 1992.
- Patton, H. J., Seismic moment estimation and the scaling of the long-period explosion source spectrum, in Taylor, S. R., J. H. Patton, and P. G. Richards, eds., *Explosion Source Phenomenology, AGU Geophysical Monograph 65*, 171–184, 1992.
- Wallace, T. C., D. Helmberger, and G. Engen, Evidence of tectonic release from underground nuclear explosions in long-period P waves, *Bull. Seism. Soc. Am.*, 73, 593–613, 1983.
- Wallace, T. C., D. Helmberger, and G. Engen, Evidence of tectonic release from underground nuclear explosions in long-period S waves, *Bull. Seism. Soc. Am.*, 85, 157–174, 1985.
- Wallace, T. C., Some useful approximations to generalize ray theory for regional distance seismograms, *Geophys. J. R. Astron. Soc.*, 85, 349–363, 1986.
- Wallace, T.C., Body wave observations of tectonic release, in Taylor, S. R., H. J. Patton, and P. G. Richards, eds, *Explosion Source Phenomenology, AGU Geophysical Monograph 65*, 161–170, 1992.

Walter, W. R., and H. J. Patton, Tectonic release from the Soviet Joint Verification Experiment, *Geophys. Res. Lett.*, 17, 1517–1520, 1990.

Xu, D., L. Gao, and K. Wang, Pnl waves study of several moderate strong earthquakes in northwestern China, *Earthquake Res. in China*, 5(4), 53–58, 1989.

Figure Captions

- Figure 1a: Two fundamental Green's functions for the tangential component, assuming a trapezoid source (0.2, 0.4, 0.2 sec) and a receiver at $\Delta = 60$ km from the source. Note that the character of the Green's function changes with depth.
- Figure 1b: Three fundamental Green's functions for the radial component. The source is the same as that in Figure 1a.
- Figure 1c: Three fundamental Green's functions for the vertical component. The source is the same as that in Figure 1a.
- Figure 2: A map showing the RMS error versus depth calculated from the "observed seismograms" and the synthetics predicted from the moment tensor inversion results for strike-slip, normal, and reverse faults. The minima of the RMS errors occur at 10 km, the assumed source depth.
- Figure 3: A similar map showing the SSM error versus depth obtained from the moment tensor inversion for strike-slip, normal, and reverse faults. The minima of the SSM errors also occur at a depth of 10 km, the assumed focal depth.
- Figure 4: A schematic map showing the multi-layered crustal models used in our numerical experiments and earthquake analysis.
- Figure 5a: A comparison between the original focal mechanism of dip-slip faulting and the fault plane solutions obtained from a single seismic station with $\Delta = 60^\circ$, given the various crustal models. All fault plane solutions are lower-hemisphere projections. The solid circles and open circles represent the compressional axis and the tensional axis, respectively.
- Figure 5b: A similar comparison between the original focal mechanism of strike-slip faulting and the fault plane solutions obtained from the single seismic station. All illustrations are the same as those in Figure 5a.
- Figure 6: A simplified map showing the epicentral region and two focal mechanisms. ANMO, near Albuquerque, New Mexico, is at an azimuth of 30° from the epicenters. A small map at the right bottom corner shows the location of the map area.
- Figure 7: A comparison between the synthetics and the observed seismograms for events on November 29, 1989, and January 29, 1990. The synthetics are dashed lines, and the observed waveforms are solid lines. The maximum amplitude ratios of the observed data to the synthetics are also shown. The RMS errors were calculated for the inversion windows shown by arrows for each component.

- Figure 8: Possible fault plane solutions for the November 29, 1989, event. The numbers at the top right corner of each solution are corresponding focal depths.
- Figure 9: A stick graph showing the composition of the eigenvectors in model space V_P from three different inversions.
- Figure 10: Location of mining explosion sources in the southwestern U.S. Table 10 gives the coordinates.
- Figure 11: The distance distribution of the data base for the southwestern U.S.
- Figure 12: A comparison between a small earthquake (left) and an explosion (right) recorded at TUC. The traces are raw broadband ground velocity.
- Figure 13: Significance as a function of distance for the southwestern U.S. Significance of 1 means a ripple-fire explosion with 99% confidence. Significance of 0.5 means ripple-fire explosion with 66% confidence.
- Figure 14: The distance distribution of the data base for the central U.S.
- Figure 15: The distance distribution of the data base for the European events recorded at GRFO.
- Figure 16: Stations (diamonds), earthquakes (squares), and raypaths used to regionalize the gross crustal structure in the region around the western Himalayan syntaxis.
- Figure 17: Crustal thickness estimates for the six blocks of the regionalization. Standard deviation is a formal estimate obtained from the model variance-covariance matrix.
- Figure 18: P_n velocity estimates for the six blocks of regionalization. As before, standard deviation is from the variance-covariance matrix.
- Figure 19: Efficiency of L_g propagation. Density of dotting indicates the efficiency of L_g propagation (the darkest regions represent the most efficient paths).
- Figure 20: Topographic map of the area around the Lop Nor Test Site. The contour interval is 1000 m. The inset shows the geographic location of the map. The black dots are the nuclear explosions which began in 1964. The black dots in the south are the atmospheric explosions, while those in the north are underground nuclear explosions. The open circles are the epicenters of the earthquakes, with a total number of 25 since 1950 within 200 km around the Lop Nor. The open circles with a cross are the events we studied in this paper. The open triangle is the CDSN station WMQ.

- Figure 21a: A record of the explosion ($M_b = 6.6$) on May 21, 1992, at GAR (dis = 14, az = 265). It has a significant Love wave component. The three components of the record are normalized to the same scale.
- Figure 21b: The latest and the largest explosion in Lop Nor ($M = 6.6$) was very well recorded world wide. At all azimuths, there is a large Love wave (tangential component). The records shown are filtered to 20 seconds.
- Figure 22: The fault distribution of the Xinjiang Province. Most of the faults are concentrated in the mountain regions and the boundaries of the basins, where most of the deformation occurs. In the Tian Shan area, most of the faults are reverse/thrust faults, and some of them are right-lateral strike-slip faults. There is a major thrust fault going through the Lop Nor area.
- Figure 23: Typical records of an earthquake near Lop Nor recorded at WMQ. The records show a very high signal-to-noise ratio and a very high quality of the body waveforms and surface waves.
- Figure 24a: SSMT solution of the event on November 15, 1988. This event shows a strike-slip mechanism with a minimum error at a depth of 12 km.
- Figure 24b: SSMT solution of the event on January 21, 1990. This event shows a thrust mechanism with a very shallow depth.
- Figure 25: Focal mechanisms of the events studied here. Both strike-slip and thrust events happen in this area. The P axes from these events are in N-S or NE-SW directions, which is very consistent with the regional stress regime. The numbers in the focal mechanisms are the event numbers (see Table 11).
- Figure 26: A record of a small explosion ($M = 4.2$) on September 29, 1988, at WMG. The figure also shows a tangential surface wave component, but the component is not as large as that associated with the explosion on May 21, 1992.
- Figure 27: Three major phases observed in the data for the first 5 seconds— P , pP , and an unknown. The third phase can be modeled as an earthquake phase shown at the bottom trace.
- Figure 28: The results of the body wave modelling for the explosion on May 21, 1992. The explosion source only (the middle trace) cannot match the wavetrains observed, especially the second trough in the observation. Once a strike-slip earthquake source is added (lower trace), the data can be matched reasonably well.

Figure 29a: Simulation of the WMQ records for tectonic release with an explosion record (September 29, 1988) added to a strike-slip earthquake (November 15, 1988), with a variation of the size of the tectonic release.

Figure 29b: Simulation of the WMQ records for tectonic release with an explosion record (September 29, 1988) added to a thrust earthquake (January 21, 1990), with a variation of the size of the tectonic release.

Figure 30: The relationship of MS versus explosion yield showing the tectonic release of an explosion at NTS (from Patton, 1992). For smaller explosions ($W < 300$ kt), the tectonic release is dominated by reverse faulting, but for larger explosions ($W > 300$ kt), strike-slip faults dominate the tectonic release. The Lop Nor events are also plotted on this chart as open circles. The Lop Nor events appear to fit the NTS relationship very well, and indeed, the explosion on May 21, 1992, did show a strike-slip tectonic release.

Prof. Thomas Ahrens
Seismological Lab, 252-21
Division of Geological & Planetary Sciences
California Institute of Technology
Pasadena, CA 91125

Prof. Keiiti Aki
Center for Earth Sciences
University of Southern California
University Park
Los Angeles, CA 90089-0741

Prof. Shelton Alexander
Geosciences Department
403 Deike Building
The Pennsylvania State University
University Park, PA 16802

Dr. Ralph Alewine, III
DARPA/NMRO
3701 North Fairfax Drive
Arlington, VA 22203-1714

Prof. Charles B. Archambeau
CIRES
University of Colorado
Boulder, CO 80309

Dr. Thomas C. Bache, Jr.
Science Applications Int'l Corp.
10260 Campus Point Drive
San Diego, CA 92121 (2 copies)

Prof. Muawia Barazangi
Institute for the Study of the Continent
Cornell University
Ithaca, NY 14853

Dr. Jeff Barker
Department of Geological Sciences
State University of New York
at Binghamton
Vestal, NY 13901

Dr. Douglas R. Baumgardt
ENSCO, Inc
5400 Port Royal Road
Springfield, VA 22151-2388

Dr. Susan Beck
Department of Geosciences
Building #77
University of Arizona
Tucson, AZ 85721

Dr. T.J. Bennett
S-CUBED
A Division of Maxwell Laboratories
11800 Sunrise Valley Drive, Suite 1212
Reston, VA 22091

Dr. Robert Blandford
AFTAC/TT, Center for Seismic Studies
1300 North 17th Street
Suite 1450
Arlington, VA 22209-2308

Dr. Stephen Bratt
Center for Seismic Studies
1300 North 17th Street
Suite 1450
Arlington, VA 22209-2308

Dr. Lawrence Burdick
IGPP, A-025
Scripps Institute of Oceanography
University of California, San Diego
La Jolla, CA 92093

Dr. Robert Burrige
Schlumberger-Doll Research Center
Old Quarry Road
Ridgefield, CT 06877

Dr. Jerry Carter
Center for Seismic Studies
1300 North 17th Street
Suite 1450
Arlington, VA 22209-2308

Dr. Eric Chael
Division 9241
Sandia Laboratory
Albuquerque, NM 87185

Dr. Martin Chapman
Department of Geological Sciences
Virginia Polytechnical Institute
21044 Derring Hall
Blacksburg, VA 24061

Prof. Vernon F. Cormier
Department of Geology & Geophysics
U-45, Room 207
University of Connecticut
Storrs, CT 06268

Prof. Steven Day
Department of Geological Sciences
San Diego State University
San Diego, CA 92182

Marvin Denny
U.S. Department of Energy
Office of Arms Control
Washington, DC 20585

Dr. Zoltan Der
ENSCO, Inc.
5400 Port Royal Road
Springfield, VA 22151-2388

Prof. Adam Dziewonski
Hoffman Laboratory, Harvard University
Dept. of Earth Atmos. & Planetary Sciences
20 Oxford Street
Cambridge, MA 02138

Prof. John Ebel
Department of Geology & Geophysics
Boston College
Chestnut Hill, MA 02167

Eric Fielding
SNEE Hall
INSTOC
Cornell University
Ithaca, NY 14853

Dr. Mark D. Fisk
Mission Research Corporation
735 State Street
P.O. Drawer 719
Santa Barbara, CA 93102

Prof Stanley Flatte
Applied Sciences Building
University of California, Santa Cruz
Santa Cruz, CA 95064

Prof. Donald Forsyth
Department of Geological Sciences
Brown University
Providence, RI 02912

Dr. Art Frankel
U.S. Geological Survey
922 National Center
Reston, VA 22092

Dr. Cliff Frolich
Institute of Geophysics
8701 North Mopac
Austin, TX 78759

Dr. Holly Given
IGPP, A-025
Scripps Institute of Oceanography
University of California, San Diego
La Jolla, CA 92093

Dr. Jeffrey W. Given
SAIC
10260 Campus Point Drive
San Diego, CA 92121

Dr. Dale Glover
Defense Intelligence Agency
ATTN: ODT-1B
Washington, DC 20301

Dr. Indra Gupta
Teledyne Geotech
314 Montgomery Street
Alexandria, VA 22314

Dan N. Hagedon
Pacific Northwest Laboratories
Battelle Boulevard
Richland, WA 99352

Dr. James Hannon
Lawrence Livermore National Laboratory
P.O. Box 808
L-205
Livermore, CA 94550

Dr. Roger Hansen
HQ AFTAC/TTR
130 South Highway A1A
Patrick AFB, FL 32925-3002

Prof. David G. Harkrider
Seismological Laboratory
Division of Geological & Planetary Sciences
California Institute of Technology
Pasadena, CA 91125

Prof. Danny Harvey
CIRES
University of Colorado
Boulder, CO 80309

Prof. Donald V. Helmberger
Seismological Laboratory
Division of Geological & Planetary Sciences
California Institute of Technology
Pasadena, CA 91125

Dr. Fred K. Lamb
University of Illinois at Urbana-Champaign
Department of Physics
1110 West Green Street
Urbana, IL 61801

Prof. Eugene Herrin
Institute for the Study of Earth and Man
Geophysical Laboratory
Southern Methodist University
Dallas, TX 75275

Prof. Charles A. Langston
Geosciences Department
403 Deike Building
The Pennsylvania State University
University Park, PA 16802

Prof. Robert B. Herrmann
Department of Earth & Atmospheric Sciences
St. Louis University
St. Louis, MO 63156

Jim Lawson, Chief Geophysicist
Oklahoma Geological Survey
Oklahoma Geophysical Observatory
P.O. Box 8
Leonard, OK 74043-0008

Prof. Lane R. Johnson
Seismographic Station
University of California
Berkeley, CA 94720

Prof. Thorne Lay
Institute of Tectonics
Earth Science Board
University of California, Santa Cruz
Santa Cruz, CA 95064

Prof. Thomas H. Jordan
Department of Earth, Atmospheric &
Planetary Sciences
Massachusetts Institute of Technology
Cambridge, MA 02139

Dr. William Leith
U.S. Geological Survey
Mail Stop 928
Reston, VA 22092

Prof. Alan Kafka
Department of Geology & Geophysics
Boston College
Chestnut Hill, MA 02167

Mr. James F. Lewkowicz
Phillips Laboratory/GPEH
29 Randolph Road
Hanscom AFB, MA 01731-3010(2 copies)

Robert C. Kemerait
ENSCO, Inc.
445 Pineda Court
Melbourne, FL 32940

Mr. Alfred Lieberman
ACDA/VI-OA State Department Building
Room 5726
320-21st Street, NW
Washington, DC 20451

Dr. Karl Koch
Institute for the Study of Earth and Man
Geophysical Laboratory
Southern Methodist University
Dallas, Tx 75275

Prof. L. Timothy Long
School of Geophysical Sciences
Georgia Institute of Technology
Atlanta, GA 30332

Dr. Max Koontz
U.S. Dept. of Energy/DP 5
Forrestal Building
1000 Independence Avenue
Washington, DC 20585

Dr. Randolph Martin, III
New England Research, Inc.
76 Olcott Drive
White River Junction, VT 05001

Dr. Richard LaCoss
MIT Lincoln Laboratory, M-200B
P.O. Box 73
Lexington, MA 02173-0073

Dr. Robert Masse
Denver Federal Building
Box 25046, Mail Stop 967
Denver, CO 80225

Dr. Gary McCartor
Department of Physics
Southern Methodist University
Dallas, TX 75275

Prof. Thomas V. McEvelly
Seismographic Station
University of California
Berkeley, CA 94720

Dr. Art McGarr
U.S. Geological Survey
Mail Stop 977
U.S. Geological Survey
Menlo Park, CA 94025

Dr. Keith L. McLaughlin
S-CUBED
A Division of Maxwell Laboratory
P.O. Box 1620
La Jolla, CA 92038-1620

Stephen Miller & Dr. Alexander Florence
SRI International
333 Ravenswood Avenue
Box AF 116
Menlo Park, CA 94025-3493

Prof. Bernard Minster
IGPP, A-025
Scripps Institute of Oceanography
University of California, San Diego
La Jolla, CA 92093

Prof. Brian J. Mitchell
Department of Earth & Atmospheric Sciences
St. Louis University
St. Louis, MO 63156

Mr. Jack Murphy
S-CUBED
A Division of Maxwell Laboratory
11800 Sunrise Valley Drive, Suite 1212
Reston, VA 22091 (2 Copies)

Dr. Keith K. Nakanishi
Lawrence Livermore National Laboratory
L-025
P.O. Box 808
Livermore, CA 94550

Dr. Carl Newton
Los Alamos National Laboratory
P.O. Box 1663
Mail Stop C335, Group ESS-3
Los Alamos, NM 87545

Dr. Bao Nguyen
HQ AFTAC/TTR
130 South Highway A1A
Patrick AFB, FL 32925-3002

Prof. John A. Orcutt
IGPP, A-025
Scripps Institute of Oceanography
University of California, San Diego
La Jolla, CA 92093

Prof. Jeffrey Park
Kline Geology Laboratory
P.O. Box 6666
New Haven, CT 06511-8130

Dr. Howard Patton
Lawrence Livermore National Laboratory
L-025
P.O. Box 808
Livermore, CA 94550

Dr. Frank Pilotte
HQ AFTAC/TT
130 South Highway A1A
Patrick AFB, FL 32925-3002

Dr. Jay J. Pulli
Radix Systems, Inc.
201 Perry Parkway
Gaithersburg, MD 20877

Dr. Robert Reinke
ATTN: FCTVTD
Field Command
Defense Nuclear Agency
Kirtland AFB, NM 87115

Prof. Paul G. Richards
Lamont-Doherty Geological Observatory
of Columbia University
Palisades, NY 10964

Mr. Wilmer Rivers
Teledyne Geotech
314 Montgomery Street
Alexandria, VA 22314

Dr. George Rothe
HQ AFTAC/TTR
130 South Highway A1A
Patrick AFB, FL 32925-3002

Dr. Alan S. Ryall, Jr.
DARPA/NMRO
3701 North Fairfax Drive
Arlington, VA 22209-1714

Dr. Richard Sailor
TASC, Inc.
55 Walkers Brook Drive
Reading, MA 01867

Prof. Charles G. Sammis
Center for Earth Sciences
University of Southern California
University Park
Los Angeles, CA 90089-0741

Prof. Christopher H. Scholz
Lamont-Doherty Geological Observatory
of Columbia University
Palisades, NY 10964

Dr. Susan Schwartz
Institute of Tectonics
1156 High Street
Santa Cruz, CA 95064

Secretary of the Air Force
(SAFRD)
Washington, DC 20330

Office of the Secretary of Defense
DDR&E
Washington, DC 20330

Thomas J. Sereno, Jr.
Science Application Int'l Corp.
10260 Campus Point Drive
San Diego, CA 92121

Dr. Michael Shore
Defense Nuclear Agency/SPSS
6801 Telegraph Road
Alexandria, VA 22310

Dr. Robert Shumway
University of California Davis
Division of Statistics
Davis, CA 95616

Dr. Matthew Sibol
Virginia Tech
Seismological Observatory
4044 Derring Hall
Blacksburg, VA 24061-0420

Prof. David G. Simpson
IRIS, Inc.
1616 North Fort Myer Drive
Suite 1050
Arlington, VA 22209

Donald L. Springer
Lawrence Livermore National Laboratory
L-025
P.O. Box 808
Livermore, CA 94550

Dr. Jeffrey Stevens
S-CUBED
A Division of Maxwell Laboratory
P.O. Box 1620
La Jolla, CA 92038-1620

Lt. Col. Jim Stobie
ATTN: AFOSR/NL
110 Duncan Avenue
Bolling AFB
Washington, DC 20332-0001

Prof. Brian Stump
Institute for the Study of Earth & Man
Geophysical Laboratory
Southern Methodist University
Dallas, TX 75275

Prof. Jeremiah Sullivan
University of Illinois at Urbana-Champaign
Department of Physics
1110 West Green Street
Urbana, IL 61801

Prof. L. Sykes
Lamont-Doherty Geological Observatory
of Columbia University
Palisades, NY 10964

Dr. David Taylor
ENSCO, Inc.
445 Pineda Court
Melbourne, FL 32940

Dr. Steven R. Taylor
Los Alamos National Laboratory
P.O. Box 1663
Mail Stop C335
Los Alamos, NM 87545

Prof. Clifford Thurber
University of Wisconsin-Madison
Department of Geology & Geophysics
1215 West Dayton Street
Madison, WI 53706

DARPA/PM
3701 North Fairfax Drive
Arlington, VA 22203-1714

Prof. M. Nafi Toksoz
Earth Resources Lab
Massachusetts Institute of Technology
42 Carleton Street
Cambridge, MA 02142

DARPA/RMO/RETRIEVAL
3701 North Fairfax Drive
Arlington, VA 22203-1714

Dr. Larry Turnbull
CIA-OSWR/NED
Washington, DC 20505

DARPA/RMO/SECURITY OFFICE
3701 North Fairfax Drive
Arlington, VA 22203-1714

Dr. Gregory van der Vink
IRIS, Inc.
1616 North Fort Myer Drive
Suite 1050
Arlington, VA 22209

HQ DNA
ATTN: Technical Library
Washington, DC 20305

Dr. Karl Veith
EG&G
5211 Auth Road
Suite 240
Suitland, MD 20746

Defense Intelligence Agency
Directorate for Scientific & Technical Intelligence
ATTN: DTIB
Washington, DC 20340-6158

Prof. Terry C. Wallace
Department of Geosciences
Building #77
University of Arizona
Tucson, AZ 85721

Defense Technical Information Center
Cameron Station
Alexandria, VA 22314 (2 Copies)

Dr. Thomas Weaver
Los Alamos National Laboratory
P.O. Box 1663
Mail Stop C335
Los Alamos, NM 87545

TACTEC
Battelle Memorial Institute
505 King Avenue
Columbus, OH 43201 (Final Report)

Dr. William Wortman
Mission Research Corporation
8560 Cinderbed Road
Suite 700
Newington, VA 22122

Phillips Laboratory
ATTN: XPG
29 Randolph Road
Hanscom AFB, MA 01731-3010

Prof. Francis T. Wu
Department of Geological Sciences
State University of New York
at Binghamton
Vestal, NY 13901

Phillips Laboratory
ATTN: GPE
29 Randolph Road
Hanscom AFB, MA 01731-3010

AFTAC/CA
(STINFO)
Patrick AFB, FL 32925-6001

Phillips Laboratory
ATTN: TSML
29 Randolph Road
Hanscom AFB, MA 01731-3010

Phillips Laboratory
ATTN: PL/SUL
3550 Aberdeen Ave SE
Kirtland, NM 87117-5776 (2 copies)

Dr. Svein Mykkeltveit
NTNT/NORSAR
P.O. Box 51
N-2007 Kjeller, NORWAY (3 Copies)

Dr. Michel Bouchon
I.R.I.G.M.-B.P. 68
38402 St. Martin D'Herès
Cedex, FRANCE

Prof. Keith Priestley
University of Cambridge
Bullard Labs, Dept. of Earth Sciences
Madingley Rise, Madingley Road
Cambridge CB3 0EZ, ENGLAND

Dr. Michel Campillo
Observatoire de Grenoble
I.R.I.G.M.-B.P. 53
38041 Grenoble, FRANCE

Dr. Jorg Schlittenhardt
Federal Institute for Geosciences & Nat'l Res.
Postfach 510153
D-3000 Hannover 51, GERMANY

Dr. Kin Yip Chun
Geophysics Division
Physics Department
University of Toronto
Ontario, CANADA

Dr. Johannes Schweitzer
Institute of Geophysics
Ruhr University/Bochum
P.O. Box 1102148
4360 Bochum 1, GERMANY

Prof. Hans-Peter Harjes
Institute for Geophysics
Ruhr University/Bochum
P.O. Box 102148
4630 Bochum 1, GERMANY

Trust & Verify
VERTIC
8 John Adam Street
London WC2N 6EZ, ENGLAND

Prof. Eystein Husebye
NTNF/NORSAR
P.O. Box 51
N-2007 Kjeller, NORWAY

David Jepsen
Acting Head, Nuclear Monitoring Section
Bureau of Mineral Resources
Geology and Geophysics
G.P.O. Box 378, Canberra, AUSTRALIA

Ms. Eva Johannisson
Senior Research Officer
FOA
S-172 90 Sundbyberg, SWEDEN

Dr. Peter Marshall
Procurement Executive
Ministry of Defense
Blacknest, Brimpton
Reading FG7-FRS, UNITED KINGDOM

Dr. Bernard Massinon, Dr. Pierre Mechler
Societe Radiomana
27 rue Claude Bernard
75005 Paris, FRANCE (2 Copies)